

**The influence of internal and external
electric fields on the transport of
energetic electrons induced by electron
irradiation in metal-insulator-metal
nanostructures**

**Bei der Fakultät für Physik der Universität Duisburg-
Essen vorgelegte Dissertation zum Erwerb des Titels
„Doktors der Naturwissenschaften“ (Dr. rer. nat.) von
Mario Marpe geb. Hufschmidt**

Datum der Disputation: 22.06.2018

Prüfungskommission:

Gutachter: Prof. Dr. A. Wucher
Prof. Dr. H. Kohl

Prüfer: Prof. Dr. H. Nienhaus

Vorsitzender der Prüfungskommission:
Prof. Dr. K. Hornberger

Contents

| | | |
|----------|--|-----------|
| 1 | Abstract: English version | 1 |
| 2 | Abstract: Deutsche Version | 2 |
| 3 | Introduction | 3 |
| 4 | Theoretical description of excitation, transport and emission of electrons in solids | 6 |
| 5 | Description of the oxide barrier inside the MIM structure | 14 |
| 5.1 | Dielectric properties of the samples | 14 |
| 5.2 | Theoretical description of the current/voltage characteristics | 16 |
| 5.2.1 | Simplified approach | 16 |
| 5.2.2 | more realistic approach | 17 |
| 5.2.3 | MIM systems | 18 |
| 5.3 | Tunneling through the oxide barrier of a MIM device | 19 |
| 6 | Experimental setup | 21 |
| 6.1 | Properties of the MIM samples | 21 |
| 6.1.1 | Fabrication and geometrical properties of MIM samples | 21 |
| 6.1.2 | Topography of the sample surface determined using an AFM | 23 |
| 6.1.3 | Topography of the sample surface determined using an optical microscope | 24 |
| 6.1.4 | Topography of the sample surface determined using a SEM | 26 |
| 6.2 | Measuring modes | 28 |
| 6.3 | Set-up for experiments without external collector/repeller electrode | 29 |
| 6.4 | Set-up for experiments with additional collector/repeller electrode | 30 |
| 6.5 | External setup | 32 |
| 6.6 | Energy levels inside the MIM and their shift due to an internal bias voltage | 35 |
| 6.7 | Properties of the electron beam | 37 |
| 6.8 | Irradiation scenarios without external collector/repeller electrode | 38 |
| 6.9 | Irradiation scenarios with external collector/repeller electrode | 40 |
| 6.10 | Interpretation of measured currents | 43 |
| 6.10.1 | Possible contributions to measured current without external collector/repeller electrode in <i>direct</i> and in <i>indirect experiments</i> | 43 |
| 6.10.2 | Current contributions with external field | 45 |

| | | |
|-----------|---|------------|
| 7 | Experimental results without external field | 49 |
| 7.1 | Scanning the electron-beam | 49 |
| 7.1.1 | x -scans Finding the active area of the sample | 51 |
| 7.1.2 | x -scans for different kinetic impact energies | 52 |
| 7.1.3 | z -scans for different kinetic impact energies | 54 |
| 7.1.4 | Evaluation of the x - and z -scans | 56 |
| 7.2 | Simulations of δ and η | 57 |
| 7.3 | Comparison with literature data | 64 |
| 7.4 | Comparison of different measuring equipment | 67 |
| 7.5 | Dependence of the direct emission yield Γ_{dir} and the indirect emission yield Γ_{indir} on the impact angle | 68 |
| 7.6 | Influence of a bias voltage on Γ_{indir} | 70 |
| 7.7 | Influence of a bias voltage on Γ_{dir} | 73 |
| 7.8 | Discussion | 74 |
| 7.9 | Conclusion | 77 |
| 8 | Experimental results obtained with external collector/repeller electrode | 78 |
| 8.1 | Position dependent current measurements | 79 |
| 8.1.1 | x -scans – Finding the active area on the sample | 80 |
| 8.1.2 | x -scans for different kinetic impact energies | 82 |
| 8.1.3 | z -scans for different kinetic impact energies | 86 |
| 8.1.4 | Evaluation of cross-absorption currents | 89 |
| 8.1.5 | Dependence of the direct emission yield Γ_{dir} and the indirect emission yield Γ_{indir} on the impact angle | 94 |
| 8.2 | Signal dependence as function of external collector/repeller voltage | 96 |
| 8.2.1 | Direct emission yield Γ_{dir} as function of the external field | 96 |
| 8.2.2 | Indirect emission yield Γ_{indir} as function of the external field | 99 |
| 8.2.3 | Evaluation of the total emission yield ζ | 102 |
| 8.2.4 | Bias voltage dependence of Γ_{indir} | 105 |
| 8.2.5 | Bias voltage dependence of Γ_{dir} | 107 |
| 8.3 | Summary | 108 |
| 9 | Conclusion | 109 |
| 9.1 | Conclusion | 109 |
| 9.2 | Outlook | 110 |
| 10 | Appendix | 111 |
| 10.1 | Acknowledgements | 111 |
| 11 | Simulations of the collector/repeller field using SIMION | 112 |
| | Bibliography | 117 |

1 Abstract: English version

The motivation for this thesis was a series of experiments applying Metal-Insulator-Metal (MIM) thin film devices under ion, photon and electron irradiation while measuring currents from the irradiated towards the non-irradiated electrode. These MIM devices consist of a several 10 nm-thick silver top electrode and an aluminum bottom electrode of similar thickness insulated by a 2..3 nm-thick aluminum oxide layer. The previous interpretation of the currents arising from the irradiation of the top metal electrode was a transport of charge carriers excited as a consequence of the irradiation, overcoming the internal oxide barrier. However, it remained an open question in how far these transport effects are exclusively "internal" processes across the barrier, which was the question to be answered within this thesis.

The advantages of MIM devices are the possible analysis of excitation below the vacuum level (in form of the *internal electron emission*) on the one hand and on the other hand the possible modification of the internal barrier height and shape by the application of a bias voltage between the MIM's top and bottom electrode.

To answer the question stated above, MIM devices were irradiated with a focused (diameter ≈ 0.75 mm) electron beam in the primary energy range from 75..1000 eV, while measuring the current either into the irradiated or into the non-irradiated electrode for various irradiation parameters (impact position, primary impact energy, impact angle) and also as function of an internal bias voltage applied between silver top and aluminum bottom electrode. The analysis of results from these experiments strongly indicate, that at least a part of the detected apparently "internal" currents measured in the non-irradiated electrode is actually caused by external processes.

Possible contributions may arise from re-absorption processes of electrons (externally) emitted into the vacuum and somehow guided back to the irradiated electrode and especially from the cross-absorption of externally emitted electrons into the non-irradiated electrode. The latter process may directly influence the "internal" current and is explained by the development of an electric field above the sample arising from the emitted electrons itself.

From these findings, a second series of experiments was triggered, where a bias-able external collector/repeller electrode above the sample was introduced, allowing to control the electric field above the sample by choosing the voltage U_d applied to the collector/repeller electrode. Therefore, it was possible to identify and quantify the cross-absorption current contributing to apparently "internal" currents and to suppress this process to obtain true internally transported electron and hole currents from the irradiated towards the non-irradiated electrode. The internal and external emission yield (i.e. the number of electrons emitted as consequence of the primary electron impact either (externally) into the vacuum or (internally) from the irradiated towards the non-irradiated electrode) was determined as function of the impact point of the electron beam on the MIM's surface, of the primary impact energy as well as of the the impact angle for static collector/repeller voltages. Additionally, experiments as function the collector/repeller voltage for different kinetic impact energies and different (internal) bias voltages have been performed.

In addition to these findings, the measurements allow to determine the total external emission yield ζ for irradiation of silver and oxide covered aluminum as function of the kinetic impact energy under electron irradiation, which is interesting due to the fact, that only few data are reported in the literature especially in the energy range below 1 keV [1].

2 Abstract: Deutsche Version

Die Motivation für die Anfertigung dieser Dissertation liegt in einer Serie von Experimenten begründet, in denen Metall-Isolator-Metall (MIM) Dünnschichtsysteme zur Messung von Strömen von der bestrahlten in die unbestrahlte Elektrode hervorgerufen durch Bestrahlung der oberen Elektrode mit Ionen, Photonen und Elektronen verwendet wurden. Diese MIM-Systeme bestehen aus einer mehrere 10 nm-dicken Silber-Deckelektrode und einer Aluminium-Bodenelektrode ähnlicher Dicke, welche mittels einer 2..3 nm dicken Aluminium-Oxidschicht voneinander isoliert sind. Die bisherige Interpretation der Ströme hervorgerufen durch die Bestrahlung der Deckelektrode war ein Transport von heißen Ladungsträgern, welche durch die Bestrahlung angeregt wurden und daher die Oxidbarriere überwinden konnten. Es blieb jedoch die Frage unbeantwortet, inwiefern diese Transportprozesse ausschließlich "interne" Prozesse durch die Barriere sind, was in dieser Dissertation beantwortet wird. Der Vorteil von MIM-Systemen liegt zum einen darin begründet, dass sich so Anregungsprozesse unterhalb der Vakuumenergie (in Form von "interner Elektronenemission") untersuchen lassen und auf der anderen Seite darin, dass die Barrierenhöhe und -form durch das Anlegen einer Biasspannung zwischen den Metallelektroden modifiziert werden kann. Um die oben aufgeworfene Frage zu beantworten, wurden MIM-Systeme mit einem fokussierten ($\varnothing \approx 0.75$ mm) Elektronenstrahl mit einer Primärenergie von 75..1000 eV bestrahlt, wobei entweder die Ströme in die bestrahlte oder in die unbestrahlte Elektrode für verschiedene Beschussparameter (Auftrreffpunkt, Primärenergie, Einfallswinkel) und auch als Funktion einer internen Biasspannung angelegt zwischen den beiden Metallelektroden des MIMs gemessen wurden. Die Analyse dieser Ergebnisse weist sehr stark darauf hin, dass zumindest ein Teil der in der unbestrahlten Elektrode gemessenen "internen" Ströme in Wirklichkeit durch externe Prozesse hervorgerufen wird. Mögliche Strombeiträge können aus Re-Absorptionsprozessen von ins Vakuum emittierten Elektronen entstehen, welche wieder auf die bestrahlte Elektrode gelangen, und insbesondere durch Kreuz-Absorptionsprozesse hervorgerufen werden, bei denen von der bestrahlten Elektrode ins Vakuum emittierte Elektronen in die nichtbestrahlte Elektrode gelangen. Der letztgenannte Prozess kann direkt den "internen" Strom beeinflussen und lässt sich mittels des Auftretens eines elektrischen Feldes durch Raumladungseffekte durch die auftreffenden und emittierten Elektronen erklären. Diese Erkenntnisse motivierten eine weitere Serie von Experimenten, bei denen eine vorspannbare Kollektor/Repeller Elektrode verwendet wurde, durch die, mittels einer angelegten Spannung U_d , das elektrische Feld oberhalb der Probe kontrolliert werden kann. Dadurch wurde es möglich, den Beitrag des Kreuz-absorptionsstrom zu den vermeintlich "internen" Strömen zu identifizieren und zu quantifizieren und schließlich auch zu unterbinden, wodurch echte interne Ströme von Elektronen und Löchen durch die Barriere bestimmt werden können. Die interne und externe Emissionsausbeute (also die Zahl der emittierten Elektronen, entweder intern durch die Barriere oder extern ins Vakuum pro einschlagendem Primärelektron) wurde als Funktion des Beschusspunktes des Primärelektronenstrahls auf der MIM-Oberfläche, als Funktion der Primärenergie und auch als Funktion des Beschusswinkels für statische Werte von U_d gemessen. Zusätzlich erfolgten Messungen als Funktion der Spannung U_d für verschiedene Primärenergien und verschiedene interne Biasspannungen.

Zusätzlich zu den Ergebnissen kann aus den Messungen auch die totale externe Elektronenausbeute ζ für den Beschuss von Silberfilmen und oxidbeckten Aluminiumfilmen mit Elektronen als Funktion der Primärenergie bestimmt werden, was insofern interessant ist, weil nur wenige Messwerte für Energien unterhalb von 1 keV in der Literatur zu finden sind [1].

3 Introduction

From a scientific view, it is interesting to study the microscopic processes inside of solid matter, that follow the impact of kinetic projectiles onto the solid and may in the end cause the emission of secondary electrons, neutrals and ions. Only the fraction of electrons with sufficient energy to overcome the surface barrier, which is for electrons limited by the work-function, may thereby be emitted into the vacuum and can therefore be studied externally.

To get a more comprehensive view, it is of interest to also study lower energetic processes as well with energies below the vacuum-energy. Therefore **metal-insulator-metal** (MIM) thin film devices with some ten nanometer thin metal films and an internally buried tunnel barrier of only a few nanometer thickness were chosen, since the energy necessary to overcome the internal tunnel barrier may be - depending on the chosen materials and film thickness - lower than the work-function delimiting the barrier for external emission. An additional advantage of MIM devices is the possibility to modify the internal barrier by the application of an internal bias voltage, which is in detail discussed in section 6.6.

The motivation for the experiments described within this thesis comes from a series of experiments in the framework of the "Sonderforschungsbereich SFB 616" (**C**ollaborative **R**esearch **C**enter CRC 616) dealing with energy dissipation processes at surfaces, in this particular case studied on **metal-insulator-metal** (MIM) thin film devices. These MIM devices consist of a silver top electrode with a thickness of 50 nm, an aluminum bottom electrode of 27 nm thickness and an insulating aluminum oxide film (thickness 3 nm). The region, where all three layers overlap, is called the "active area" of the MIM.

First experiments using MIM devices under Ar^+ -ion bombardment of the top electrode within the active area [2] proved that electronic excitation even below the vacuum level could be studied by detecting an electron current from the ion-bombarded top electrode (impact energy of several keV) into the bottom electrode of the MIM. These experiments were followed by measurements of internal currents caused by the impact of electrons [3], of photons [4, 5] and of highly charged ions [6] as well as of internal currents caused by chemical surface reactions [7].

In all cases, the currents into the bottom electrode induced by the excitation of the top electrode within the active area were interpreted in terms of an "internal" emission of electrons as consequence of energy dissipation processes. To contribute to this current, electrons have to overcome the internal barrier of the MIM formed by the thin insulating oxide layer between the metal films. According to [8], the internal barrier height for $\text{Ag}|\text{AlO}_x|\text{Al}$ MIM structures on the $\text{Al}|\text{AlO}_x$ -side is 2.1..2.4 eV and on the $\text{Ag}|\text{AlO}_x$ -side

3.4..3.9 eV. The higher barrier at the oxide–silver interface is due to hydroxide species [8], leading to a trapezoidal shape of the barrier.

Experiments performed under variation of the internal bias voltage (applied between top and bottom electrode) which changes the shape of the barrier [2, 4, 9], showed a possible polarity change of the measured internal signal. This was the basis for the interpretation of the internal currents as a sum of an ion induced electron and hole current, that are measured simultaneously. Thereby the barrier height is different for electrons and for defect electrons (holes), since the barrier height for electrons is defined in terms of the difference between the Fermi-Energy of the top silver electrode and the lower edge of the AlO_x conduction band, while the barrier height for holes is given by the energy difference between the upper edge of the AlO_x 's valence band and the top silver conduction band.

The theoretical description of such processes across the barrier in the models commonly used for a description of BEEM (**b**allistic **e**lectron **e**mission **m**icroscopy) and STM (**s**canning **T**unnelling **m**icroscopy) measurements employ only one species of charge carriers. In contrast to this, in case of MIM devices, both the electron and the hole contributions need to be considered, therefore the theoretical models had to be extended. A suitable model is discussed e.g. in [4] in terms of a two-band tunneling process.

However, in all cases, the excitation from outside must induce an excitation of charge carriers (electrons and holes) within the irradiated electrode. The excitation induced hot carriers need to be transported towards the internal barrier of the MIM and have to overcome the barrier to cause a detectable current into the non-irradiated electrode. In case of experiments under ion bombardment, this is actually a rather indirect process. Impinging ions may dissipate their kinetic energy either directly in the electronic subsystem of the bombarded electrode via "electronic friction" of the moving particle slowed down by the free electron gas of the target metal, or via collisions with the ionic subsystem ("nuclear stopping") of the target causing the lattice ions to move, which are on their part slowed down by electronic friction. This way, kinetic energy of the impinging projectile is fed into the electronic system in a collective way, which might cause the excitation of hot charge carriers. In case of electrons as excitation source, the excitation is a direct consequence of the electron irradiation, since the electrons may directly interact with the electron gas of the target electrode. Therefore, the transport process within the irradiated electrode can be probed by variation of the kinetic impact energy, which should influence the penetration depth of the projectile and should therefore also influence the transportation length towards the barrier.

Experiments with electronic excitations were previously performed in a **B**allistic **E**lectron **E**mission **M**icroscope (BEEM) setup [10] and also for irradiation experiments in a similar energy range as used here [3]. However, the irradiation experiment left the same open question regarding the possibility of *external* processes contributing to the apparent *internal* currents, which was not included in the previous experiments [11, 12, 2, 12]. A possible alternative may arise from an external electron transport. External electrons can overcome distances of several millimeters easily and thereby may constitute an alternative transport channel.

The aim of this thesis is therefore to answer this question.

The first step towards this intention were experiments with a constant primary impact energy varying the impact position of the electron beam on the MIM surface to determine the position of the active area. In contrast to the experiments before, the emission into the vacuum was probed by measuring the specimen current into the irradiated electrode, which was done in addition to the measurements of the "internal" currents into the non-irradiated electrode. This series of experiments was previously published [13] and is discussed in chapter 7 of this thesis. The evaluation of the results obtained from these measurements indicate indeed, that external processes are contributing to the "internal" currents measured in the non-irradiated electrode. This was explained by the possible development of an electric field above the surface caused by the impinging and the emitted electrons itself, changing the trajectories especially of low-energy electrons, which may therefore be re-absorbed in the irradiated electrode or cross-absorbed in the non irradiated electrode and significantly influence the measured sample currents.

These findings triggered a second series of measurements, where an external collector/repeller electrode above the surface was introduced, which can be found in chapter 8 and will be submitted for publication simultaneously with the submission of this thesis [14]. By changing the potential U_d to the external electrode in the range from ± 40 V, a controllable electric field above the sample was established. In case of $+40$ V, the field attracts all electrons and accelerates them towards the electrode, in case of -40 V, high-energy electrons are decelerated, while low-energy electrons are repelled towards the sample surface. From these findings, it was possible to determine the external processes contributing to the apparently internal currents and also to inhibit them, which allows to detect **true internal currents**. These true internal currents show a clear dependence on the impact angle, on the primary kinetic impact energy and on the internal bias voltage. In addition to these findings, the measurements allow to determine the total external emission yield ζ for irradiation of silver and oxide covered aluminum as function of the kinetic impact energy under electron irradiation, which is interesting due to the fact, that only few data are reported in the literature especially in the energy range below 1 keV [1].

4 Theoretical description of excitation, transport and emission of electrons in solids

The derivation discussed in this chapter is organized in strong accordance to the description found in Schou's review article [15]. All formulae and sketches can be found in the cited article.

If an energetic electron with the primary kinetic energy E_{prim} impinges onto a surface, it undergoes stopping processes and therefore dissipates energy in the electronic sub-system of the irradiated target material. Due to the deposition of energy, secondary electrons may leave the solid, if target electrons gather enough energy to overcome the target's work-function. If this is not the case, target electrons still may be excited to move inside the solid. Projectile electrons may leave the surface due to elastic reflection either near the surface of the sample or in deeper layers. If the reflection takes place in close vicinity to the sample surface, the primary electrons will keep most of their initial kinetic energy E_{prim} and will move with a kinetic energy $\approx E_{\text{prim}}$ in opposite direction. If the reflection takes place deeper within the solid, the projectile's energy loss will be higher on the way into the solid and also on the way back towards the surface, the backscattered electrons from these processes will have an energy significantly smaller than E_{prim} .

The excitation process causing the emission of secondary electrons can either happen, when the primary electron impinges onto the surface (then the emitted secondary electrons are called δ_0 -electrons) or when the electrons, backscattered deeper within the solid, travel back towards the surface (in the latter case they are called δ_1 -electrons). Both situations are sketched in figure 4.1.

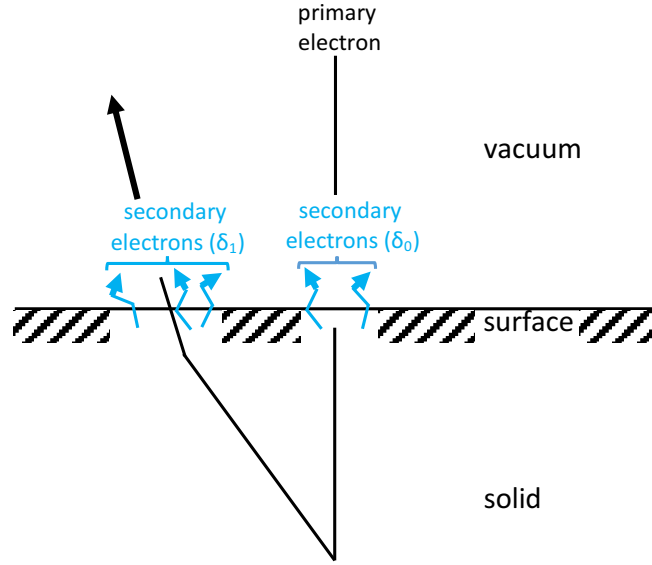


Figure 4.1: Secondary electrons excited immediately after the penetration of the sample's surface by an primary electron are called secondary electrons δ_0 ; secondary electrons excited by a primary electron reflected back towards the surface in deeper layers of the irradiated sample, are called secondary electrons δ_1 . Primary electrons dissipate kinetic energy to the sample's electronic subsystem during their way through the solid. The amount of dissipated energy is proportional to the traveled way of the primary electrons within the solid. Reproduced from [15].

According to Schou [15], a half-spherical detector mounted above the surface would detect the whole energy spectrum of secondary electrons as well as of backscattered primary electrons in the energy range from ≈ 0 eV to energies close to the primary kinetic energy E_{prim} .

The energy spectrum of the electrons detected on such a collector is usually divided (by an arbitrary convention) into *secondary electrons* with kinetic energies ≤ 50 eV and into *backscattered electrons* with kinetic energies ≥ 50 eV. This convention will be also used in this work, although Reimer in [16] states, that this convention is questionable especially in case of primary energies of 1 keV or below, which are used here. It therefore must be kept in mind that the probability to find high energetic "secondary electrons" as well as low energetic "back scattered electrons" is non-zero and that there is no systematical way to discern the electrons after their origin [15].

Typical energy spectra recorded on a detector above the sample show a maximum at ≈ 1.10 eV for the secondary electrons and at an energy of $\approx E_{\text{prim}}$ for the backscattered electrons.

According to Seiler [17], the most probable kinetic energy of the secondary electrons emitted under electron irradiation is in the range from 1.5 eV and about 75% of the emitted secondaries have a kinetic energy ≤ 15 eV.

If the detector is positively biased (typically to $\approx +50\text{V}$), it will collect all electrons above the surface and the measured current normalized to the primary electron current I_{prim} is called the *total emission yield* ζ , defined as the sum of the secondary electron yield δ and the the yield of backscattered electrons η , while η and δ are normalized to I_{prim} (see [15]):

$$\zeta = \delta + \eta. \quad (4.1)$$

In this context, the "yield" is given by the fraction of emitted particles per impinging particle. Here, the primary electron current I_{prim} is compared to detected currents to determine yields.

As discussed above, δ has contributions of secondaries excited by the passing of primaries from the vacuum towards the solid (δ_0) as well as of secondaries excited by the passing of backscattered electrons from the solid towards the surface (δ_1), therefore is, according to Schou [15]

$$\delta = \delta_0 + \delta_1. \quad (4.2)$$

According to Cazaux [18], who denoted the quantities δ_0 with SE_1 and δ_1 with SE_2 , the predominant contribution in the energy regime of up to 1 keV is $\delta_0 = \text{SE}_1$.

If the detector is negatively biased (typically to $\approx -50\text{V}$), a retarding field is established between the sample and the detector which hinders secondary electrons from reaching the detector. Therefore the current measured on the collector in this case is the current of backscattered electrons called η (again normalized to I_{prim}), which are not influenced by the electric field, since their energy is close to the initial energy E_{prim} , and therefore the influence of the collector/repeller field to them can be neglected.

The drawback of this simple collector design is caused by the fact, that the collector itself will be a source of secondary electrons (in this context called *tertiary electrons*, since they are caused by the impact of secondaries from the sample). Due to impact of high energetic backscattered electrons on the collector, tertiary electrons may be excited and also backscattered electrons may again be backscattered by the collector towards the sample. In case of a positively biased collector/repeller, the low-energy tertiary electrons are hindered from reaching the sample and are held back in the collector, which is not true in case of a negatively biased collector/repeller, acting as repeller.

This influence of the collector/repeller will be discussed in more detail in the second experimental part, where experiments with *external* collector/repeller electrode are presented.

However, by variation of the collector's potential U_d a simple way of secondary electron energy spectroscopy can be performed, since in case of a retarding field (negative potential applied to the collector/repeller), electrons with a kinetic energy below the retarding field strength are hindered from reaching the collector. In case a saturation of the collector current is found, all electrons with lower kinetic energies are either pulled towards the collector (positive potential) or hindered from reaching it (negative potential). Therefore the width and the peak position of the secondary electron energy distribution can be

deduced from the collector current I_d as function of collector voltage U_d , which will be also discussed in the frame of experiments using the external electrode.

The other approach to evaluate the emission/reflection behaviour, is the measurement of the specimen current normalized to the primary current I_{prim} . Therefore the yield of externally emitted electrons can be calculated by the equation

$$\Gamma_{\text{ext}} = 1 - \frac{I}{I_{\text{prim}}} \quad (4.3)$$

from the specimen current measured in the irradiated electrode. When externally emitted particles are repelled towards to sample by an external electric field, $\Gamma_{\text{ext}} \approx \zeta$.

According to [15], the backscattering coefficient η is well studied and depends on the impact angle, the atomic number of the target material and on the thickness of the target as well as on the primary kinetic energy. Results of computations using available simulation packages (e.g pyPENELOPE and Casino [19, 20, 21]) are in good agreement to experimental data (as shown in figure 7.6 on page 59.)

The dependence of δ on the target material is more complex and still not fully understood (see [15]). Therefore measurements for different target materials and target systems are still useful to further improve the understanding of the processes resulting in the emission of secondary electrons.

Since the surface condition also has severe influence to the sample's emission behaviour, the vacuum conditions may significantly change the magnitude of the yields, which makes it more difficult to compare measured yield values to literature data, especially since many of the few reported results in the low energy regime from the literature were taken in the 1940's to the 1960's where the vacuum conditions often were poor (see 7.3).

According to Schou [15], dissipation of the projectile's kinetic energy causes the excitation of secondary electrons. A linear slowing down is assumed and a so called *stopping power* is defined as the energy lost per primary electron per unit path length, where $\frac{dE}{dx}$ denotes the stopping power, N denotes the number density of atoms in the target material and $S(E)$ denotes the stopping cross section:

$$\left| \frac{dE}{dx} \right| = N \cdot S(E). \quad (4.4)$$

The stopping cross section $S(E)$ includes the energy dependence of the stopping power $\frac{dE}{dx}$. For energies $E \geq 10$ keV, this stopping power is quite well theoretically described and experimentally determined, but fairly unknown for the energy regime $E \leq 1$ keV as used here [15, 22]. In principle, the knowledge of the stopping power would be crucial to test the theoretical predictions. According to Schou [15], the stopping power in the low energy limit is determined by the number of free electrons within the solid, while for higher energies it is proportional to the atomic number Z .

A typical description of the secondary electron emission (also as discussed by Schou [15]) can be described by a three-step process:

- primary ionization of the target atoms by impinging projectiles during the penetration as well as secondary ionization by energetic secondary electrons
- some of the electrons liberated by the ionization process migrate to the surface
- escape of these electrons through the potential barrier at the surface

Again according to Schou [15], a theoretical description has to reproduce the following experimental findings:

1. The major part of the emitted secondary electrons originates from a thin layer near the surface, which is also called "escape zone" [23, 24, 25, 26] [found in [15]]. For metals and semiconductors, this escape zone extends over 0.5..5 nm below the surface, for insulators the escape zone may reach as much as 10..75 nm into the solid.
2. In case the irradiated sample is not single-crystalline, the angular distribution $\frac{d\delta}{d\Omega_1}$ of the emitted electrons follows a cosine function [27] (found in [15]).
3. The shape of the energy distribution $\frac{d\delta}{dE_1}$ remains unchanged, if the primary electron energy E_{prim} and/or the impact angle θ is varied, while the absolute magnitude of the values strongly depends on the primary energy E as well as on the impact angle θ [28, 29, 30, 31, 32] (found in [15]).
4. The secondary electron yield $\delta(E)$ has a maximum for primary electron energies at $\approx 1\text{keV}$ and decreases slowly for energies above the energy with maximal yield [17, 25, 33, 34, 30].
5. The yield $\delta(\theta)$ as a function of the impact angle θ increases with the angle (relative to the surface normal). It is described by the formula $\delta(\theta) = \delta(\theta^0) \cdot \cos^{-n}(\theta)$ with reported values for $n \in [1.5..0.8]$ according to [25, 33, 35].
6. Measurements on insulators show a far higher yield δ than measurements on metals (see [25, 33] (≤ 1 for metals and one order of magnitude higher for insulators)

The theoretical treatment of Schou is reproduced here, following the method proposed by [36, 37, 38] disregarding the contribution δ_1 (from backscattered electrons) to the yield δ , which is, as stated above, weak in the energy range relevant for the experiments discussed in the framework of this thesis (see [18]).

The number of **internal** secondary electrons in the energy interval $[E_0, E_0 + dE_0]$ excited by the impact of primary electrons of the energy $E(x)$ within the depth interval $[x, x + dx]$ under normal incidence is described by the equation [15]

$$\frac{1}{4\pi} \cdot f(E(x), E_0) dE_0 d\Omega_0 , \tag{4.5}$$

where $[\Omega_0, \Omega_0 + d\Omega_0]$ denotes the angle interval, in which secondary electrons move (see [15]). The formula is valid under the assumption of an isotropic excitation, which is only partially true.

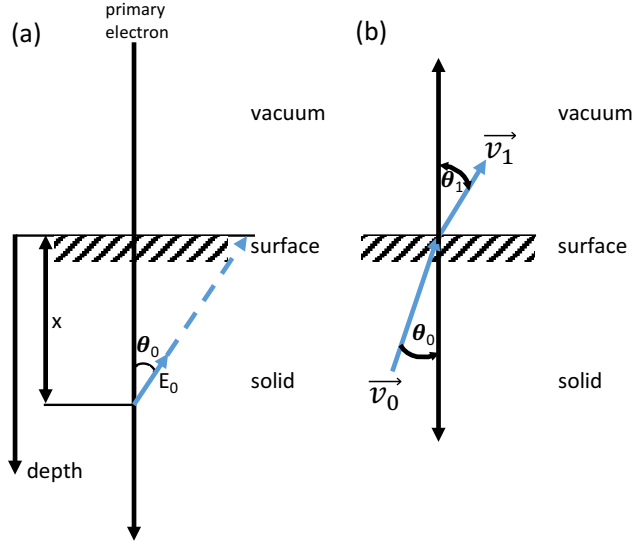


Figure 4.2: **(a)** Geometry of the escape of a liberated electron from depth x with the initial energy E_0 for normal incidence (relative to surface normal) (reproduced from [15]) **(b)** Electron passing the surface barrier: For planar barrier, the energy component parallel to surface remains unchanged (reproduced from [15]).

Since secondary electrons are produced in a thin escape zone, the energy loss of the primary electron within this escape zone can be neglected (see [15]):

$$f(E(x), E_0)dE_0d\Omega_0 \approx f(E, E_0)dE_0d\Omega_0 . \quad (4.6)$$

The liberated electrons then move towards the surface. It is assumed, that the secondaries have the probability $\exp(-\frac{x}{\lambda \cdot \cos(\theta)})$ to reach the surface in a straight line from their point of liberation towards the surface (see panel (a) of 4.2). Only electrons reaching the surface with their initial energy are ejected from the surface, even electrons colliding only once do not possess enough energy to overcome the surface barrier.

The distribution of secondaries after passing the surface barrier (the upper limit is expanded to ∞ , since most secondary electrons originate from the escape zone), is described by (see [15]):

$$J(E_0, \Omega_0) \cdot dE_0 \cdot d\Omega_0 \approx \left(\frac{1}{4\pi}\right) dE_0 d\Omega_0 \int_0^\infty f(E, E_0) \cdot \exp\left(-\frac{x}{\lambda(E_0) \cdot \cos(\theta)}\right) dx \quad (4.7)$$

Calculating the integral in 4.7 results in (see [15]):

$$J(E_0, \Omega_0) \cdot dE_0 \cdot d\Omega_0 = \left(\frac{1}{4\pi} \right) \cdot f(E, E_0) \cdot \lambda(E_0) \cdot \cos(\theta_0) \cdot dE_0 \cdot d\Omega_0 \quad (4.8)$$

Typically a planar barrier of the magnitude U_0 is assumed [39, 40, 41], which the electrons have to overcome to be emitted into the vacuum. The situation is sketched in panel (b) of figure 4.2. The emission angle θ_1 and the emission energy E_1 (both in the vacuum) are related to the Energy E_0 and angle θ_0 in the solid via the equations in 4.9 (see [15]).

$$\begin{aligned} E_1 \cdot \cos^2(\theta_1) &= E_0 \cdot \cos^2(\theta_0) - U_0 \\ E_1 \cdot \sin^2(\theta_1) &= E_0 \cdot \sin^2(\theta_0) \\ \Rightarrow E_1 + U_0 &= E_0 \end{aligned} \quad (4.9)$$

Therefore the energy component parallel to the surface remains unchanged, while the component normal to the surface is reduced (see panel (b) of 4.2, [15]).

The surface barrier for metals is determined by the work function Φ and the Fermi energy E_F with $U_0 = \Phi + E_F$, for insulators (like the aluminum oxide) the surface barrier is determined by the electron affinity.

The distribution of emitted secondary electrons is described by the equation (see [15]):

$$\frac{d\delta}{dE_1} \cdot (E, E_1) \cdot dE_1 = \frac{1}{4} \left(1 - \frac{U_0}{E_0} \right) \cdot \lambda(E_0) \cdot f(E, E_0) \cdot dE_0 \quad (4.10)$$

Integration of 4.10 with respect to E_0 leads to the secondary electron yield 4.11 (see [15]).

$$\delta = \frac{1}{4} \int_{U_0}^E \left(1 - \frac{U_0}{E_0} \right) \cdot \lambda(E_0) \cdot f(E, E_0) \cdot dE_0 \quad (4.11)$$

To evaluate the equation, the knowledge of the production rate $f(E, E_0)$ and of the escape length $\lambda(E_0)$ would be crucial. By crude assuming that the escape length λ is independent of E_0 , $\lambda(E_0) = \lambda$, the integral 4.11 leads essentially to a quantity proportional to the stopping power of the primaries shown in 4.11. C_0 is a constant; W describes the average energy to produce an ion-electron pair, which is the average energy to liberate an electron with energy higher than U_0 (from [15]):

$$\int_{U_0}^E f(E, E_0) \cdot dE_0 = \left(\frac{C_0}{W} \right) \cdot \left| \frac{E_0}{dx} \right|_e \quad (4.12)$$

The result (according to [15]) is the semi-empirical electron yield with the constant C_1

$$\delta \approx \frac{C_1}{4} \frac{\lambda}{W} \left| \frac{dE}{dx} \right|_e, \quad (4.13)$$

where C_1 includes the contribution from the term $\frac{U_0}{E_0} \cdot f(E, E_0)$ with the additional approximation, that the energy of the ejected electrons is constant.

The advantage of 4.13 is the factorization in λ , W and $(\frac{dE}{dx})_e$. λ denotes the characteristic escape length, which is independent of the primary energy and of the impact angle. The electron-ion pair energy W is almost independent of the primary energy [42]. The target material influences W and the stopping power $\frac{dE}{dx}$. Although the description by 4.13 is not complete, it can be observed, that the production rate $f(E, E_0)$ is influenced by the target material. In principle also $\lambda(E_0)$ depends on the target material, so the energy-independent λ is just a first approximation. The thin escape zone, the weak energy-dependence of $\frac{d\delta}{dE_1}$ and the increase of δ for insulators are included in the description. The contribution of reflected electrons is not included in this model. (The more detailed description including the full discussion of the model can be found in [15]).

As discussed above, a non-negligible fraction of the secondary electrons liberated through the irradiation of the solid with energetic electrons cannot overcome the surface barrier -either due the fact that their trajectories are not pointed towards the surface or to the fact that the excitation takes place outside the escape zone or to the fact that the secondaries are scattered within the solid.

Therefore a full description of the energy dissipation of the primary's kinetic energy needs to include these excitation processes not resulting in external electron emission as well.

To allow the experimental determination of these processes, multi-layer samples were applied within the experiments. These MIM devices allow for a detection of tunneling currents across a thin insulating oxide barrier between the top electrode and the bottom electrode. In the experiments discussed here, the top electrode consisted of a 50nm-thick silver film, the bottom electrode of a 30nm-thick aluminum film, while the insulating film was fabricated by a consumptive anodic oxidation to form an insulating aluminum oxide film of about 3nm-thickness reducing the thickness of the aluminum film to ≈ 27 nm.

The thin insulating film allows tunneling of excited charge carriers through the internal barrier of the MIM. In case the internal barrier is smaller than the external barrier, even particles with less energy necessary to overcome the work-function of the top electrode can leave this electrode - not to the vacuum, but to the aluminum bottom electrode.

Especially in case of excitation processes far within the solid (and therefore far outside the escape zone), excited charge carriers from these processes can be detected as *internal currents*.

5 Description of the oxide barrier inside the MIM structure

5.1 Dielectric properties of the samples

The condition of the insulating oxide barrier of the MIM sample was identified by recording **C**urrent-**V**oltage (CV) characteristics of the sample. Therefore the potential of one (usually of the upper silver) electrode is varied from -0.5 V to $+0.5$ V with a voltage feed $s := \frac{dU}{dt}$ of the order of 20..100 mV/s, while the current into the other MIM electrode (usually the aluminum bottom electrode) without electron irradiation is measured. As discussed in chapter 5.2.3, the current answer of the MIM device to the voltage ramp depends on the value of the oxide's resistance R_{AlO_x} , the voltage feed s and the dynamic capacitance C_d of the MIM as well as on the tunneling current I_{tunnel} as expressed in the equation

$$I(t) = \frac{U(t)}{R_{\text{AlO}_x}} + s \cdot C_d + I_{\text{tunnel}} . \quad (5.1)$$

A typical result of such a CV measurement is depicted in figure 5.1, showing the usual behavior of an intact MIM device with a pronounced current hysteresis ΔI . Defective MIM devices show just an ohmic characteristic. The value of ΔI is determined by the voltage feed of the voltage ramp and the dynamic capacitance of the MIM device via

$$\Delta I = C_d \cdot \frac{dU}{dt} = C_d \cdot s . \quad (5.2)$$

The constant slope of the current curve is described by the fraction $\frac{U(t)}{R_{\text{AlO}_x}}$ and is therefore a consequence of the non-infinite resistance of the oxide layer. A pronounced tunneling current I_{tunnel} would be visible in an exponential increase/decrease of the current. This is clearly not the case in figure 5.1.

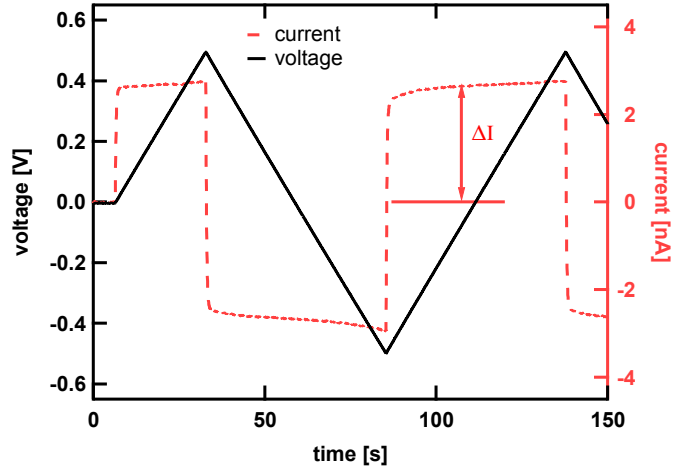


Figure 5.1: **Black curve:** voltage ramp applied between top and bottom electrode; **red curve:** current induced in the bottom electrode by the voltage ramp. The charging current ΔI gives the dynamic capacitance C_d (see equation 5.2). See also [13].

The dependence of the hysteresis ΔI on the voltage feed s is shown in figure 5.2. The dynamic capacitance of the (individual) MIM device is determined by the slope of the indicated least square fit line to $0.14 \mu\text{F}$. Combining this finding with the known thickness of the aluminum oxide (3 nm) and the known dimension of the active area of $4 \text{ mm} \cdot 4 \text{ mm}$ using the formulae valid for an ideal parallel plate capacitor allows to calculate the oxide's relative permittivity $\epsilon_{\text{rel}} \approx 6$. The relative permittivity of anodic oxides on aluminum wires was reported before [43, 44, 45] to reach values of $\epsilon_{\text{rel}} \approx 11$ [13]. Assuming an already existing gas phase oxide on the aluminum film, when the anodic oxidation is started in the droplet cell to fabricate the MIM samples, would explain the lower value for ϵ_{rel} in this case.

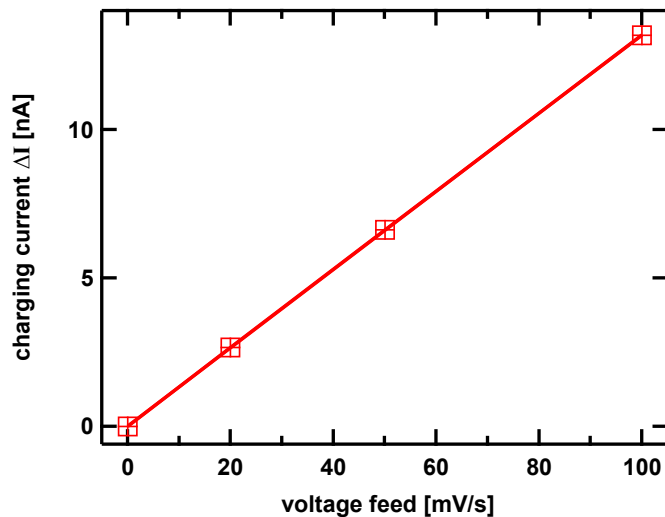


Figure 5.2: Charging current as a function of the voltage feed: ΔI is affected linearly by the voltage feed. See also [13].

Current-Voltage (CV) characteristics were recorded frequently before and after the e^- -beam experiments to ensure that the electrical properties of the device remain unchanged. During experiments under ion bombardment in the past, it was often observed, that the CV-characteristics changed during experiments as a consequence of the irradiation. In many cases the initial CV-characteristics could be reached again by the application of voltage ramps to the top electrode for several hours. Due to this finding, the suspected reason for the changes in the characteristics was the implantation of mobile defects (ions) within the oxide that lowered the resistance of the oxide significantly. By applying voltage ramps, the mobile defects were moved causing the regain of the oxide's high resistance. A similar behavior was never observed during the experiments under electron irradiation reported here. Therefore the repeated measurement of the CV-characteristics was just a precaution.

5.2 Theoretical description of the current/voltage characteristics

The current answer of the MIM to a voltage ramp as shown in figure 5.1 can be described by the models as discussed within this chapter, which can be also found in the author's diploma thesis [46], and have been included here to improve the availability of the discussion.

5.2.1 Simplified approach

The most simplified model of a MIM device would be a serial connection of a capacitor with the capacitance C and of a resistor with the resistance R shown in figure 5.3. The resistor represents the resistance of the top metal electrode. In case of thin films with a thickness of several 10 nm, the resistance depends on the film thickness [47] and may reach values of $\approx 10..40 \Omega$. The capacitor is formed by the two overlapping electrodes of the MIM insulated by the aluminum oxide film. It can well be simulated by a parallel plate capacitor with the oxide film as dielectric.



Figure 5.3: Equivalent circuit diagram of the most simplified description of a MIM

The equivalent circuit diagram is depicted in figure 5.3.

The voltage ramps to the silver top electrode can be parameterized by:

$$U(t) = \begin{cases} U_{\min} + s \cdot t & , t \in [0, T/2] \\ U_{\max} - s \cdot (t - T/2) & , t \in [T/2, T] \end{cases}$$

$$T = \frac{2 \cdot (U_{\max} - U_{\min})}{s}$$

U_{\min} is equal to the lower limit of the voltage ramp (typically $-0.5.. -1$ V), U_{\max} to the upper limit (typically $+0.5..1$ V) and s describes the rate of the ramp (e.g. $s = \frac{dU}{dt} = 20\text{mV/s}$). Then the period T of the voltage ramps can be expressed by the equation above.

$$\frac{dI}{dt} + \frac{1}{R \cdot C} \cdot I = \frac{1}{R} \cdot \frac{dU(t)}{dt} \quad (5.3)$$

For the rising edge of the voltage ramp

$$\Rightarrow I(t) = s \cdot C + \left(\frac{U_{\min}}{R} - s \cdot C \right) \cdot e^{-\frac{t}{R \cdot C}} \quad (5.4)$$

and for the falling edge

$$\Rightarrow I(t) = -s \cdot C + 2 \cdot s \cdot C \cdot e^{-\frac{t-T/2}{R \cdot C}} + \left(\frac{U_{\min}}{R} - s \cdot C \right) \cdot e^{-\frac{t}{R \cdot C}} \quad (5.5)$$

5.2.2 more realistic approach

The most simple approach discussed before is unrealistic since it assumes a perfectly insulating oxide layer. A more realistic approach applies a resistor R_{AlOx} parallel to the capacitor like sketched in figure 5.4, simulating the finite ohmic resistance of the oxide film.

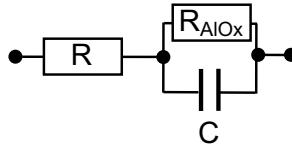


Figure 5.4: Equivalent circuit diagram of the more realistic description of a MIM

rising edge

$$I(t) = \frac{R_{\text{AlO}_x}}{R + R_{\text{AlO}_x}} \left[\frac{U_{\text{min}}}{R} - \frac{R_{\text{AlO}_x}}{R + R_{\text{AlO}_x}} sC \right] e^{-\frac{t}{\tau}} + \left[\frac{U_{\text{min}}}{R + R_{\text{AlO}_x}} + \left(\frac{R_{\text{AlO}_x}}{R + R_{\text{AlO}_x}} \right)^2 sC \right] + \frac{st}{R + R_{\text{AlO}_x}} \quad (5.6)$$

$$R_P = \left. \begin{array}{l} \text{For } R_{\text{AlO}_x} \rightarrow \infty : \\ \frac{R \cdot R_{\text{AlO}_x}}{R + R_{\text{AlO}_x}} \rightarrow R \\ \frac{R_{\text{AlO}_x}}{R + R_{\text{AlO}_x}} \rightarrow 1 \end{array} \right\} \Rightarrow I(t) = s \cdot C + \left[\frac{U_{\text{min}}}{R} - s \cdot C \right] \cdot e^{-\frac{t}{R \cdot T}} \quad (5.7)$$

$$R_P = \left. \begin{array}{l} \text{For } R_{\text{AlO}_x} \gg R : \\ \frac{R \cdot R_{\text{AlO}_x}}{R + R_{\text{AlO}_x}} \rightarrow R \\ \frac{R_{\text{AlO}_x}}{R + R_{\text{AlO}_x}} \rightarrow 1 \end{array} \right\} \Rightarrow I(t) = \left[\frac{U_{\text{min}}}{R_{\text{AlO}_x}} + sC \right] + \left[\frac{U_{\text{min}}}{R} - sC \right] e^{-\frac{t}{R \cdot T}} + \frac{st}{R_{\text{AlO}_x}} \quad (5.8)$$

$$t \gg R \cdot C \Rightarrow \boxed{I(t) = \frac{U(t)}{R_{\text{AlO}_x}} + s \cdot C} \quad (5.9)$$

5.2.3 MIM systems

In addition to the capacitance, the oxide's resistance and the resistance of the thin metal films, a tunneling resistance occurs due to the thin oxide barrier see 5.5.

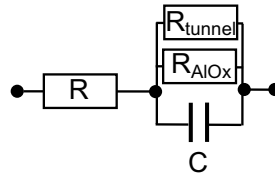


Figure 5.5: Equivalent circuit diagram of the description of a realistic MIM

Depending on the thickness of the oxide barrier and the bias voltage between the electrodes of the MIM (in case applied), tunneling currents may flow from the irradiated to the non-irradiated electrode. The tunneling current may thereby be explained by a tunneling model, which can be found in chapter 5.3 below.

Multiplying the tunnel current density as defined below with the dimension of the active area of the MIM sample would allow to calculate the tunneling current. The equation would have the following structure (for $t \gg R \cdot C$)

$$\Rightarrow I(t) = \frac{U(t)}{R_{\text{AlO}_x}} + s \cdot C + I_{\text{tunnel}} \quad (5.10)$$

5.3 Tunneling through the oxide barrier of a MIM device

The whole discussion and all formulae within this chapter were taken from [4]. As discussed in chapter 4, the excitation caused by the irradiation of the surface may lead to the excitation of charge carriers within the solid. In case the charge carriers cannot overcome the surface barrier, they stay within the solid.

The internal barrier formed by the thin insulating oxide between the top and the bottom electrode of the MIM may be crossed by tunneling. Charge carriers excited in the irradiated electrode due to electron irradiation may be detected in the non-irradiated electrode of the MIM. This can be understood by means of a two-temperature tunneling model where an **electron temperature** is assigned to excited electrons. The non irradiated electrode stays at room temperature. The existing models must be generalized since up to now they just describe the excitation inside the top silver electrode and the detection in the bottom electrode, but during the measurements discussed in the framework of this thesis also the opposing effect was detected when irradiating the bottom electrode and detecting inside the top electrode.

The electron induced electronic excitation in the irradiated electrode can be described as Fermi distribution, whereas the electron temperate is locally and temporally raised due to the irradiation with electrons. The non-irradiated electrode remains at room temperature.

According to [4, 48], the tunneling current density (net) can be written as

$$j = \frac{4 \cdot \pi \cdot m \cdot e}{h^3} \int_0^\infty [f_1(E) - f_2(E)] dE \int_0^E P_{\text{tun}}(E, E_{\parallel}) \cdot dE_{\parallel} . \quad (5.11)$$

- E is the energy of the charge carrier
- E_{\parallel} describes the energy component parallel to the plane of the insulating film
- $f_1(E)$ denotes the probability of the occupation for electron states in the irradiated electrode
- $f_2(E)$ denotes the probability of the occupation for electron states in the non-irradiated electrode

- m is the electron mass
- e is the elementary charge
- $P_{\text{tun}}(E, E_{\parallel}, U)$ is the transmission probability for the bias-voltage U between the both electrodes

According to [4], the occupation probabilities for the electron gases can be expressed by the equations:

$$f_1(E, U, T_1) = \left[\exp\left(\frac{E - e \cdot U}{k_B \cdot T_1}\right) + 1 \right]^{-1} \quad (5.12)$$

and by

$$f_2(E, U, T_2) = \left[\exp\left(\frac{E}{k_B \cdot T_2}\right) + 1 \right]^{-1}, \quad (5.13)$$

where E denotes the energy of the charge carrier (above the Fermi energy of the irradiated electrode), U the applied bias voltage between the metal films of the MIM, k_B is the Boltzmann factor, T_1 is the electron temperature of the electron gas in the irradiated electrode and T_2 is the electron temperature of the electron gas in the non-irradiated electrode. According to [4], assuming that the transmission probability $P_{\text{tun}} = 1$ for electrons (and holes) in the energy states above the barrier and the tunneling probability through the barrier in WKB approximation can be calculated to:

$$P_{\text{tun}}(E, E_{\parallel}, U) = \exp\left[-2 \int_0^{d_{\text{Ox}}} [-k_z^2(E, E_{\parallel}, z', U)]^{1/2} dz'\right] \quad (5.14)$$

for the impact angle θ on the oxide interface, the thickness of the oxide film d_{Ox} , the energy E , k_z the electron wave number normal to the interface plane, the voltage U and the position z' . This discussion is described in more detail in [4]; the WKB approximation is discussed in [49].

$$j(U, T_1, T_2) = \frac{4 \cdot \pi \cdot m \cdot e}{h^3} \int_{E_0(U)}^{\infty} [f_1(E, U, T_1) - f_2(E, T_2)] \left(\int_0^{E - E_0(U)} P_{\text{tun}}(E, E_{\parallel}, U) \cdot dE_{\parallel} \right) \cdot dE. \quad (5.15)$$

The lower integration limit of the first integral $E_0(U) = \max(-E_{F_2}, e \cdot U - E_{F_1})$ avoids contributions of energies below the valence band, where no electronic states exist in the implemented model as discussed in [4]. The upper integration limit of the second integral implements the requirement, that only electrons with an energy component perpendicular to the film plane $> E_0(U)$ are able to overcome the tunnel barrier.

6 Experimental setup

Major parts of this chapter were published before in [13] or are part of a manuscript [14] of an article which will be submitted soon to the "Journal of Electron Spectroscopy and Related Phenomena".

6.1 Properties of the MIM samples

6.1.1 Fabrication and geometrical properties of MIM samples

The MIM samples used here were fabricated in the following way:

- The bottom electrode is formed by physical vapour desorption of aluminum evoked from thermal evaporation under ultra-high vacuum conditions onto a glass substrate (dimensions 18 mm · 9 mm) which is partially masked by evaporation masks that define the area where desorption of metal vapour is possible.
- The lateral dimensions of the aluminum film formed on the substrate are (due to the evaporation mask) 18 mm · 4 mm; the film thickness monitored by a quartz microbalance is set to about 30nm.
- The sample is removed from the vacuum chamber and the surface of the aluminum film oxidized (sparing a contact area) using an electrochemical droplet cell. This way, a thin aluminum oxide film is formed by a consumptive oxidation reducing the residual thickness of the aluminum film. The thickness of the aluminum oxide film is controlled by setting the oxidation potential. A detailed description of the process can be found in [50].
- The thickness of the oxide is a crucial parameter since it must be on the one hand high enough to warrant a stable interface, but on the other hand low enough to enable tunneling of excited charge carriers through the oxide.
- After the oxidation, the sample is mounted again inside of an ultra high vacuum chamber to evaporate the silver top electrode across the aluminum oxide film.
- The evaporation masks used for this process leave an area of 8 mm · 4 mm open, where the silver film evokes by thermal vapor deposition. The thickness, again monitored by a quartz microbalance, is set to $\approx 50\text{nm}$.

- The crossing region, where the top silver electrode onto the insulating aluminum oxide onto the bottom aluminum electrode overlap, is called the **active area** of the MIM. The lateral dimension of the active area are $4\text{ mm} \cdot 4\text{ mm}$ with a total thickness of the layer stack of $\approx 80\text{nm}$ on top of the glass substrate.
- The sample can be tested by the application of a voltage ramp (usually applied to the top silver electrode) while measuring the current answer in the other (usually the bottom aluminum) electrode. A typical current/voltage characteristics is shown in figure 5.1 above.
- If the sample is found to be intact and no ohmic characteristic is found, it is mounted on a rotatable x - y - z -manipulator mounted on an ultra high vacuum chamber. The x -direction of the manipulator is chosen to be parallel to the sample's silver film, the z -direction parallel to the aluminum film and the y -direction defines the distance between electron gun and sample. The silver electrode is contacted on both sides of the active area using conductive carbon cement. Also the aluminum electrode on the non-oxidized part of the aluminum film is contacted this way. Both electrodes are individually connected via voltage feedthroughs to the atmospheric side of the surrounding ultra-high vacuum chamber.

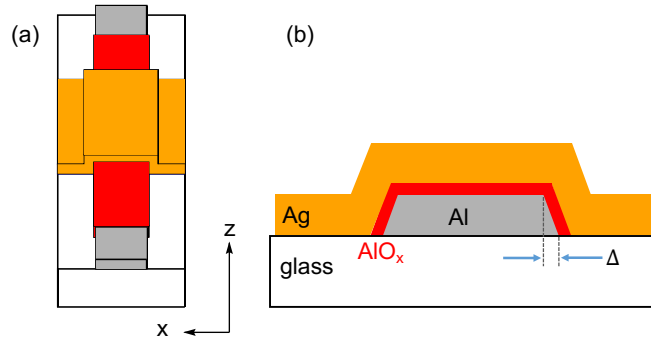


Figure 6.1: Sketches of the MIM samples: **(a)**: Schematic sketch of a MIM device indicating the layer structure as well as the coordinate system **(b)**: Schematic cross sectional view (not drawn to scale) along the x -direction in the middle of the active area (crossing area of bottom and the top electrode); Δ denotes the increase of the film's length due to shadowing effects during the evaporation process. See also [13].

A sketch of the MIM's layer structure and the sample's coordinate system are shown in panel (a) of figure 6.1 with the x -direction chosen to run across the top silver electrode and the z -direction chosen to run along the oxide covered aluminum bottom electrode. A schematic cut through the sample (not drawn to scale) through the center of the active area is visible in panel (b) of the figure, indicating the layer structure. Δ denotes the increase of the electrode's length due to submerging of metal vapor under the evaporation masks. The evaporation masks determine the film's dimensions. Since they are mounted $\approx 3\text{ mm}$ away from the glass substrate and since the thermal evaporation source has a circular opening of 4mm diameter and is mounted $\approx 170\text{ mm}$ away from the sample, the

increase Δ of the film's length can be roughly estimated by $\approx 4 \cdot \frac{3}{170} \text{ mm} = 70 \mu\text{m}$ [13]. Therefore the films increases on each side by $70 \mu\text{m}$. This means that the rectangular shape of the aluminum bottom electrode becomes a trapezoidal shape (as shown exaggeratedly in panel (b) of figure 6.1). These values coincide to findings as reported in [51, 5].

6.1.2 Topography of the sample surface determined using an AFM

The local emission behaviour of samples under electron irradiation may be significantly influenced by the roughness of the sample surface. Therefore the roughness was measured by means of an **atomic-force-microscope** (AFM). The second reason to perform measurements with the AFM was to determine the layer thickness of the films forming the MIM device. The quartz microbalance used to monitor the layer thickness during the evaporation process applied for the fabrication of the samples needs to be calibrated, since it detects a frequency change of an oscillator caused by absorption of material. Therefore the quartz is mounted near the used glass substrate inside the vacuum chamber used for physical vapor desorption of the films. The material growth on the microbalance and on the glass substrate is assumed to be identical so the thickness of adsorbed material on the quartz is proportional to the layer thickness of adsorbed material on the glass substrate.

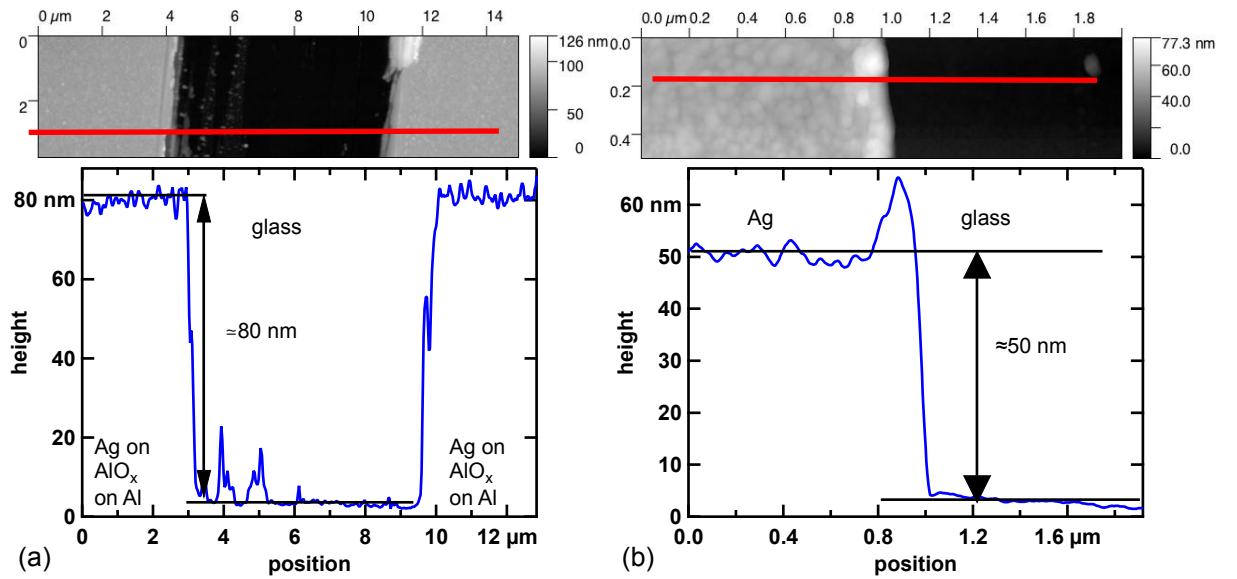


Figure 6.2: **(a) Top panel:** AFM image of a MIM's active area scanned across a scratch; the position of the line-scan **(bottom panel)** is indicated by the red line. **(b) Top panel:** AFM image of the same sample at the step from silver film to the glass substrate; the position of the line-scan **(bottom panel)** is indicated by the red line. See also [13].

The calibration process is performed by measuring the materials layer thickness by means of an **atomic force microscope** (AFM) and comparing this to the frequency change of the microbalance. Therefore the evaporated films a partially scratched away using a steel

needle allowing to measure the layer thickness by taking an AFM line-scan across the fabricated rift. Typical results of such AFM images are shown in the upper parts of figure 6.2, where the red lines indicate the positions, where the line-scans (see lower part of the image) were evaluated.

In panel (a) of figure 6.2, the scan was performed on the active area, where a total sample thickness (excluding the glass substrate) was determined to 80 nm. In panel (b) of figure 6.2, the scan was performed on the silver film outside the active area, where the silver film is directly evaporated onto the glass substrate, indicating a layer thickness of about 50 nm. Combining these two findings, the thickness of the aluminum film can be determined to 30 nm, while the aluminum film thickness is reduced to 27 nm by a consumptive oxidation to form the insulating aluminum oxide film. The layer thickness of the oxide film is determined by the chosen oxidation potential.

The roughness of the surface (RMS) is determined by analyzing AFM line-scans. The results for the silver film within the active area are 1.4 nm (RMS) and 1 nm for the silver film outside the active area. The underlying glass substrate has a roughness (RMS) of 0.2 – 0.3 nm, meaning that all films are fairly flat and the local roughness will not (predominantly) affect the emission behaviour.

6.1.3 Topography of the sample surface determined using an optical microscope

The MIM samples were also examined by means of a Keyence digital optical microscope as shown in figure 6.3. The motivation for this analysis was to study whether the irradiation of the MIM devices by electron beams caused a surface modification. Such a surface modification by local carbon contamination is known in the SEM community and was suspected to cause local changes in the emission behaviour found in the experiments performed for this thesis (as discussed below). In SEM experiments, it is known that carbon compounds produced by polymerization from HFC (hydro fluorocarbons) and from HC (hydrocarbons) under electron bombardment are deposited onto the sample, which was e.g. reported in reference [52]. In panel (c) of figure 6.3, an overview of the MIM device is shown. Upper left: oxide covered aluminum; upper right: silver film within the active area; lower left: glass substrate; lower right: silver film on glass substrate outside the active area. The edge between the active area and the oxide covered aluminum film is indicated by a black line, the one between the silver film within and outside the active area by a red line. Small black structures are visible in all parts of the sample that were frequently irradiated with the electron beam, but not outside the irradiated area. This becomes obvious by examining the silver film outside the active area which does not show any signs of black spots in the lower part far away from the active area, where the sample was, if at all, only rarely irradiated. In panels (a) and (b), the transition between the active area and the oxide covered aluminum (as indicated by the black line in panel (c)) is analyzed by two zoom images. The frayed (laser cut) evaporation masks cause the frayed edge of the film. The length scale is determined to $\approx 3 \mu\text{m}$. Comparing the length scale of the the

transients of several μm with the beam diameter of the electron beam ($\varnothing \approx 0.75 \text{ mm}$) it is found that these edges cannot be resolved in position dependent experiments due to the limited resolution. The determined length scale is in good agreement with the values of some $10 \mu\text{m}$ reported in [5]. A zoom image of the region marked by the red line in (c) is depicted in panel (d), showing visible marks of contamination. The markers were used for measuring the length scale on which the silver film drops from the active area to the silver film on the glass substrate, which was determined to be about $4.6 \mu\text{m}$.

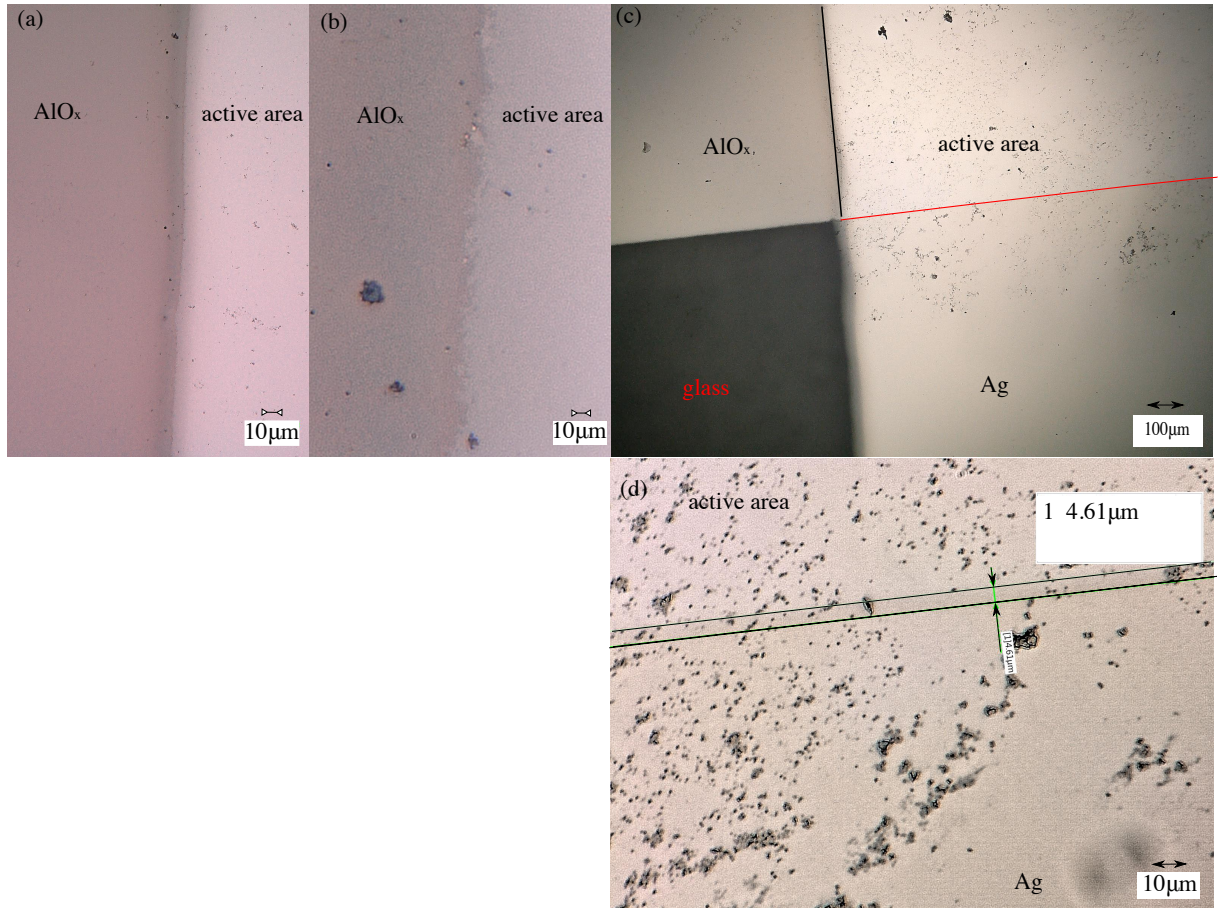


Figure 6.3: Microscopic pictures of an irradiated MIM device taken by a Keyence digital microscope (data: courtesy of J.-C. Knoblich). **(a)** Zoom image of the area marked with the black line in the overview shown in panel (c): transition between the active area and the oxide covered aluminum film; the sharpness of the edge is defined by the sharpness of the evaporation masks. **(b)** like (a), but further zoomed in. **(c)** Overview of the sample. The black line marks the edge between the active area and the AlO_x film; the red line the edge between silver on glass and the active area. **(d)** Zoom image of the edge marked by the red line in (c) showing a transition area of about $4.6 \mu\text{m}$ where the silver film runs out over the edge of the aluminum film. See also [13].

6.1.4 Topography of the sample surface determined using a SEM

During the experiments performed for this thesis, a peculiar behaviour when irradiating a particular spot within the active area was noticed (see section 8.1.2). Along with the known issue of carbon contamination in SEM experiments and the observation of the black dots in panel (b) of figure 6.3, it was suspected that the carbon contamination of the surface might also play a significant role in the low energetic electron experiments here. To further examine this hypothesis, **Scanning Electron Microscope** images of irradiated and non-irradiated MIM samples were taken, which are shown in figure 6.4. Panel (a) shows an image of an irradiated sample, recorded with 900x magnification. Parts of the active area (upper left), of the silver film outside the active area (upper right), of the oxide covered aluminum (lower left) and of the glass substrate (lower right) can be seen. The arrow in the picture indicates a length of $20\mu\text{m}$. The silver film (within as well as outside the active area) and also the oxide covered aluminum film are visible as fairly homogeneous, dark areas, indicating that no surface charge is established due to the irradiation with electrons in the SEM. The bright light-up visible on the transition of the metal films and the glass substrate (lower right part of panel (a)) otherwise indicates, that a surface charge is established on the glass substrate. A temporal evolution of this charge was also observed during the scans. Panel (b) shows a zoom image of the active area taken with a magnification of 10000x. The circular structure (highlighted by the red circle) has a diameter of $3\mu\text{m}$ and is therefore much smaller than the beam diameter of the electron beam ($\varnothing \approx 0.5..0.75\text{ mm}$). In panel (c), an image (recorded with a magnification of 900x) of the silver film outside the irradiated area is shown. On the left edge of the image, a black structure is visible, which represents a part of the conductive carbon cement used to establish the electrical wiring of the sample. No circular structures are visible, though. This means, that the circular structures observed in panels (a) and (b) are clearly induced by the e^- -beam. In panel (c) only a few dust flakes are visible, which are hardly to avoid, since the samples were transported on atmosphere. An overview image of the active area is shown in panel (d), which was recorded with the same magnification of 900x like used for recording the images in panels (a) and (c), showing again visible circular structures, as discussed above. In panel (e) an image of the transition between the active area and the silver on top of the glass substrate is shown, which was recorded using a magnification of 430x. A scratch through the sample is also visible, which was fabricated by a needle to enable AFM measurements of the film thickness. The arrow indicates the length scale of $50\mu\text{m}$. In panel (f), an image of the silver film of a non-irradiated sample is shown, which was recorded with a magnification of 900x. Obviously no circular structures occur; the black item is a dust flake. This proves that the small circular structures are indeed caused by low energetic electron irradiation of the samples.

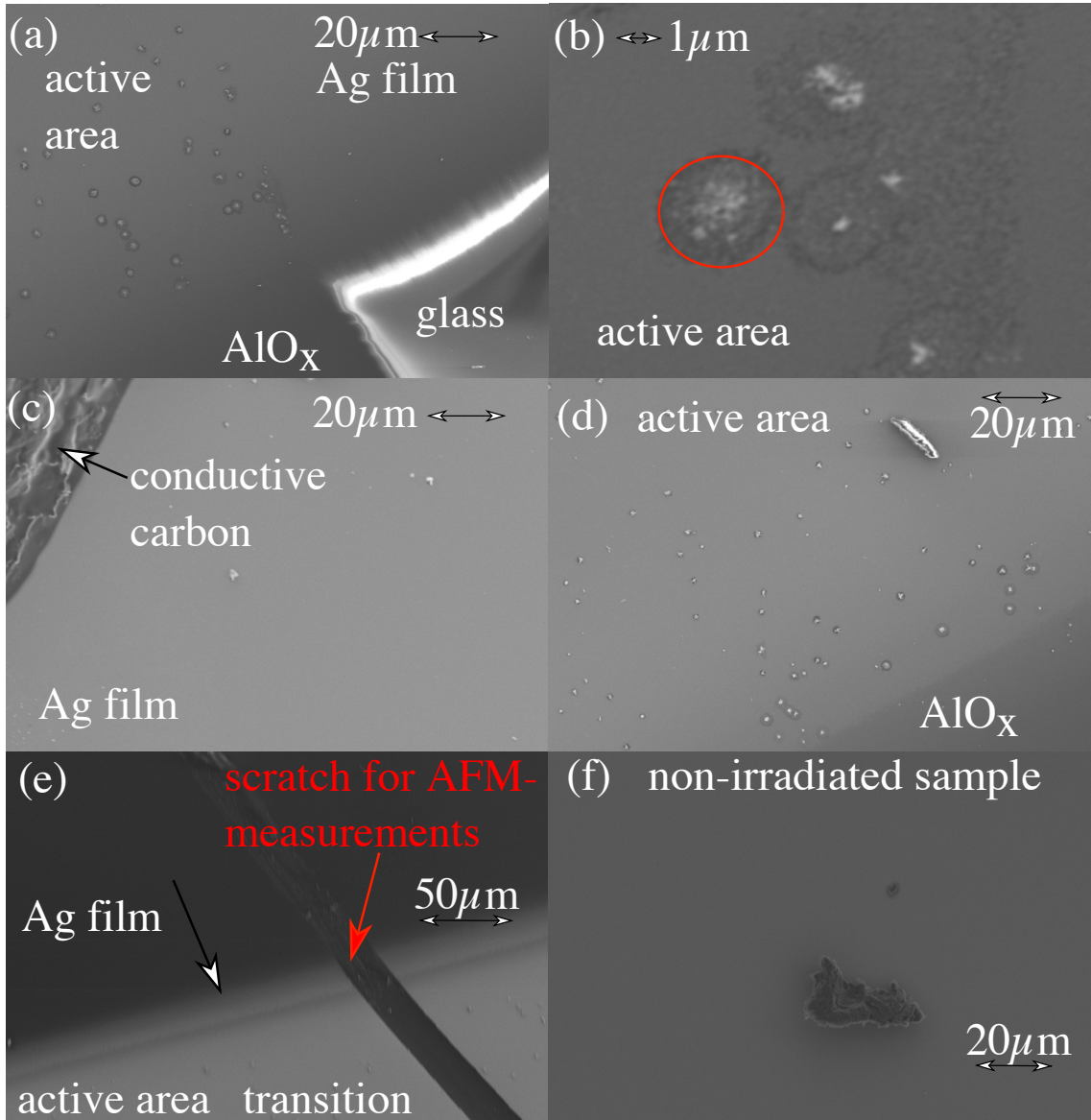


Figure 6.4: SEM images of MIM samples (data courtesy of A. Reichert) **(a)**: Overview (900x magnification) of the overlap between the active area, the silver film and the AlO_x film on the glass substrate, showing visible contamination where the sample was frequently irradiated. **(b)**: Zoom image of the active area (magnification 10000x): Typical diameter of the contamination is 2 μm **(c)**: Image (magnification 900x) of the silver film next to the active area where the sample was rarely irradiated: nearly flat surface without contamination. **(d)**: Image (magnification 900x) of the active area where the sample was frequently irradiated, a rod like dust particle and small circular structures are visible. **(e)**: Image (magnification 430x) of the edge between active area/ silver film of an irradiated sample; a needle scratch made intentionally for AFM thickness measurements is visible. **(f)**: Image (magnification 900x) of the silver film of a non-irradiated sample showing dust flakes, but no circular structures.

6.2 Measuring modes

The currents into the different electrodes of the irradiated MIM device were measured using the current-monitoring input of a potentiostat (Heka PG 510). If the current into the top silver or bottom aluminum electrode of the MIM is measured, the experiment mode is called "**probe top**" or "**probe bottom**", respectively.

In the *probe top* mode, the top silver electrode of the MIM is connected to the "working" input of the potentiostat, to measure the current into the top electrode, while the aluminum bottom electrode of the MIM is connected to the bridged "counter" and "reference" input of the potentiostat. Therefore, the bottom electrode is set to the desired potential (of usually 0 V or to the chosen bias voltage), while the current into the grounded top silver electrode is measured by the potentiostat's internal I/U converter. This way, the potentiostat acts as high-precision voltage source connected to the bottom- and as I/U converter connected to the top electrode. The *probe bottom* mode can be described in the same way, but in this case the *top* silver electrode is connected to the voltage source and the *bottom* aluminum electrode to the I/U converter. Both measuring modes are depicted in figure 6.5, where the current meter input is symbolized by an ammeter and the high-precision voltage source by a function generator. In order to vary the impact point of the focused electron beam on the surface of the MIM device, the sample was moved either in *x*- or *z*-direction. The blue dotted lines thereby indicate the path, at which the sample was steered during the experiments.

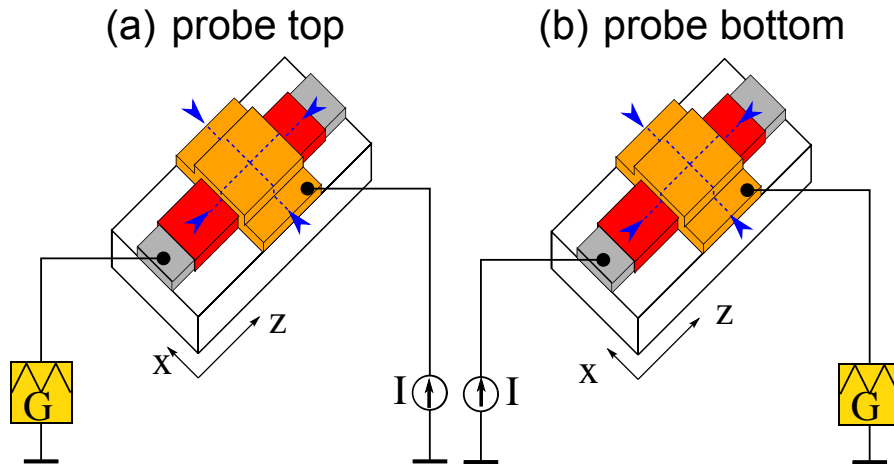


Figure 6.5: Different measuring modes used for MIM samples: (a): *probe top* mode where the silver top electrode is metered with the current meter input of the potentiostat, while the bottom aluminum electrode is connected to the bridged counter-/reference inputs and kept at virtual ground. The *x*-coordinate is chosen to run along the silver film and the *z*-coordinate along the aluminum film. The blue dashed lines indicate the path the sample is steered during the electron irradiation. (b): Same as (a), but in the *probe bottom* mode, where the bottom electrode is metered and the top electrode kept at virtual ground. Taken from [13].

As discussed in section 7.4, in principle the potentiostat could be replaced by an I/U-converter without significantly changing the results (see figure 7.12). In the past, the *probe bottom* mode was the only established measuring mode during the experiments with MIM devices (e.g. see [2]). The *probe top* mode was established here to examine the external emission behaviour of the samples as well. Both measuring modes are used throughout the experiments described in the remainder of this work, regardless if an external collector/repeller electrode was used or not.

6.3 Set-up for experiments without external collector/repeller electrode

The wiring is sketched in figure 6.6 (shown here: *probe top* mode).

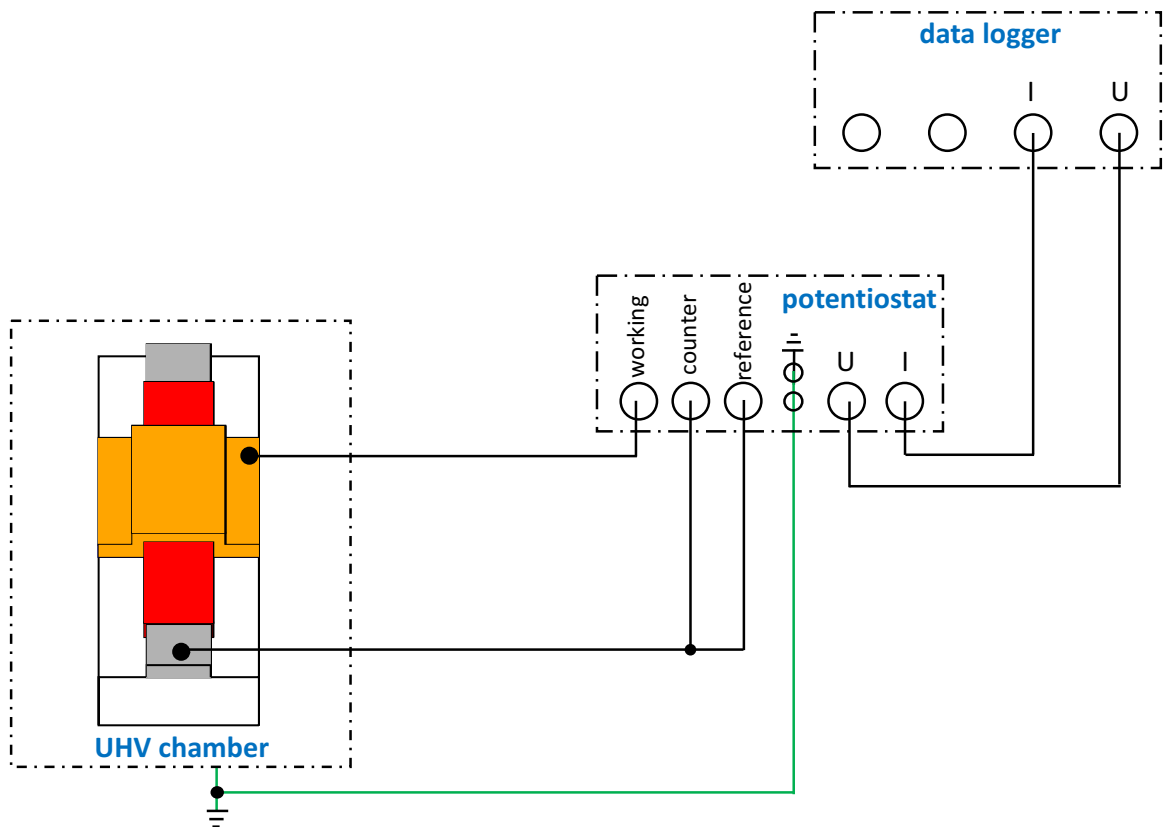


Figure 6.6: Wiring diagram in case no external collector/repeller electrode is installed.

The chosen potential applied to the non-metered electrode is read out via the voltage output of the potentiostat, while the measured current into the metered electrode is read out via the current output of the potentiostat. Both are connected to individual channels of an USB oscilloscope (PicoScope 3425) used as data-logger and stored. The ground input of the potentiostat as well as its chassis are connected to the ground of the UHV chamber.

6.4 Set-up for experiments with additional collector/repeller electrode

As already explained in the introduction, a second set of experiment was performed which was triggered by the first set of experiments. In the second set, an additional collector/repeller electrode was installed to control the electric field above the sample, which is established by the application of a voltage U_d to the external electrode. The collector/repeller has the shape of a half-tube and is made of aluminum with the dimensions in x -direction of 20 mm, in z -direction of 15 mm and with a radius of the tube of 10 mm. A slit of the width in x -direction of ≈ 15 mm and in z -direction of 5 mm is milled in the electrode to allow primary electrons to travel unobstructed towards the sample. The collector/repeller electrode was constructed this way since it does not apply metal grids within the beam path, which are a possible source of low energy secondary electrons when irradiated by the electron beam. In ion-irradiation experiments, this is often acceptable, but in case of electron irradiation experiments, additional secondary electrons would significantly influence the experimental findings due to a modified energy distribution of the electrons impinging on the sample.

The experiments with external collector/repeller electrode apply the same samples, the same instrumentation as well as the same measuring modes as before, therefore the set-up as well as the nomenclature are identical to the ones used before. The motivation for the application of an external electrode was to control externally emitted electrons, which were suspected to influence the measurements (see chapter 7.8). By biasing the collector/repeller electrode, an electric field above the sample is established which allows, depending on the collector/repeller potential U_d , to repel emitted electrons towards the sample ($U_d < 0$ V) or to accelerate them away from the sample ($U_d > 0$ V). A biased collector/repeller electrode effectively prevents the built-up of a space charge above the sample. Moreover, by measuring the current I_d into the electrode, an additional measuring mode is available.

Due to the fact that not only low energy secondary electrons are emitted, when an energetic electron beam impinges onto a surface, but also quasi-elastically backscattered electrons with up to the primary energy leave the surface, in principle an electric field of almost the acceleration voltage of the primary electrons would be needed to fully repel these backscattered electrons to the sample. Such a field, however, would have severe influence on the primary electron energy and on the focal properties of the primary electron beam. Therefore, the electric field established here is provided by the application of a voltage up to $U_d = \pm 40$ V, which is a compromise between the voltage necessary to drain/repel all secondary electrons on the one hand and between a reduction of the primary kinetic energy and de-focusing of the primary electron beam on the other hand. As will be shown later (see figures 8.10, 8.11 and 8.12), the electric field applied here is sufficient to drain/to repel all electrons in all cases, except if the oxide covered aluminum is irradiated. However, the influence of the external electric field to the backscattered electrons is negligible. The issues arising from this fact are also discussed in section 6.9, since the drawback of the presence of such an electrode is the fact, that the collector/repeller electrode may become a source

of electrons as well. If backscattered electrons impinge on the external electrode, they will cause the emission of tertiary electrons and may also possibly cause backscattered electrons leaving the external electrode's surface. In case of $U_d > 0V$, these *tertiary electrons* are held back, in case of $U_d < 0V$, the *tertiary electrons* are accelerated towards the sample (holder) by the electrical field between sample and collector/repeller.

A schematic of the set-up for these measurements is depicted in figure 6.7, the measuring modes as well as the coordinate system are identical to the nomenclature used before.

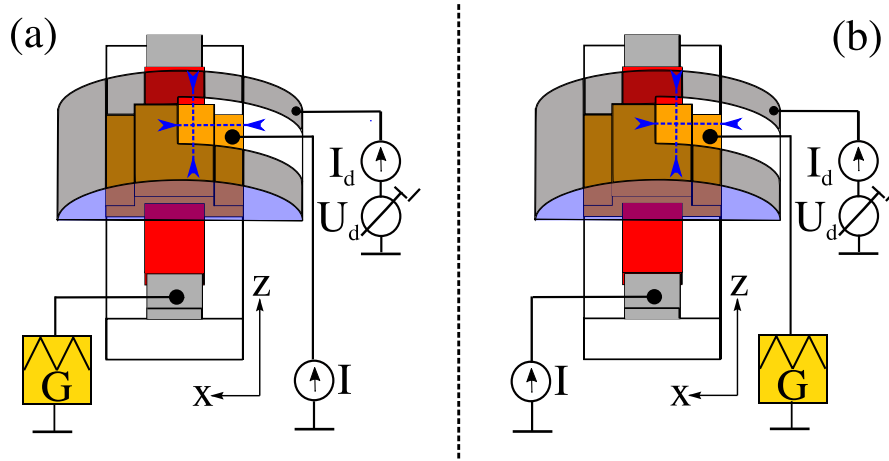


Figure 6.7: Schematic of the set-up of experiments with collector/repeller electrode: **(a)** *probe top* mode where the current to the silver top electrode is measured while keeping the aluminum bottom electrode at a constant potential; the collector/repeller electrode is kept at U_d while metering the current I_d to the electrode. The sample is either moved horizontally in x -direction or vertically in z -direction symbolized by the blue dashed lines while detecting all currents as function of the momentary beam position. **(b)** same as (a), but in the *probe bottom* mode, where the current into the aluminum bottom electrode is measured and the silver top electrode being kept at a constant potential. See [14].

The wiring of the MIM device is identical to the one described in section 6.3 before. The collector/repeller voltage U_d is generated by two interconnected power supplies wired like shown in figure 6.8 to build a zero-crossing power supply, which allows to choose the voltage in the interval from $-42 V.. +42 V$ by an external potentiometer. The bridged output of the power supply is the 0 V-pole of the potentiostat and is also connected to the ground of the UHV-chamber. The picoammeter (Keithley 6487) used to measure the current I_d onto the collector/repeller electrode, floats on U_d . U_d as well as I_d are data logged by the USB oscilloscope as described above.

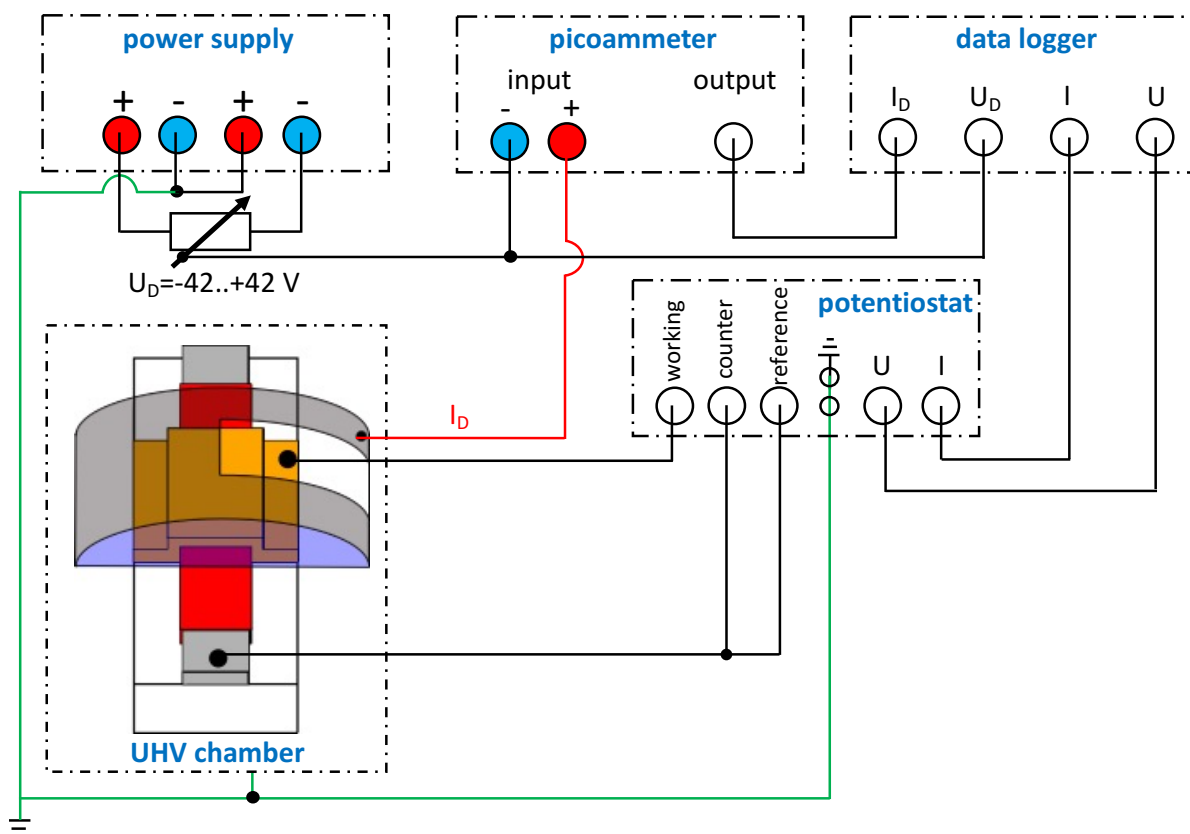


Figure 6.8: Wiring diagram in case of measurements as function of the collector/repeller voltage U_d .

6.5 External setup

The overall setup is shown in figure 6.9. The numbers in the photograph denote the following parts of the experimental setup: (1) UHV chamber, (2) viewport towards the sample, (3) electron gun, (4-7): rotatable x - y - z -manipulator: (4) micrometer measuring screw for the y -direction, (5) like (4) for the x -direction, (6) measuring screw for the z -direction, (7) voltage feed-throughs, (8) turbo molecular pump, (9) potentiostat, (10) data logger, (11) vacuum gauge controller, (12) residual gas analyzer, (13) ion gun. The configuration shown in the photograph was modified in comparison to the configuration for the electron experiments by adding an ion gun and rotating the sample manipulator by 45° . The base pressure is in the order of $9 \cdot 10^{-9} \text{ mbar}$.

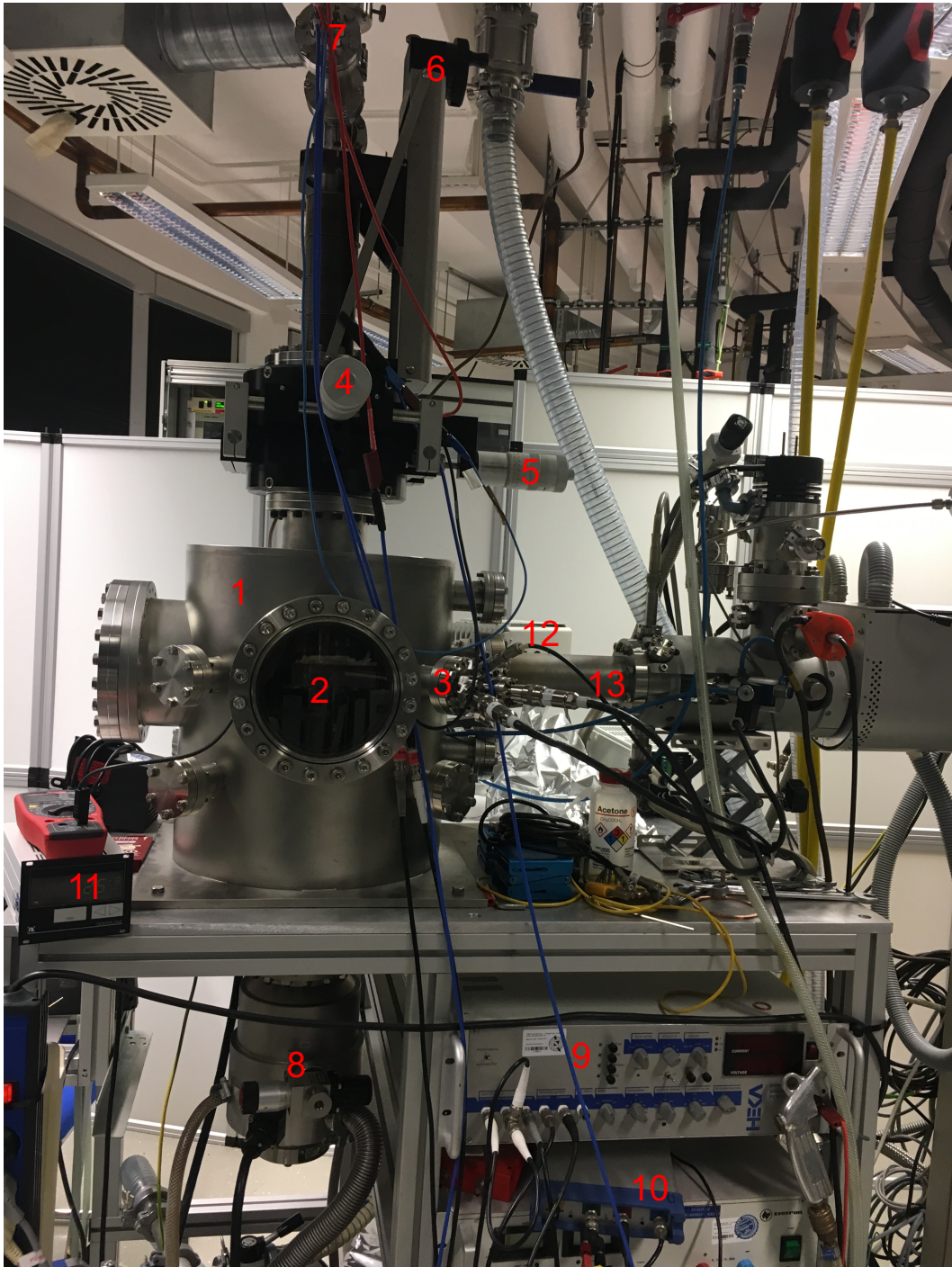


Figure 6.9: Photograph of the ultra high vacuum chamber and the equipment related to the MIM experiments. The numbers in the photograph denote: (1) UHV chamber, (2) view port towards the sample, (3) electron gun, (4-7): rotatable $x-y-z$ -manipulator:(4) micrometer measuring screw for the y -direction, (5) like (4) for the x -direction, (6) measuring screw for the z -direction, (7) voltage feed-throughs, (8) turbo molecular pump, (9) potentiostat, (10) data logger, (11) vacuum gauge controller, (12) residual gas analyzer, (13) ion gun

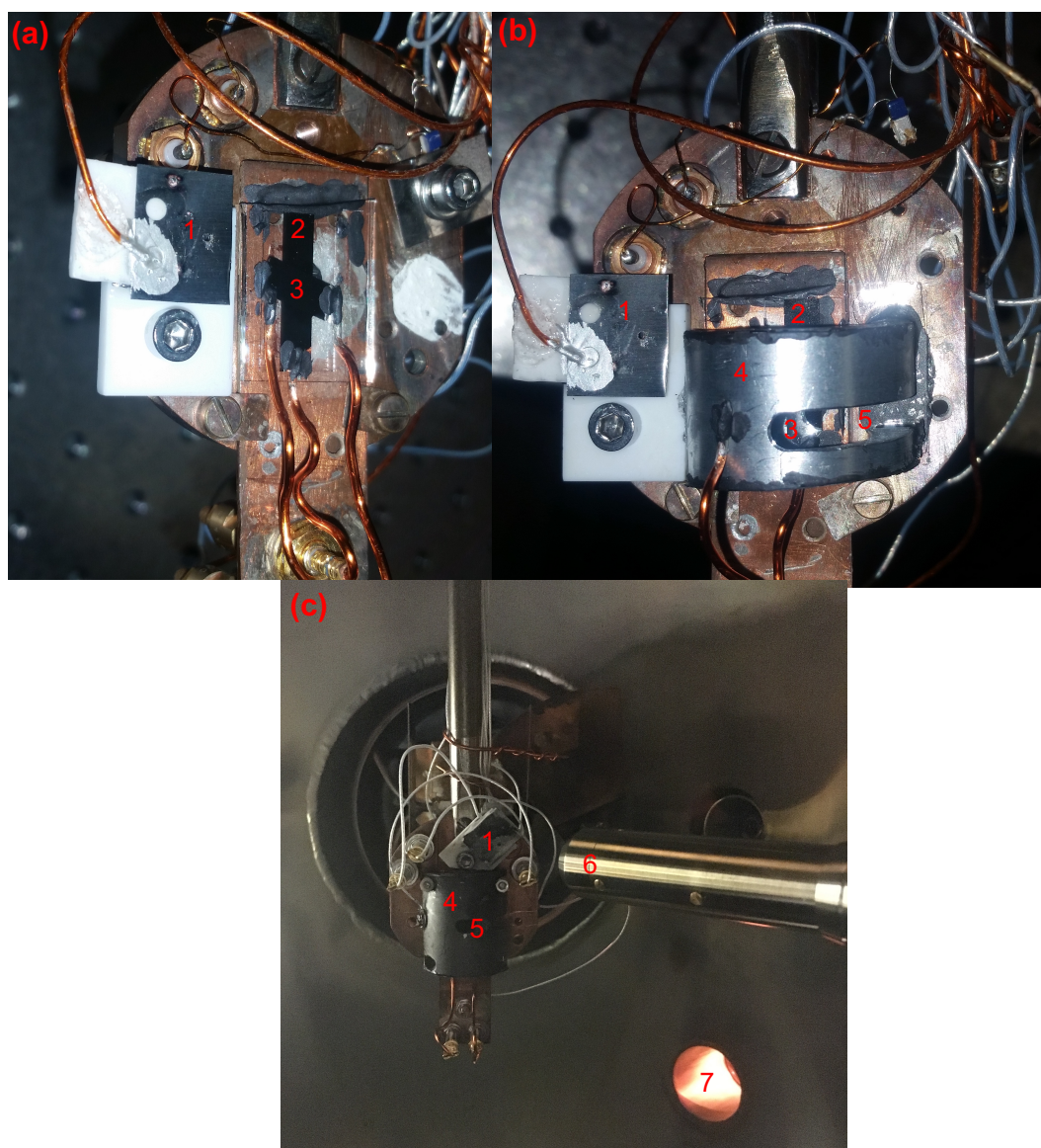


Figure 6.10: **(a-c)**: Photographs of the sample holder **(a)**: Typical configuration for the experiments without external collector/repeller electrode. The numbers denote: (1) front shield of the Faraday cup (FC) with entrance hole, (2) oxide covered aluminum electrode of the MIM, (3) active area of the MIM. **(b)**: Typical configuration for the experiments with external collector/repeller electrode. The numbers denote: (1) front shield of the Faraday cup (FC) with entrance hole, (2) oxide covered aluminum electrode of the MIM, (3) active area of the MIM, (4) collector/repeller electrode, (5) slit. **(c)**: Typical configuration for the experiments with external collector/repeller electrode mounted inside the UHV vessel. The numbers denote: (1) front shield of the Faraday cup (FC) with entrance hole, (4) collector/repeller electrode, (5) slit, (6) electron gun, (7) vacuum gauge.

In figure 6.10 images of the mounted MIM samples are shown, which are isolated by the glass substrate against the walls of the vacuum vessel. Panel (a) shows a typical configuration for the experiments without external collector/repeller electrode. The numbers denote: (1) front shield of the Faraday cup (FC) with entrance hole, (2) oxide covered aluminum electrode of the MIM and (3) active area of the MIM. In panel (b), the configuration for the experiments with external collector/repeller electrode is shown. The numbers denote: (1) front shield of the Faraday cup (FC) with entrance hole, (2) oxide covered aluminum electrode of the MIM, (3) active area of the MIM, (4) collector/repeller electrode and (5) slit. In panel (c) the typical configuration for the experiments with external collector/repeller electrode mounted inside the UHV vessel is shown. The numbers denote: (1) front shield of the Faraday cup (FC) with entrance hole, (4) collector/repeller electrode, (5) slit, (6) electron gun, (7) vacuum gauge.

6.6 Energy levels inside the MIM and their shift due to an internal bias voltage

The insulating oxide film between the MIM's metal films may act as a tunnel barrier, when either higher voltages between the MIM electrodes are applied [43, 50] or a transport of non-ground-state electrons (and holes) is involved [6, 53]. The theory behind this observed behaviour is discussed in formula 5.15 in section 5.3.

A tunnel barrier formed by a thin oxide film is different from barriers commonly described in theoretical physics or in the **Scanning Tunneling Microscope** [54], since these barriers allow tunneling of only one species (in case of the STM only of electrons), while tunneling through an oxide film is possible for two types of charge carriers, namely here for electrons and for holes [9]. Electrons and holes have thereby different barrier heights: The barrier height for an electron is given by the energy difference between the Fermi level of the metal and the lower edge of the metal oxide's conduction band, while the barrier height for holes is determined by the energy difference to the upper edge of the valence band.

The transport of excited charge carriers generated by different processes (for instance a chemical surface reaction or the impact of an energetic particle) was already studied using metal-insulator-metal junctions [2, 7]. As stated above, these studies worked with the hypothesis that the current between the top and the bottom electrode induced by the electronic excitation produced in one of the two metal electrodes is evoked by the *internal* transport of excited electrons or holes through the *internal* buried oxide barrier. To verify this hypothesis, further experiments were performed with the application of a bias voltage between the top and the bottom electrode of the MIM. If the oxide barrier is on the one hand thick enough to sufficiently suppress the dc bias current induced by the bias voltage, but on the other hand also thin enough to allow a detectable current of hot charge carriers, in principle a bias voltage dependence of the *internal* currents should be observed, because a bias voltage changes the ratio of the hole and of the electron transport in the whole hot

carrier transport [9]. This was indeed observed and therefore the hypothesis of an *internal* transport was further verified [4, 9, 55, 56, 57].

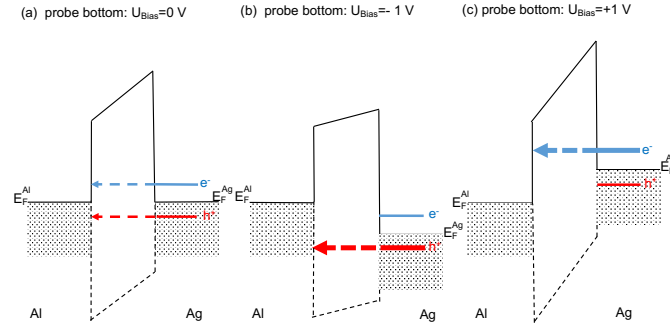


Figure 6.11: **(a)**: Energy levels in the MIM device at 0 V bias voltage between silver top and aluminum bottom electrode. **(b)**: A negative bias voltage on the bottom electrode acts as retarding field for excited electrons in the top electrode and eases the transport of excited holes. **(c)**: A positive bias voltage on the bottom electrode acts as retarding field for excited holes in the top electrode and eases the transport of excited electrons.

The specific influence of a bias voltage on the hole and electron transport can be explained by a bias-induced modification of the two-band tunnel barrier as sketched in figure 6.11. In case of 0 V bias (panel (a)) and excitation of the silver electrode, the *internal* current from the excited silver towards the non-excited aluminum electrode may consist of both e^- and h^+ currents with opposite polarity. By applying a bias voltage, the potential of the silver electrode is shifted up- or downwards with respect to that of the aluminum electrode. By convention, we define the polarity of the bias voltage such that a negative bias acts as a retarding field for the excited electrons and therefore decreases the electron current while simultaneously increasing the hole current crossing the tunneling barrier. For excitation of the top silver film and the current measured in *probe bottom* mode, this situation is depicted in panel (b) of figure 6.11. The situation for a positive bias voltage is sketched in panel (c) where the bias now acts as a retarding field for excited holes, while the transport of excited electrons is eased.

To simplify the figure, an *internal* electric field across the oxide due to dipole layers at the oxide interfaces as discussed in detail in [56] is not taken into account in figure 6.11.

In the previous experiments using MIM devices, the *probe bottom* mode was applied to gather information about an excited electron transport (e.g. references [2, 12, 57]) induced by ion impact onto the silver electrode surface. In the present experiments using electron excitation, also experiments in the *probe top* mode were performed.

Starting with experiments without external collector/repeller electrode, that again challenged the hypothesis of *internal* transport [13] (section 7.6), experiments as a function of the *internal* electric field (due to varied bias voltage) in combination with an external electric field (due to an applied collector/repeller voltage) were performed, which are in detail described in section 8.2.4.

6.7 Properties of the electron beam

The e^- -beam used for irradiating experiments was generated by a commercial ELG-2 electron gun by Kimball Physics. Although this electron source is in principle also suitable to produce low-energetic electron beams with kinetic energies below 50 eV, the measurements in that energy range were found to be experimentally challenging. Either the current measurement of the primary current was error-prone or the beam focusing did not work well enough to guarantee a stable primary e^- -beam. These difficulties which may be caused by the fairly high working distance of about 10cm used in the first set of experiments. However, a reduction to about 2 cm was tried when starting experiments with external collector/repeller electrode without much success regarding the low energy focus.

Therefore only measurements in the energy range from 75..1000 eV were evaluated here. Although the beam could in principle be pulsed, a DC operation was chosen since this avoids issues arising from measurements of small pulsed currents. The samples were also found to be stable enough, so that a continuous operation during the experiments did not significantly affect the lifetime of the samples (which was several months for each sample).

The primary electron current was measured in a custom built *Faraday Cup* (in the following referred to as "FC") consisting of tantalum back electrode, an insulator made of 5 mm Macor ceramics, and a molybdenum front electrode with a laser-cut hole of $\varnothing \approx 0.75$ mm diameter. Front and back electrode of the FC were independently connected to voltage feed-throughs and electrically isolated against the sample as well as against the manipulator.

The impact point of the electron beam was determined using the FC. For that purpose, the FC front and back electrode were individually read out using two picoammeters. At first the current onto the FC front was maximized, followed by maximizing the current into the FC *i)* by shifting the manipulator and *ii)* by optimizing the lens parameters of the electron gun. The goal was to maximize the current into the FC and to minimize the current to the FC front electrode. If the beam diameter was smaller than the diameter of the FC entrance hole, an *x*- or *z*-scan across the entrance hole provided a pretty exact information about the impact point as well as about the beam diameter. For an exact measurement of the primary electron current in the FC, the FC front electrode was biased to repel all secondary electrons emitted from the FC electrode back to the FC electrode. By doing this, a measurement of the primary electron current is provided. Since the lateral dimensions of the MIM devices are on the mm-scale, a maximal spot size of 1mm was found acceptable. As visible in figure 6.12, a beam diameter of that order of magnitude was achieved in all cases. The blue curves in figure 6.12 correspond to measurements on the FC_{front} -, the red curves to measurements on the FC-electrode. The FC electrode is only irradiated, if the electron beam penetrates the FC via the small entrance hole in the center of the front electrode. The current to the front electrode decreases in case the electron beam penetrates the entrance hole, while simultaneously the current to the FC electrode increases. Only in case of 750 eV (panel (c) of the figure) a clear plateau is visible

in on the red curve, indicating that the beam diameter of the electron beam is smaller than the entrance hole of the FC. In all other cases, the beam diameter was $\varnothing \geq 0.75\text{mm}$ which was found to be sufficient for the experiments discussed here. The primary electron current was kept in the range of 10 – 40 nA for all kinetic energies, the beam diameter was chosen as small as possible.

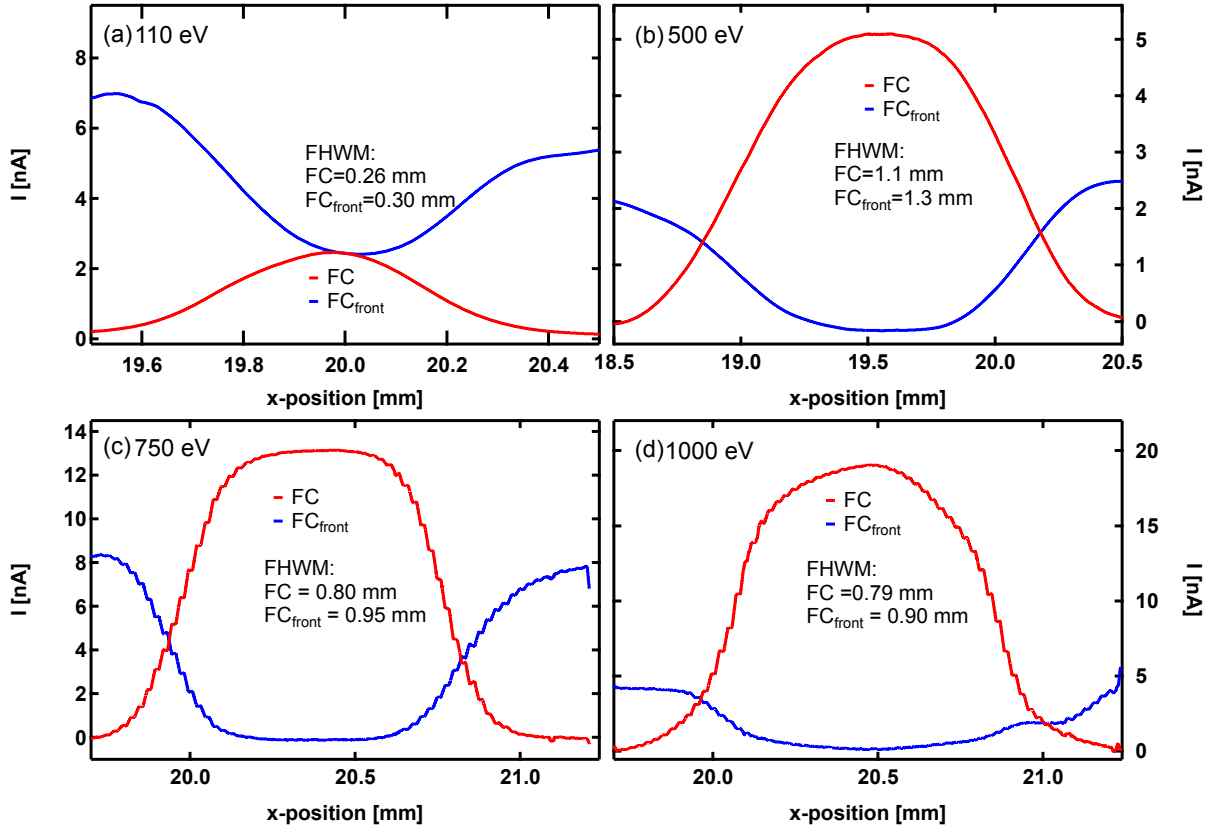


Figure 6.12: Current measured on the FC_{front} – and into the FC as function of the x -position: panel (a) for 110 eV, panel (b) for 500 eV, panel (c) for 750 eV and panel (d) for 1000 eV.

6.8 Irradiation scenarios without external collector/repeller electrode

As discussed above, measurements in *probe top* and *probe bottom* mode are possible, which cause in combination with different applied impact points three different irradiation scenarios depicted in figure 6.13. Panel (a) of the figure shows a schematic cross-sectional view in x -direction through the center of the active area. During x -scans, an irradiation of the silver film within (labelled with (1)) and outside the active area (labelled with (2)), respectively, is possible. As shown in the table in the figure, the irradiation of positions (1) and (2) correspond to a *direct* experiment in the *probe top* and to an *indirect* experiment in the *probe top* mode. Panel (b) of the figure shows a schematic cross-sectional

view in z -direction through the center of the aluminum film. During z -scans, an irradiation of the silver film within the active area (labelled with (1)) and of the oxide covered aluminum film (labelled with (3)) is possible. As shown in the table in the figure, the irradiation of positions (1) correspond to a *direct* experiment in the *probe top* and to an *indirect* experiment in the *probe top* mode, while the irradiation of position (3) is a *direct* experiment in the *probe bottom* and an *indirect* experiment in the *probe top* mode. The possible combinations are also shown in the table.

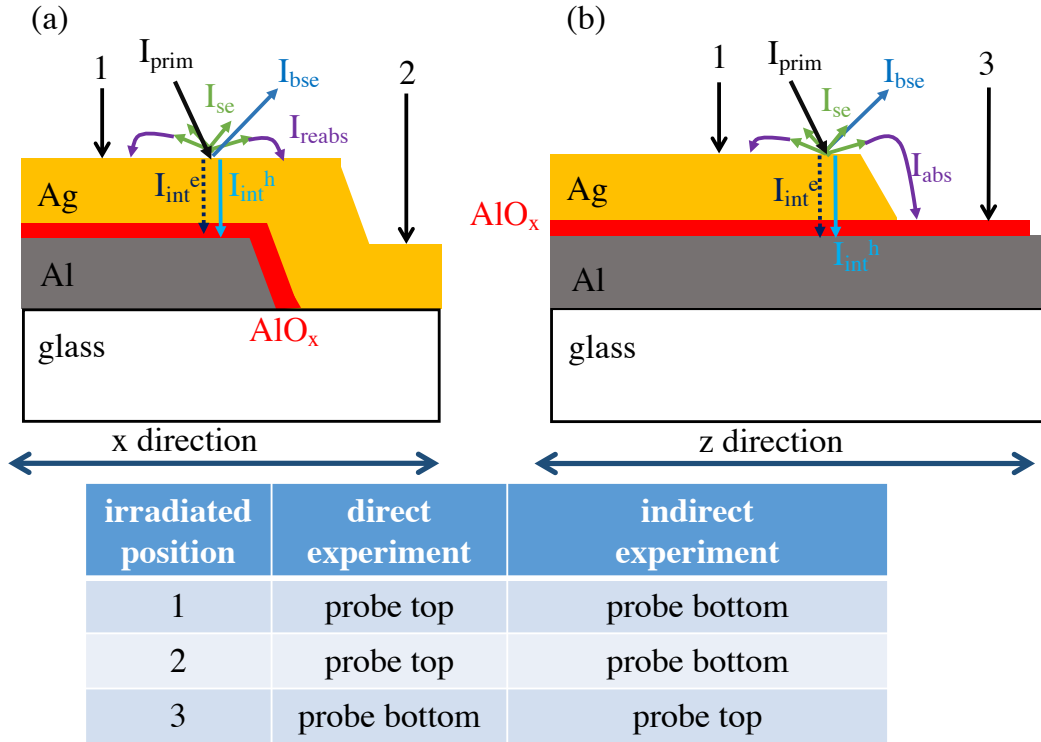


Figure 6.13: Schematic of the different irradiation/detection scenarios: (a): Schematic cross-sectional view in x -direction across the active area. (b): Schematic cross-sectional view in z -direction across the aluminum film. Currents are explained in section 6.10. The table explains, which combination of irradiated position and measuring mode corresponds to *direct* and which to *indirect* experiments. See also [13].

The following nomenclature of possible current contributions is used throughout this thesis:

The following contributions may in principle also appear in bulk samples:

- I_{prim} : **p**rimar**y** **e**lectron current impinging on the surface
- I_{se} : **s**ecund**y** **e**lectron current evoking from the irradiated surface due to the irradiation with I_{prim}

- I_{bse} : **back scattered electron** current evoking from primary electrons reflected at or near the vacuum/solid interface
- I_{reabs} **reabsorption** current of electrons that are reflected towards the irradiated surface (e.g. due to an electric field above the surface established by space charge)

The following contributions appear exclusively in multi-layer samples:

- I_{int} : **internal** current across the barrier consisting of:
 - I_{int}^e : **internally transported electrons**
 - I_{int}^h : **internally transported holes**
- I_{abs} : (cross-) **absorbed** electrons evoking from the irradiated surface circumventing the internal barrier and entering the non-irradiated electrode

6.9 Irradiation scenarios with external collector/repeller electrode

In the experiments with a controlled electric field above the sample established by the application of a voltage U_d to the external electrode, the same MIM devices as before were used. Therefore, the irradiation spots (1-3) and the schematic cross-sectional views as introduced in figure 6.13 are used to characterize the processes here as well. Due to the half-tube shape of the collector/repeller electrode mounted parallel to the z -direction, the shape in the cross-sectional view of the external electrode depends on the scan direction. As shown in figure 6.14, by scans in x -direction the electrode appears as quarter-circle (see panels (a) and (b)), while it appears with rectangular shape in z -scans.

In addition to the current contributions introduced in the preceding section, the collector/repeller electrode will be hit by electrons and may therefore become a source of tertiary electrons causing the current I_{te} .

In panel (a) of figure 6.14, the situation is sketched for x -scans with a positive voltage U_d applied to the external electrode, which therefore acts as collector and suppresses reabsorption processes. In panel (b), the situation is sketched for x -scans with a negative voltage U_d applied to the external electrode, which therefore acts as repeller and also as source of tertiary electrons. This manifests in the occurrence of the currents I_{reabs} and I_{te} . In panel (c) of the figure, the situation for z -scans at a positive voltage U_d is shown, where also the oxide covered aluminum may be irradiated. In panel (d) of the figure, the situation for z -scans at a negative voltage U_d is shown, where in addition to I_{reabs} and I_{te} also a cross-absorption current I_{abs} may arise.

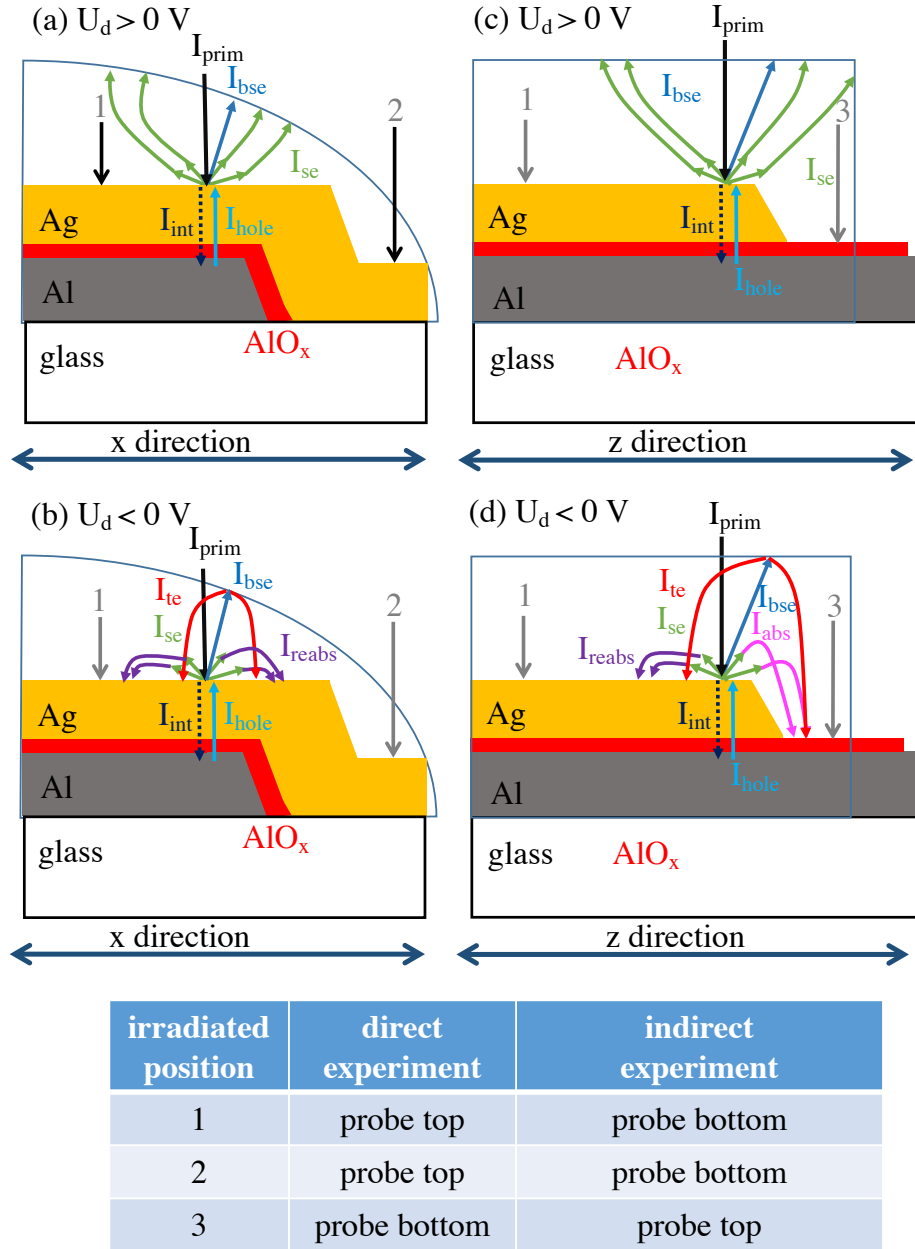


Figure 6.14: Schematic of the irradiation scenarios and the resulting current contributions to the measured sample current: (a) current contributions and possible irradiation spots during x -scans for collector/repeller voltages $U_d > 0$ V; (b) same as (a) for collector/repeller voltages $U_d < 0$ V; (c) during z -scans for collector/repeller voltages $U_d > 0$ V; (d) like (c) for collector/repeller voltages $U_d < 0$ V. Taken from [14].

Since the externally applied collector/repeller voltage influences significantly the possible current contributions to the measured sample currents, a nomenclature is introduced here, which clearly indicates the respective mode: In case that the collector/repeller voltage $U_d > 0$ V, the superscript is "+" is used and "-" otherwise for both the *direct* and the **indirect** measurements. This leads to the assignments I_{dir}^+ , I_{indir}^+ , I_{dir}^- and I_{indir}^- . The current I_d onto the collector/repeller electrode can also be measured. Depending on U_d , the nomenclature I_d^+ and I_d^- is used.

6.10 Interpretation of measured currents

6.10.1 Possible contributions to measured current without external collector/repeller electrode in *direct* and in *indirect* experiments

As already discussed in section 4, the total external emission yield is given by equation 4.1 with contributions of backscattered electrons η and of secondary electrons δ , while δ may have contributions of secondary electrons produced by primary electrons (in the literature referred to as $SE_1 = \delta_0$) and of secondary electrons produced by backscattered primary electrons ($SE_2 = \delta_1$), which is according to [18] negligible here. To distinguish between the contributions to ζ , an external field above the sample would be needed, which is not available in this set of experiments. Due to the fact, that no bulk samples but MIM devices with internal barrier are used, additional contributions to measured currents have to be considered, which are shown in figure 6.13 on page 39.

As also stated above, if the current metered electrode is also the irradiated electrode, this is called a *direct* experiment, and the measured current into the irradiated electrode is given by [14]

$$I_{\text{dir}} = I_{\text{prim}} - I_{\text{ext}} - I_{\text{int}} + I_{\text{reabs}} \quad (6.1)$$

In *indirect* measurements, where the non-irradiated electrode is metered, the measured current is determined by the emission behavior of the sample and consists of the following contributions [14] :

$$I_{\text{indir}} = I_{\text{int}} + I_{\text{abs}} \quad (6.2)$$

The primary electron current I_{prim} and the internal current I_{int} were defined before; the latter depends on the contributions [14]

$$I_{\text{int}} = I_{\text{int}}^e - I_{\text{int}}^h, \quad (6.3)$$

while the **external** current depends on the emission processes from the sample and contains the contributions [14]

$$I_{\text{ext}} = I_{\text{se}} + I_{\text{bse}}. \quad (6.4)$$

As shown in figure 6.13 and defined above, two currents may arise, if the volume above the surface is not field-free:

- I_{reabs} effectively lowers the measured current I_{ext} . Due to the limited field strength, it will affect predominantly low-energy electrons (secondary electrons). The probability P_{reabs} , that an emitted electron will be reabsorbed, depends on the I_{prim} , is of course in the range of $0 < P_{\text{reabs}} \leq 1$ and is defined by $I_{\text{reabs}} = I_{\text{prim}} \cdot \delta \cdot P_{\text{reabs}}$ (see [13]).

- The probability, that an externally emitted electron is absorbed in the non-irradiated electrode and circumvents thereby the internal barrier while contributing to the current I_{abs} , is called P_{abs} . The absorption current is therefore defined by the equation $I_{\text{abs}} = I_{\text{prim}} \cdot \delta \cdot P_{\text{abs}}$. A current I_{abs} thereby apparently increases the current I_{int}^e and decreases I_{int}^h .
- A reabsorption/cross-absorption from the irradiated bottom to the non-irradiated top electrode is not depicted in 6.13, although it is in principle possible in case of irradiation on position (3).

The local emission behaviour of the sample is determined by the atomic number of the target material, the local surface chemistry and the local surface roughness, which influence I_{se} and I_{bse} . Since I_{abs} and I_{reabs} depend on the density of electrons above the surface, both quantities therefore depend on I_{se} and I_{bse} . Especially in case that electrons impinge on insulators (in the experiments either on the glass substrate or on the oxide film on top of the aluminum), a local surface charging may occur, which influences the externally mediated processes of the I_{abs} and I_{reabs} . In case of a direct penetration of electrons through top silver and oxide film into the bottom aluminum electrode would influence the *internal* current, but is negligible in the energy range used here, which will be shown in section 7.2 below.

- If $\frac{I_{\text{dir}}}{I_{\text{prim}}} \approx 1$, the following situations are possible:
 - I_{ext} is negligible.
 - I_{reabs} and I_{ext} cancel each other.
 - I_{int}^h is strong enough to counterbalance I_{int}^e and I_{ext} .
 - Combining 6.1 with 6.4 and 6.3 with the finding, that $I_{\text{dir}} \approx I_{\text{prim}}$, leads to $I_{\text{int}}^h + I_{\text{reabs}} = I_{\text{se}} + I_{\text{bse}} + I_{\text{int}}^e$.
- If $\frac{I_{\text{dir}}}{I_{\text{prim}}} = 0$, the internal and external emission currents cancel each other and therefore 6.1 combined with equations 6.4 and 6.3 yields in $I_{\text{prim}} + I_{\text{int}}^h + I_{\text{reabs}} = I_{\text{se}} + I_{\text{bse}} + I_{\text{int}}^e$
- If $\frac{I_{\text{dir}}}{I_{\text{prim}}} < 0$, the internal and external emission currents overbalance the impinging currents, therefore equations 6.1, 6.4 and 6.3 can be combined to $I_{\text{prim}} + I_{\text{int}}^h + I_{\text{reabs}} < I_{\text{se}} + I_{\text{bse}} + I_{\text{int}}^e$

In *indirect* measurements with primary impact energies ≤ 1 eV and layer structures as applied here, a direct penetration of the non-irradiated electrode by primaries is improbable, therefore I_{int} is actually the current of excited electrons generated within the irradiated electrode, flowing across the barrier. The current measured into the non irradiated electrode is therefore dominated by electrons and holes excited through the irradiation of the top silver electrode plus the contribution of I_{abs} .

The measured current I_{dir} can also be used to calculate the *direct* emission yield

$$\Gamma_{\text{dir}} = 1 - \frac{I_{\text{dir}}}{I_{\text{prim}}} \quad (6.5)$$

The *direct* emission yield Γ_{dir} defined this way describes the net number of negative elementary charges *leaving* the irradiated electrode per primary electron impact. Since in these *direct* experiments also *internal* processes may be involved, Γ_{dir} is in general not equal to the total external emission yield ζ or to Γ_{ext} .

The currents measured in *indirect* measurements into the non-irradiated electrode (normalized to I_{prim}) may be interpreted as follows:

- If $\frac{I_{\text{indir}}}{I_{\text{prim}}} > 0$, a positive net flux of negative charge carriers from the irradiated electrode is detected in the non-irradiated electrode- either by *internal* or by *external* transport processes. In this case, equations 6.2 combined with 6.3 yields in $I_{\text{int}}^e + I_{\text{abs}} > I_{\text{int}}^h$.
- If $\frac{I_{\text{indir}}}{I_{\text{prim}}} = 0$, both contributions to the internal current, namely I_{int}^e and I_{int}^h cancel each other. Then equations 6.2 combined with 6.3 can be written as $I_{\text{int}}^e + I_{\text{abs}} = I_{\text{int}}^h$. This is only understandable by means of a two-band tunneling process involving excited electrons above the Fermi-level as well as a similar distribution of excited holes below the Fermi-level, which is a valid solution for the two-band tunneling process described in section 5.3. A more detailed description can be found in section 7.6.
- $\frac{I_{\text{indir}}}{I_{\text{prim}}} < 0$ is possible in case that a net flux of holes predominates the measured current. Then equations 6.2 combined with 6.3 yields in $I_{\text{int}}^e + I_{\text{abs}} < I_{\text{int}}^h$.

The measured current I_{indir} can be used to calculate the *indirect* emission yield

$$\Gamma_{\text{indir}} = \frac{I_{\text{indir}}}{I_{\text{prim}}} \quad (6.6)$$

Γ_{indir} defined that way describes the net number of negative elementary charges entering the non-irradiated electrode per primary electron impact.

6.10.2 Contributions to measured currents obtained under influence of external collector/repeller fields in *direct* and *indirect* experiments

The possible current contributions are identical to the ones discussed in section 6.8. Due to the electron impact onto the collector/repeller electrode causing an electron emission from the external electrode towards the sample, an additional current contribution I_{te} caused by tertiary electrons emitted from the external electrode and accelerated towards the sample

may arise. This current may have contributions of low energy electrons (i.e. secondary electrons caused by the impact of energetic electrons onto the external electrode) and of higher energy electrons (caused by electrons elastically reflected (=backscattered) on the irradiated sample, which impinge on the collector/repeller electrode and may there be again elastically reflected towards the sample). Due to the external electric field, the absorption current I_{abs} is also affected and can in part be caused by i) **cross-absorbed** secondary electrons leaving the irradiated electrode which are somehow guided back to the sample and enter the non-irradiated electrode and ii) by tertiary electrons leaving the collector/repeller electrode's surface and ending up in the non-irradiated electrode.

As defined above, the current measured on the external electrode is called I_d .

In this section, all currents which can be measured in the respective experiment are discussed and their contribution to the re-absorption and cross-absorption currents are presented.

The measured sample current in case of *direct* experiments consists of these contributions:

$$I_{\text{dir}} = I_{\text{prim}} - I_{\text{int}} - I_{\text{se}} - I_{\text{bse}} + I_{\text{te}} + I_{\text{reabs}} \quad (6.7)$$

Obviously, this is just the current like discussed in equation 6.1 with the additional contribution I_{te} arising from the external electrode.

The sample current measured in **indirect** experiments is identical to the definition in equation 6.2 with the same internal current like defined in 6.3. As above, the sample current can be used to define the *internal* emission yield as defined in equation 6.6.

The assumption, on which the equations 6.7 and 6.2 base on, is, that all tertiary electrons emitted from the collector/repeller electrode contribute to the current measured into the irradiated electrode. Since electrons backscattered on the sample may in principle hit the collector/repeller electrode anywhere and may therefore cause the emission of tertiary electrons anywhere on the collector/repeller electrode. These tertiary electrons may therefore be accelerated towards the sample and may thereby either impinge on the irradiated electrode, on the non-irradiated electrode and even on the glass substrate. The partition between these different possibilities depends on the position from which the tertiary electrons start, on the electric field configuration between collector/repeller and sample and on the charge of the sample (in case a bias voltage is applied) [14]. The current measured onto the collector/repeller electrode consists of the following contributions:

$$I_d = I_{\text{se}} + I_{\text{bse}} - I_{\text{te}} \quad (6.8)$$

If a voltage U_d is applied between the collector/repeller electrode and the sample, the measured currents are changed as follows:

For $U_d \geq 0$ (collector mode), externally emitted electrons are drained towards the collector/repeller and the emission of low-energy tertiary electrons from the collector/repeller

towards the sample becomes suppressed. For sufficiently large values of U_d , this leads to a complete extraction of all emitted electrons, corresponding to

$$I_{\text{reabs}} = 0, I_{\text{abs}} = 0 \text{ and } I_{\text{te}} = 0 \quad (6.9)$$

Under these conditions, the **direct** current (equation 6.7) simplifies to

$$I_{\text{dir}}^+ = I_{\text{prim}} - I_{\text{int}} - I_{\text{se}} - I_{\text{bse}} \quad (6.10)$$

and the **indirect** current (equation 6.2) reduces to

$$I_{\text{indir}}^+ = I_{\text{int}} \quad (6.11)$$

Normalizing these currents to the primary electron current yields

$$\frac{I_{\text{dir}}^+}{I_{\text{prim}}} = 1 - \Gamma_{\text{int}} - \delta + \eta = 1 - \Gamma_{\text{int}} - \zeta \quad (6.12)$$

$$(6.12) \& (6.6) \Rightarrow \boxed{1 - \frac{I_{\text{dir}}^+}{I_{\text{prim}}} - \frac{I_{\text{indir}}^+}{I_{\text{prim}}} = \zeta} \quad (6.13)$$

The current measured into the collector/repeller electrode is given by the equation

$$(6.8) \Rightarrow \boxed{I_d^+ = I_{\text{se}} + I_{\text{bse}} = \zeta \cdot I_{\text{prim}}} \quad (6.14)$$

since the emission of tertiary electrons is inhibited due to the collector/repeller field.

For $U_d < 0$ (repeller mode), externally emitted electrons are reflected towards the sample and contribute to the re- and cross-absorption currents. For sufficiently negative values of U_d , all emitted secondary electrons are held back at the sample surface, yielding

$$I_{\text{se}} = I_{\text{reabs}} + I_{\text{abs}} \quad (6.15)$$

At the same time, all tertiary electrons emitted from the collector/repeller electrode are now accelerated towards the sample. The **direct** current measured under these conditions is

$$I_{\text{dir}}^- = I_{\text{prim}} - I_{\text{int}} - I_{\text{se}} - I_{\text{bse}} + I_{\text{te}} + I_{\text{reabs}} \quad (6.16)$$

and the **indirect** current (equation 6.2) by

$$I_{\text{indir}}^- = I_{\text{int}} + I_{\text{abs}} \quad (6.17)$$

Summing equations (6.16), (6.17) and (6.15) results in

$$\Rightarrow I_{\text{dir}}^- + I_{\text{indir}}^- = I_{\text{prim}} - I_{\text{bse}} + I_{\text{te}} \quad (6.18)$$

$$\Rightarrow \boxed{1 - \frac{I_{\text{dir}}^-}{I_{\text{prim}}} - \frac{I_{\text{indir}}^-}{I_{\text{prim}}} = \eta \cdot (1 - \delta_{\text{collector/repeller}})} \quad (6.19)$$

Note that the partition of I_{te} between I_{dir} and I_{indir} is irrelevant in eq. (6.19), where $\delta_{\text{collector/repeller}}$ denotes the low energy electron emission coefficient at the collector/repeller electrode surface. The current measured at the collector/repeller electrode is given by the equation

$$(6.8) \Rightarrow I_{\text{d}}^- = I_{\text{bse}} - I_{\text{te}} \quad (6.20)$$

since the secondary electrons emitted from the sample are reflected and therefore do not reach the collector/repeller.

The (cross-) absorption current can be determined by subtracting equation 6.11 from equation 6.17:

$$I_{\text{abs}} = I_{\text{indir}}^- - I_{\text{indir}}^+ \quad (6.21)$$

7 Experimental results without external field

Within this chapter, the results of experiments performed using MIM devices under electron irradiation will be shown and discussed. At first, experiments with a constant kinetic energy will be shown, where the electron beam is steered across the sample to identify different areas of the MIM device. The second part deals with the kinetic impact energy dependence of detected device currents while scanning along the top silver electrode of the MIM in the *probe top* as well as in the *probe bottom* mode. The third part deals with the kinetic impact energy dependence of detected device currents while scanning across the silver and thereby along the bottom aluminum film. It will be discussed, that the nature of the experiments changes during such scans. From parts two and three, *indirect* and *direct* emission yields as function of the primary kinetic impact energy can be derived and compared to results as reported in the literature, which can be found in the fourth part. In the fifth part, the dependence of the *indirect* and *direct* emission yields on the impact angle is shown and discussed. Finally the dependence of the measured *indirect* and *direct* emission yields on the internal bias voltage between the two metal electrodes of the MIM device will be shown and discussed. In principle, all the topics discussed here including the corresponding figures can be found in [13].

7.1 Scanning the electron-beam

The impact point of the electron beam onto the surface of the MIM has significant influence to the experiments; therefore it is necessary to clearly identify this impact point. Scanning the electron beam across the surface while measuring the resulting sample currents allows for a clear identification of the impact point. Since the diameter of the primary electron beam is $\varnothing < 1$ mm and therefore smaller than the relevant dimensions of the MIM device, the different areas of the samples can be individually examined. As discussed in the section 6.7, the primary electron current I_{prim} was measured in the Faraday cup along with beam diameter. With the noted position of the Faraday cup relative to the sample position, it was possible to steer the sample via the *x-y-z*-manipulator in the center of the electron beam. Depending on the desired experimental mode, *probe top* and *probe bottom*, respectively, either the current in the top silver or bottom aluminum electrode was measured as function of the momentary primary electron beam's impact point. By changing the *x*- and *z*-coordinate (with the coordinate system as defined above), it was

possible to identify the so called "active area" of the MIM, which is the area where all three MIM layers overlap.

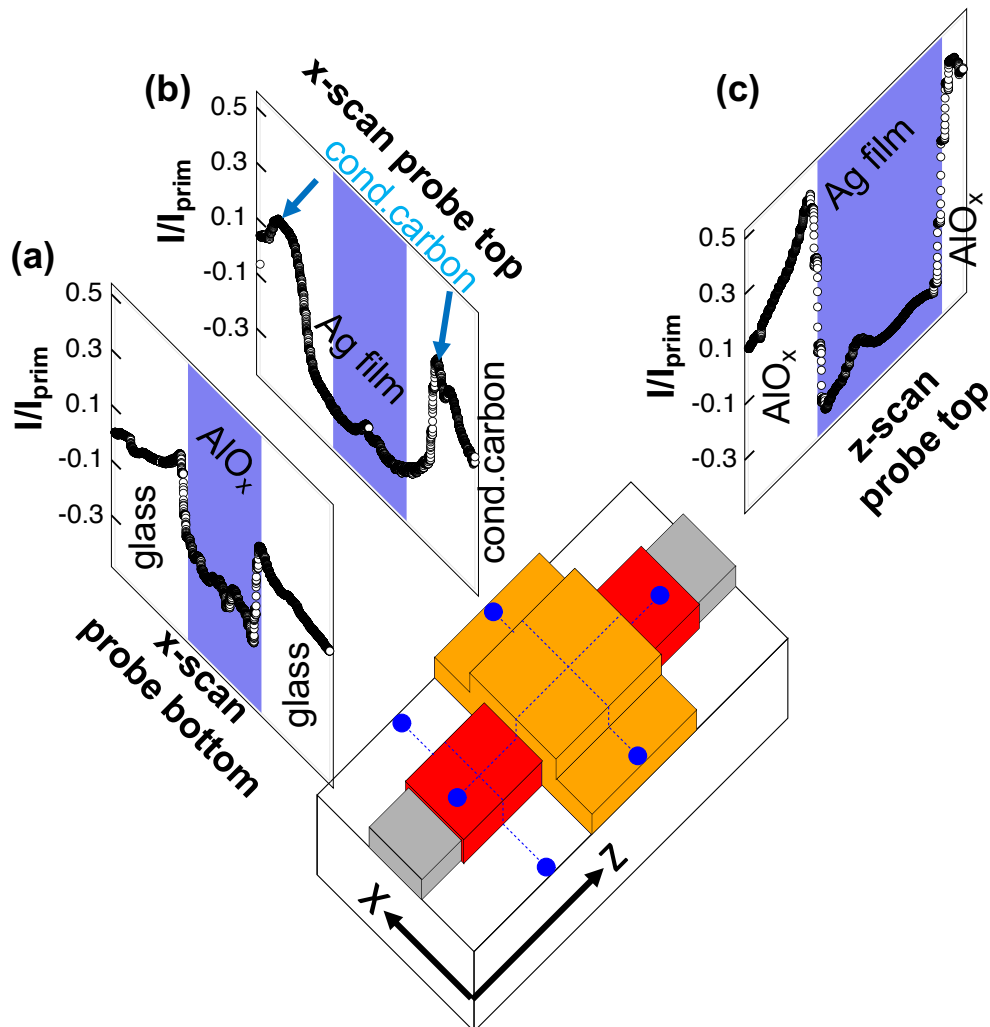


Figure 7.1: Visualization of position dependent experiments: The image shows a schematic of a MIM and the results (normalized currents) of three different scans performed for a primary kinetic energy of 500 eV: **(a)** *x*-scan outside the active area for a path across the glass substrate towards the oxide covered aluminum towards the glass again while measuring the current into the aluminum bottom electrode (*probe bottom* mode). **(b)** *x*-scan across the active area starting on a contact pad of conductive carbon (used for wiring the MIM) along the silver film outside the active area, crossing the active area, along the silver film outside the active area towards the second contact pad of carbon while measuring the current into the silver top electrode. **(c)** *z*-scan along the aluminum film starting on the oxide covered aluminum film, crossing the silver film within the active area and ending again on the oxide covered aluminum while measuring the current into the top silver electrode.

Each impact point was irradiated for several seconds (typically 5..10 s to ensure, that

the detected currents remained unchanged. After each set of experiments, the primary electron current I_{prim} was measured again in the FC; in case of a discrepancy between the current before and after the experiment, the result of this particular experiment was discarded and the measurement repeated.

In the following plots, the ordinate shows the measured current I normalized to the primary electron current I_{prim} as function of the corresponding impact point (on the abscissa).

7.1.1 x -scans Finding the active area of the sample

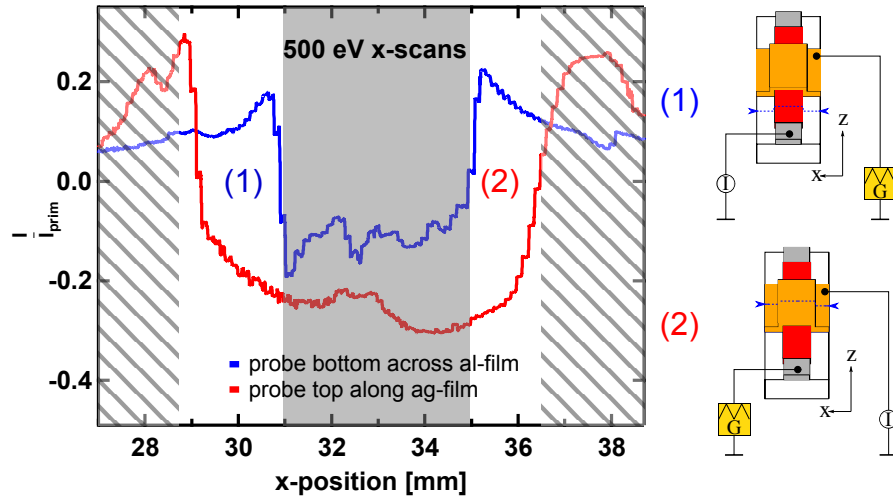


Figure 7.2: x -scans to determine the position of the active area (1) in *probe bottom* mode with electron beam being scanned like depicted by the dashed blue line in pictogram (1): path from glass/ AlO_x on Al/glass (2) in *probe top* mode with electron beam being scanned as depicted by the dashed blue line in pictogram (2): path from silver on glass/ active area / silver on glass with 500 eV kinetic impact energy. The grey box indicates the position of the aluminum film, which is also the underlay of the active area. Taken from [13].

To identify the position of the active area (the part of the MIM, where all three layers overlap and form a sandwich like structure), at first the x -position of the aluminum film was determined, since the aluminum film is the underlay of the active area. Therefore, a x -scan has been performed at a z -position, where the primary electron beam followed a path across the glass substrate, crossing the (oxide covered) aluminum film and across the glass substrate again, while measuring the current into the aluminum electrode. The result is depicted as graph (1) in the figure 7.2. The beam path is symbolized by the blue dashed line in pictogram (1) of the figure. The normalized current detected in the aluminum electrode starts with values of around 0.1 when the glass substrate is irradiated. This is interpreted as a current of electrons from the glass substrate towards the aluminum electrode, since by convention (see above), an incoming flux of negative charge carriers is counted as positive current. This behaviour is understandable in terms of an emission of secondary electrons from the glass, while some of these secondary electrons impinge on

the aluminum. When the oxide covered aluminum is irradiated instead of the glass (for $31 \text{ mm} < x < 35 \text{ mm}$), the normalized current is negative, which indicates, that more negative charge carriers (i.e. electrons) leave the aluminum, than impinge onto it. For $x > 35 \text{ mm}$, the glass substrate is irradiated again, which is visible by a strong change of the signal at the transition point. The measured current curve runs almost symmetrical in comparison with the other side of the glass substrate. Therefore the x -coordinates of the aluminum film are derived to $31 \text{ mm} \leq x \leq 35 \text{ mm}$. The red curve (2) in the same figure shows the result of an x -scan along the MIM's silver film at a different z -coordinate, while measuring the current into the silver film. The path of the electron beam is depicted as blue dashed line in pictogram (2) of the figure. After an increase from values around 0.1 to values around 0.3, the measured current signal drops fast at $x \approx 29 \text{ mm}$ to values of $\frac{I}{I_{\text{prim}}} \approx -0.2$. With exception at $x \approx 33 \text{ mm}$, the signal forms a plateau, until it increases to positive values again starting at $x = 36 \text{ mm}$. The plateau-width of about 7 mm is understandable in terms of a constant secondary electron emission from the silver into the vacuum, which is in line with the negative normalized current, indicating an external electron emission yield of 1.2. The current change at $x < 29 \text{ mm}$ and at $x > 37 \text{ mm}$ is assigned to the irradiation of carbon contacts instead of the silver. Therefore the areas are shaded here and will not be shown in the following plots, since there the carbon contact points instead of the sample are irradiated and the surface structure is undefined at these points. The feature at $x = 33 \text{ mm}$ is assigned to a local carbon contamination.

In both cases, the experiments depicted in figure 7.2 are *direct* experiments, since the irradiated electrode is also the current metered electrode. This chapter may in similar form also be found in [13].

7.1.2 x-scans for different kinetic impact energies

To determine the energy dependence of the electron beam induced *external* secondary electron emission yield, x -scans for different kinetic impact energies were performed. The results of the scans performed along the center of the silver electrode as indicated in the pictogram in *probe top* mode are shown in panel (a) of figure 7.3, the results in the *probe bottom* in panel (b). The results of the scans in *probe top* mode show a significant energy dependence along with broad plateaus of about 7 mm plateau width that correlate to the geometric width of the silver film. The active area, indicated by the grey box, does not seem to play a special role in the measurements shown in panel (a). Starting with values $\frac{I}{I_{\text{prim}}} \approx 1$ for 75 eV indicating zero *external* electron emission, for 150 eV values of 0.3 are reached, indicating a *direct* emission yield of 0.7. For 200 eV the *direct* emission yield is equal to 1, since the normalized current reaches values $\frac{I}{I_{\text{prim}}} \approx 0$ and reaches values of $\frac{I}{I_{\text{prim}}} \approx 1.3$ for 1 keV. All curves in (a) except the one for 75 eV show a clear signal change at $x \approx 29 \text{ mm}$ and at $x \approx 37 \text{ mm}$, where the carbon contact points are left towards the silver film as discussed above. A feature around $x \approx 33 \text{ mm}$ is also visible in all curves except for 75 eV, again assigned to a local carbon contamination.

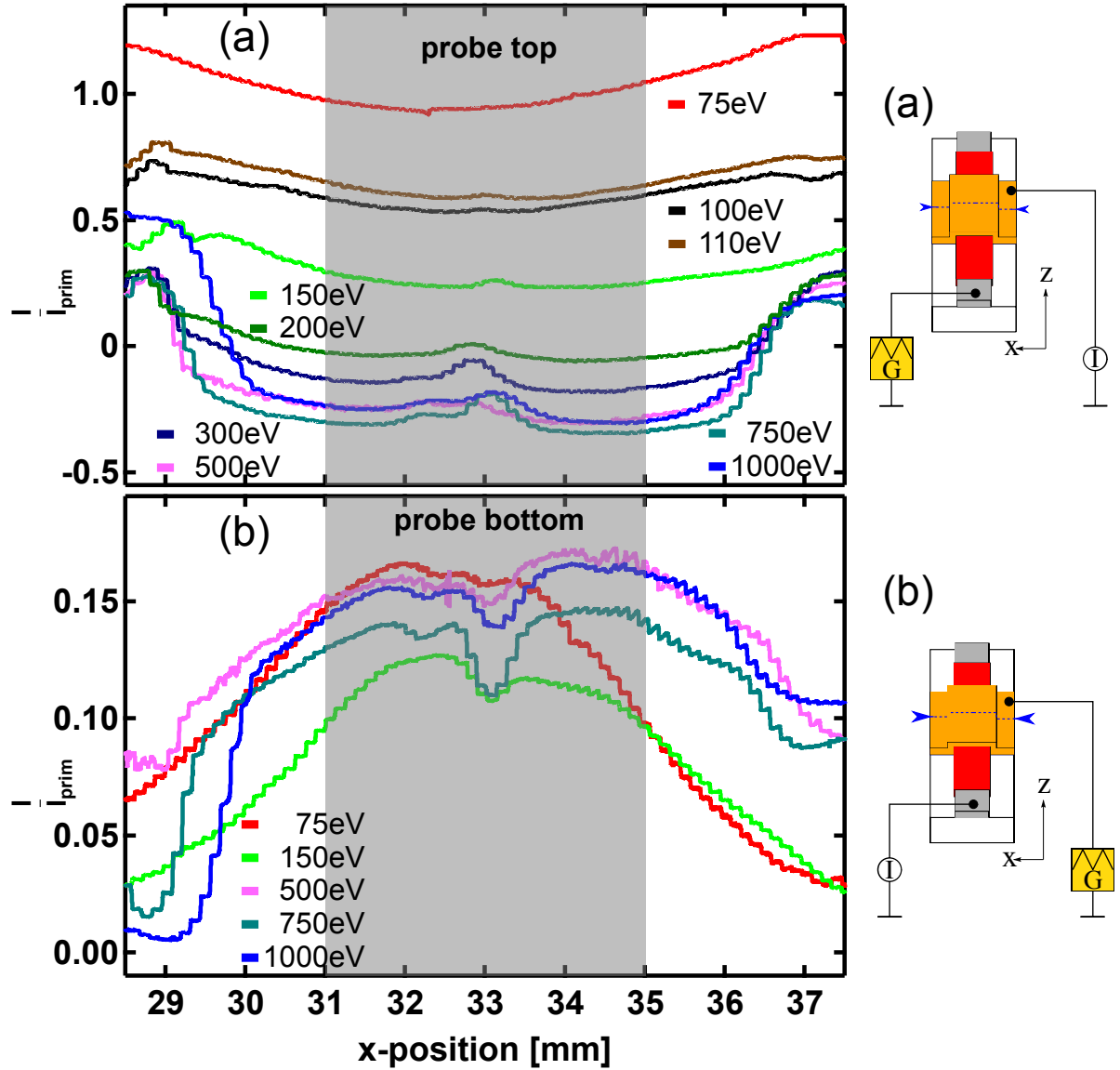


Figure 7.3: (a): Results of x -scans in *probe top* mode (see pictogram (a)) for different kinetic impact energies in the range of 75..1000 eV. The z -coordinate (as well as the y -coordinate) were identical for all scans. (b): same as (a) in *probe bottom* mode (see pictogram (b)). The grey box indicates the position of the active area, which is defined by the width of the underlying aluminum film. See also [13].

The measurement at 75 eV is included for comparison only, since the normalized current values $\frac{I}{I_{\text{prim}}} > 1$ point to a mis-measured primary current I_{prim} , which was indeed tedious to determine at low kinetic energies. Therefore the overall form of the measured current curve is credible, but the position is somehow questionable. The results of scans in the *probe bottom* mode are shown in panel (b) of the figure 7.3, indicating a significantly less pronounced impact energy dependence of the signals. The normalized current remains at

values around $\frac{I}{I_{\text{prim}}} \approx 0.12..0.15$, if the active area is irradiated. All curves show an signal increase for $29 \text{ mm} < x < 31 \text{ mm}$ and a decrease for $35 \text{ mm} > x > 37 \text{ mm}$. The signals measured at x -values corresponding to the active area are more or less constant and show a feature at $x \approx 33 \text{ mm}$, which is again assigned to a carbon contamination of the surface. Since all x -scans shown here were performed at the same z -position and also all z -scans (see chapter 7.1.3) at the same x -position, the built-up of such a localized contamination seems to be reasonable. The fact that a significant current signal is measured also in case the silver film *outside* the active area is irradiated in *probe bottom* mode, points towards a non-negligible *external* transport channel for excitation. A more detailed discussion can be found in section 7.8.

7.1.3 z -scans for different kinetic impact energies

Scans in z -direction allow to compare results for the impact on oxide covered aluminum and for the active area. Therefore, z -scans at a fixed x -coordinate of $x = 33 \text{ mm}$ for different kinetic impact energies were performed. During z -scans in *probe top* mode, as depicted in panel (a) of figure 7.4, the nature of the experiment changes from an *indirect* experiment, when the oxide covered aluminum is irradiated, to a *direct* experiment, when the active area is irradiated and back to an *indirect* experiment, when the electron beam leaves the active area towards the oxide covered aluminum again. In case of *probe bottom* experiments, the irradiation of the oxide covered aluminum corresponds to a *direct* experiment, while the irradiation of the active area corresponds to an *indirect* experiment. The grey box in figure 7.4 indicates the position of the active area; the blue lines in the pictograms indicate the path of the scans. The z -scans in *probe top* mode (panel (a) of figure 7.4) show a signal increase from $140 \text{ mm} \leq z \leq 142 \text{ mm}$ and a decrease from $146.5 \text{ mm} \leq z \leq 147 \text{ mm}$. In these z -intervals, the dependence of the measured (normalized) currents on the kinetic impact energy is weak and the position dependence is strong. For all energies, the normalized currents are positive within these z -intervals. Due to the convention, that electron currents floating into the measuring electrode are counted as positive, this means that electrons are emitted from the aluminum and are somehow detected in the top silver electrode. The signal increase with approaching to the active area points to an external electron emission/cross-absorption process working with the higher efficiency, the closer the impact point is to the active area. The feasibility of such a transport of excitation from the aluminum electrode towards the silver top electrode while crossing the oxide barrier seems questionable; a further discussion is found in chapter 7.8.

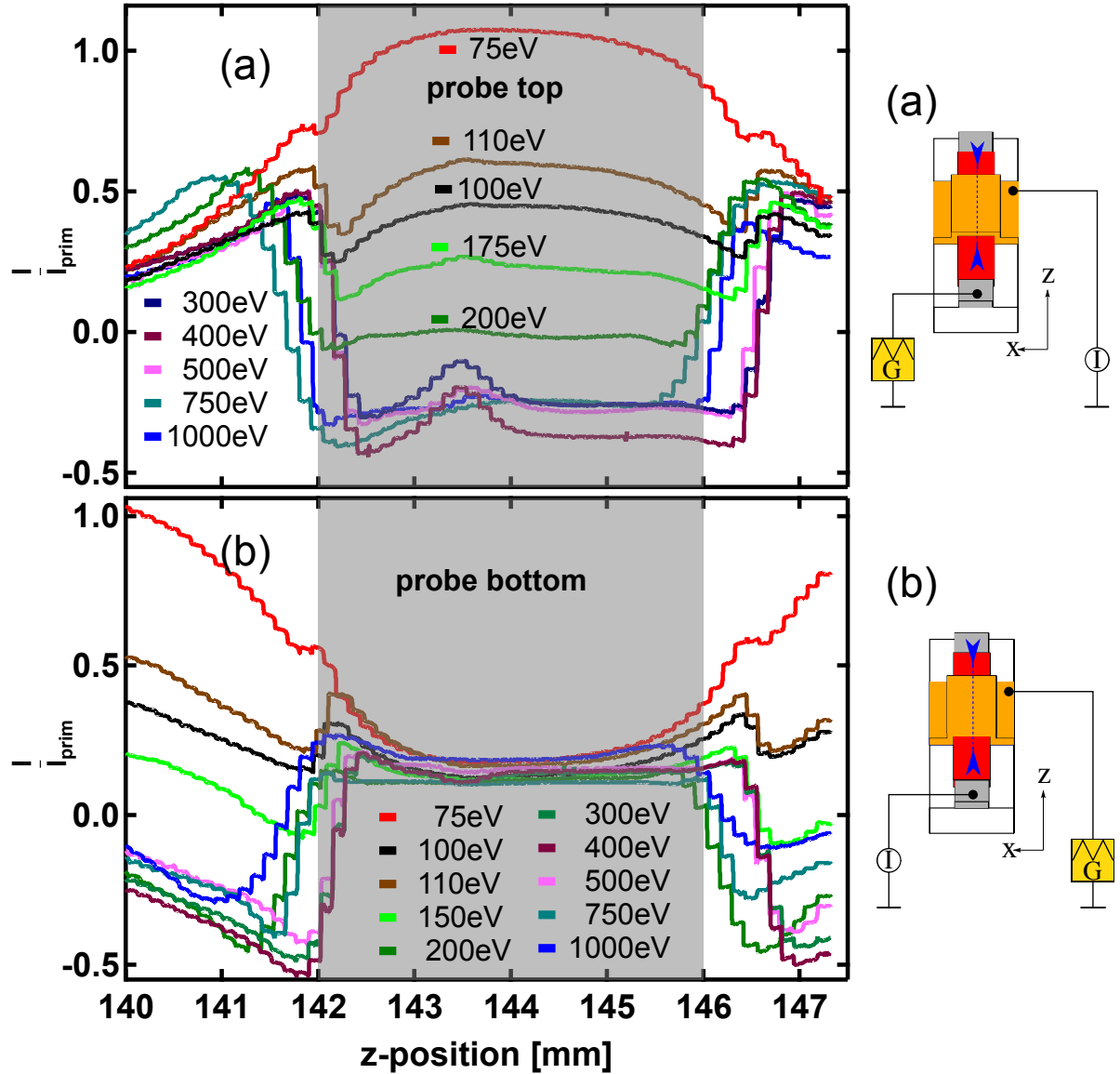


Figure 7.4: (a): Results of z -scans in *probe top* mode (see pictogram (a)) for different kinetic impact energies in the range from 75..1000 eV. The x -coordinate (as well as the y -coordinate) were identical for all scans. (b): same as (a) in *probe bottom* mode (see pictogram (b)). The grey box indicates the position of the active area. For $142 \text{ mm} \leq z \leq 146 \text{ mm}$, the active area is irradiated (shown as grey shaded area), while otherwise the e^- -beam impinges on the AlO_x /aluminum film. See also [13].

In case of *direct* experiments in *probe top* mode (for z -values in the interval from $142 \text{ mm} \leq z \leq 146 \text{ mm}$), the measured current curves show a strong dependence on the primary impact energy and plateaus with a width corresponding to the 4 mm geometrical width of the active area can be seen. For 75 eV, normalized currents of $\frac{I}{I_{\text{prim}}} \approx 1$ are measured indicating a negligible direct electron emission yield. For 200 eV the normalized currents

are close to zero and the direct electron emission yield is $\Gamma_{\text{dir}} \approx 1$ and further increases towards negative values. For $E_{\text{prim}} \geq 300\text{eV}$, the dependence on the primary impact energy is weak and normalized current values of $\frac{I}{I_{\text{prim}}} \approx -0.3..-0.4$ are measured that correspond to external electron emission yield of $\Gamma_{\text{dir}} = 1.3..1.4$. In case of *direct* experiments in *probe bottom* mode (panel (b) of 7.4 for irradiation of the oxide covered aluminum film), a similar energy dependence as observed in the *probe top* mode and irradiation of the active area, in combination with a signal decrease with approaching to the active area, is observed. For kinetic impact energies $E_{\text{prim}} \geq 150\text{ eV}$, the energy dependence is negligible and the measured (normalized) current just depends on the position. For these energies, the measured normalized currents are $\frac{I}{I_{\text{prim}}} < 0$ corresponding to a direct electron emission yield $\Gamma_{\text{dir}} > 1$. If the active area is irradiated ($142\text{ mm} \leq z \leq 146\text{ mm}$), the measured curves show clear plateaus of the width corresponding to the geometrical width of the active area. For all impact energies, the normalized currents reach values of $\frac{I}{I_{\text{prim}}} \approx 0.2$, similar to the values observed in panel (b) of 7.3.

7.1.4 Evaluation of the x- and z-scans

In panel (a) of figure 7.5, the *direct* electron emission yield calculated by equation 6.5 on page 45 is shown as function of the primary impact energy. Γ_{dir} describes the external electron emission into the vacuum and is obtained by evaluating the plateau values from *x*- and *z*-scans for irradiation of the active area outside the carbon contaminated area in *probe top* mode as shown in panels (a) of figures 7.3 and 7.4, respectively. In panel (b) of figure 7.5, the *indirect* emission yield calculated by 6.6 is shown as function of the primary impact energy, which describes the apparently *internal* emission yield Γ_{indir} obtained from evaluating the plateau values of *x*- and *z*-scans for irradiation of the active area outside the carbon contaminated area in *probe bottom* mode as shown in panels (b) of figures 7.3 and 7.4, respectively. The blue curves in 7.5 correspond to results from *x*-scans, the black curves to results from *z*-scans and the red curves to averaged values.

As visible in panel (a) of figure 7.5, Γ_{dir} shows a clear increase with increasing impact energy from values of $\Gamma_{\text{dir}} = 0$ at 75 eV to values of $\Gamma_{\text{dir}} \approx 1$ at 200 eV and is practically independent of the primary impact energy for energies above 300 eV with values of $\Gamma_{\text{mathrmdir}} \approx 1.3$. Positive values of $\Gamma_{\text{dir}} = 1.3$ correspond to the emission of 1.3 electrons per impinging primary electron.

The *indirect* emission yield Γ_{indir} obtained from *indirect* experiments as depicted in panel (b) of figure 7.5 shows no significant dependence on the primary impact energy. For all energies, values of $\Gamma_{\text{indir}} \approx 0.14$ are detected.

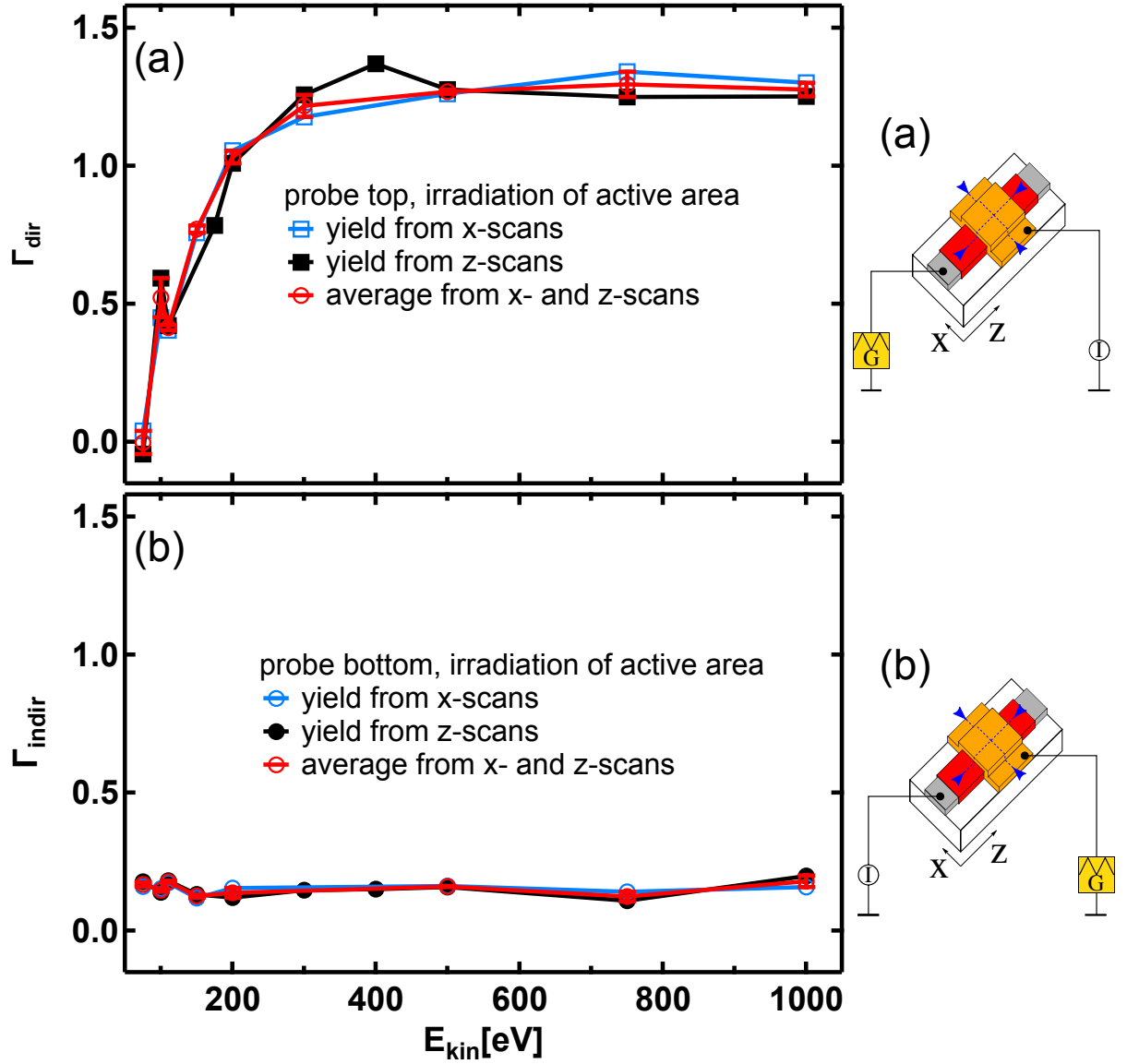


Figure 7.5: Evaluation of the x - and z -scans as function of the primary impact energy. (a): Direct emission yield in *probe top* mode evaluated by reading out plateau values from parts (a) of figure 7.3 and of figure 7.4, respectively, along with averaged result (red curve). (b): Indirect emission yield in *probe bottom* mode evaluated by reading out plateau values from parts (b) of figure 7.3 and of figure 7.4, respectively, along with averaged result (red curve). See also [13].

7.2 Simulations of δ and η

Only few results obtained for δ and η for similar kinetic impact energies are reported in the literature, which were all measured on bulk-samples. To increase the footing for data com-

parison purposes, simulations with the available software packages have been performed. The most versatile tool was the Casino Monte-Carlo package, which is intended to simulate the behaviour of 3d structures in a SEM. In its latest version (3.3) [20], the NIST's MONSEL code [58, 59] was implemented, permitting the simulation of secondary electron generation. The other available program packages, e.g. Casio 2.42 and pyPENELOPE [21, 19], do not include this feature and are therefore useful for calculations of backscattering coefficients only. In this context it should be noted, that the simulations for primary kinetic energies below 1 keV are not well tested within any of the three program packages due to limitations in the used models. However, the proper trend can be obtained, anyway and for kinetic energies above 1 keV the computed results are in good agreement to the experimental findings.

The results of secondary electron yields δ as function of the kinetic impact energy computed using the Casino package as well as experimental results from the literature are shown in panel (a) of figure 7.6.

A sample in the Casino code is defined by the physical dimensions of the individual layers and by choosing the individual composition for each layer, which can either be atomic or molecular. By defining the mass density in $\frac{\text{g}}{\text{cm}^3}$, the atomic number Z and in case of compositions, the atomic numbers along with either the weight-fraction or the atomic fraction of the respective elements along with the plasmon energy and the work-function (both measured in eV), the sample is completely defined. Therefore, crystalline structures are not considered within the simulations.

According to [20, 58], electron trajectories are calculated using a hybrid-model treating the plasmon-scattering and electron-electron as individual events, while other inelastic processes are approximated by assuming a mean energy loss, when the MONSEL standard settings are used. As Lowney points out in [58], the residual energy loss rate $(dE/dS)_r$ is a value added to the value of the work-function. This modifies the lower energy limit, electrons have to overcome to be emitted into the vacuum and has strong influence on the secondary electron yield [58].

Using the standard settings of the MONSEL code (50 eV limit), the calculated values for δ reach values of ≈ 3 for low impact energies, which is about twice of the experimentally determined values. At higher impact energies, the experimentally observed behaviour is quite well reproduced by the simulations. The relevant parameter to improve the correlation between experimental data and calculations is the lower cut off energy¹. From a physical view, this parameter just shifts the number of electrons counted as secondary electrons ($E_{\text{kin}} < 50$ eV) and electrons counted as backscattered electrons ($E_{\text{kin}} > 50$ eV). The best agreement between experimental data and calculated results was achieved using the values for η and a lower limit of 5 eV, which is shown as magenta colored curve in panel (a). Again, it must be noted that this is just an artificial, heuristic tuning towards better agreement and does not make sense from a physical view. However, as discussed in [16], the discrimination between secondary electrons and backscattered electrons in the energy regime below 1 keV is arbitrary. In panel (b) of figure 7.6, the results of backscattering

¹in the code called "Minimum electron energy [No Sec. generation]"

coefficients η calculated using Casino as well as pyPENELOPE along with experimental results are shown.

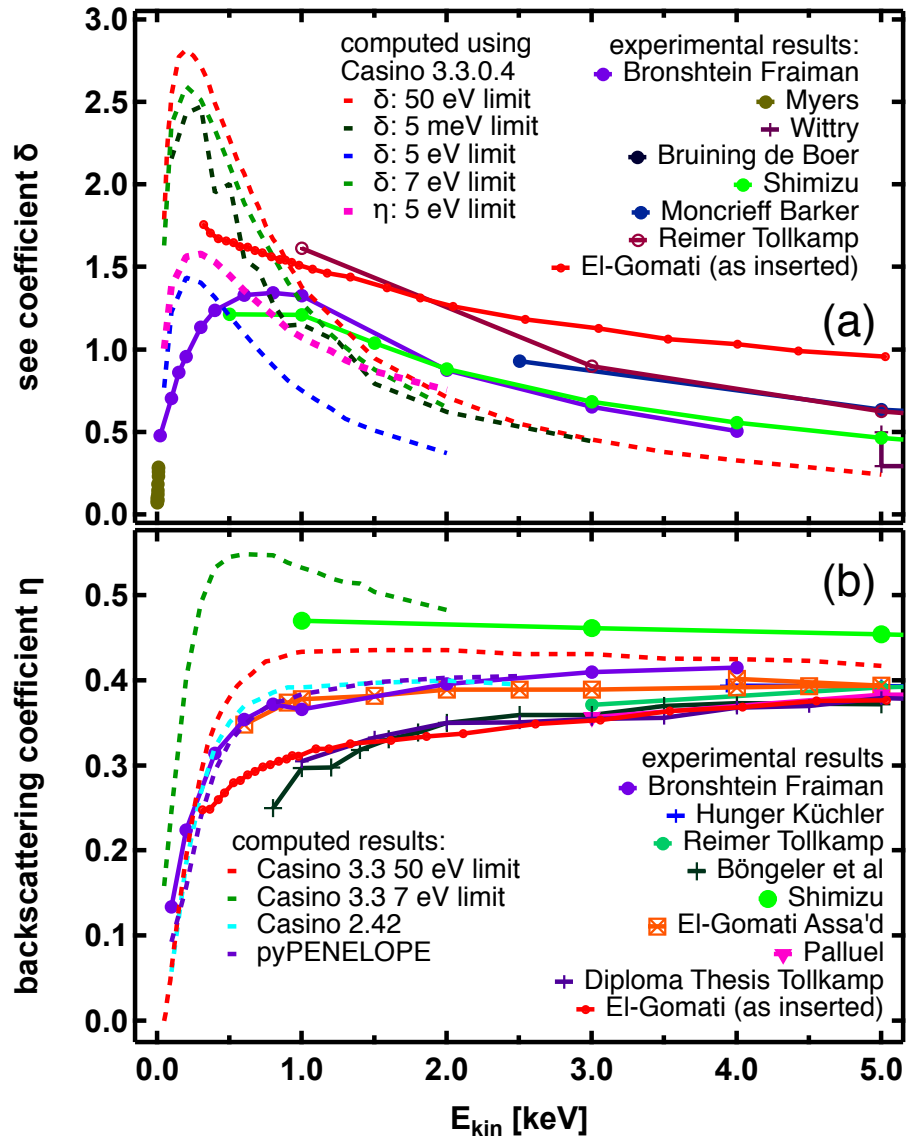


Figure 7.6: (a): Results of simulations computed using Casino for δ in comparison to available literature data as function of the kinetic impact energy for irradiation of silver. (b): Results of simulations computed using Casino and pyPENELOPE for η in comparison to available literature data as function of the kinetic impact energy also for irradiation of silver. Bronshtein Fraiman [60], Myers [61], Wittry [62], Bruining de Boer [63], Shimizu [29], Moncrieff Barker [64], Reimer Tollkamp [65], Hunger Kuchler [66], Böngeler [67], El-Gomati Assa'd [68], Palluel [69], Diploma Thesis Tollkamp [70], Casino [20, 21], pyPENELOPE [19], El-Gomati [71, 72]

The overall agreement using the standard settings between calculated and experimental results is good, with exception of the simulation using Casino 3.3 and 7 eV lower energy

limit, which shows a signal increase at low kinetic energies. This behaviour is the clearer, the lower this energy limit was set, leading to the curve for η at 5 eV limit shown in panel (a) of the figure. This is in line with the discussion above, that the chosen energy just changes the assignment into secondary and backscattered electrons, which is also proven by the fact, that the sum ζ of η and δ for 5 eV and for 50 eV are identical (as shown in panel (a) of 7.10).

To revise a possible influence of the layer structure to the results obtained from the simulations, calculations were performed using different target systems. In panel (a) of figure 7.7, results of simulations of the backscattering coefficient η for silver bulk samples obtained with Casino 3.3 [20], Casino 2.42 [21] and with pePENELOPE [19] along with simulations for a irradiation of a MIM multi-layer system (provided by H. Demers) using Casino 3.3 are shown as function of the primary impact energy. The results obtained with Casino 2.42 and with pePENELOPE are almost identical, so are the results obtained by using Casino 3.3. In panel (b) of the figure, results of simulations of the secondary electron emission coefficient δ obtained by using Casino 3.3 for irradiation of a silver bulk samples and of a MIM multi-layer system (provided by H. Demers) are shown. Again no different is observed between both results. This non-existing difference between the results obtained for a 40nm silver bulk sample and the MIM (both with Casino 3.3) become plausible, when the figure 7.9 (see below) is taken into account, since obviously only the upper ≈ 10 nm of the silver film are influenced by the irradiation and therefore the layer structure below the top layer does not affect the signal. This may be different, when tunneling between the layers would be taken into account, but that is beyond the scope of the discussed software packages. In panel (a) of figure 7.8, the results for the backscattering coefficient η calculated with the Casino versions 2.4.2 and 3.3 are shown. η increases with increasing impact angle if calculated with Casino 2.4.2, which is also the predicted and experimentally observed behaviour, since the excitation caused by the primary electrons is located nearer to the surface. The calculations with Casino 3.3 show a **decrease** instead. This is a consequence of the way the surfaces of the solids are defined in the different versions of Casino. In Version 2.4.2, the surface of the sample is defined by a fixed plane and the impact angle is changed by tilting the impinging electron beam; every trajectory above the surface plane is interpreted as backscattered electron, if the energy is higher than 50 eV. The calculation of secondary electrons is not implemented. In version 3.3 of Casino, the primary electron beam has a fixed position and the sample is tilted instead; the generation of secondaries is implemented (see panel (b) of the figure), but the result as function of the impact angle also seems faulty. In this version, every trajectory above the surface plane is interpreted as backscattered electron if the energy is higher than 50 eV and as secondary electron if the energy is less than 50 eV, but due to the tilt of the sample, the surface is not well defined anymore. Therefore the calculation of angle dependent results for δ is not possible, if the trajectories are not individually examined, which was beyond the scope of this thesis.

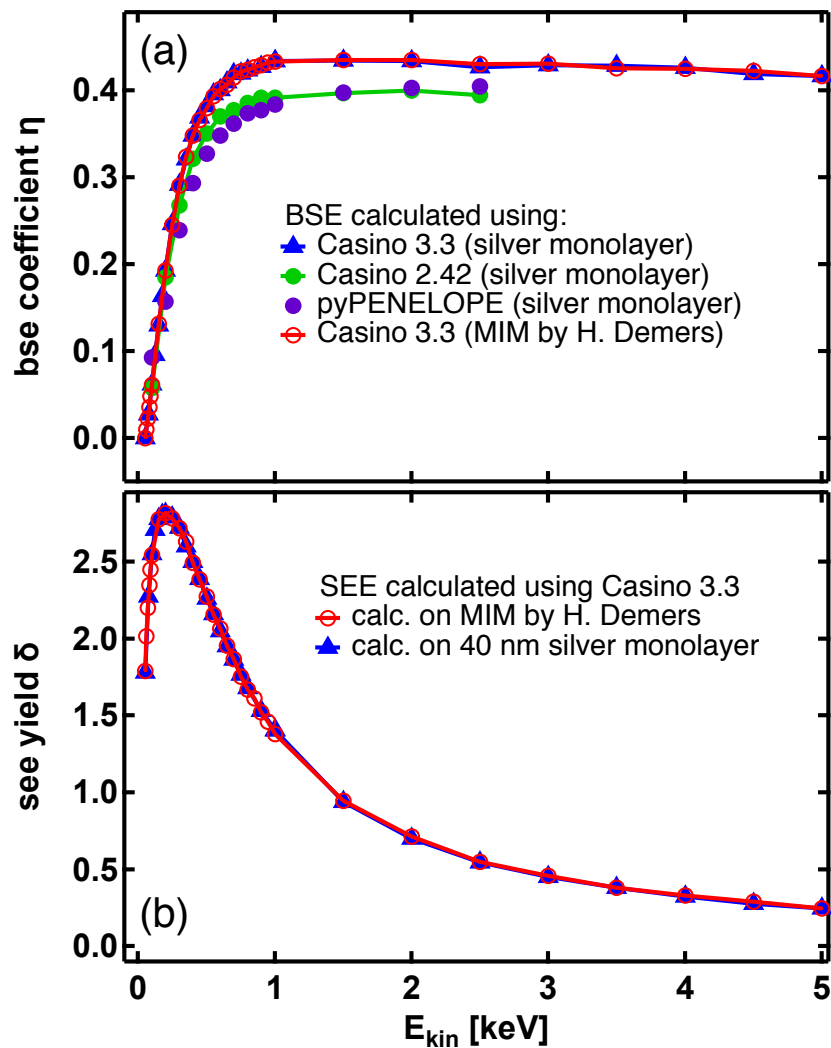


Figure 7.7: (a): Results of the simulated backscattering coefficient η as a function of the primary kinetic energy calculated using Casino 3.3, Casino 2.42 and pyPENELOPE for 40 nm- thick silver layers and using Casino 3.3 and a MIM multi-layer (provided by H. Demers). (b): Results of the simulated secondary electron emission coefficient δ as function of the primary kinetic energy calculated using Casino 3.3 for 40 nm-thick silver layer and for a MIM multi-layer (provided by H. Demers).

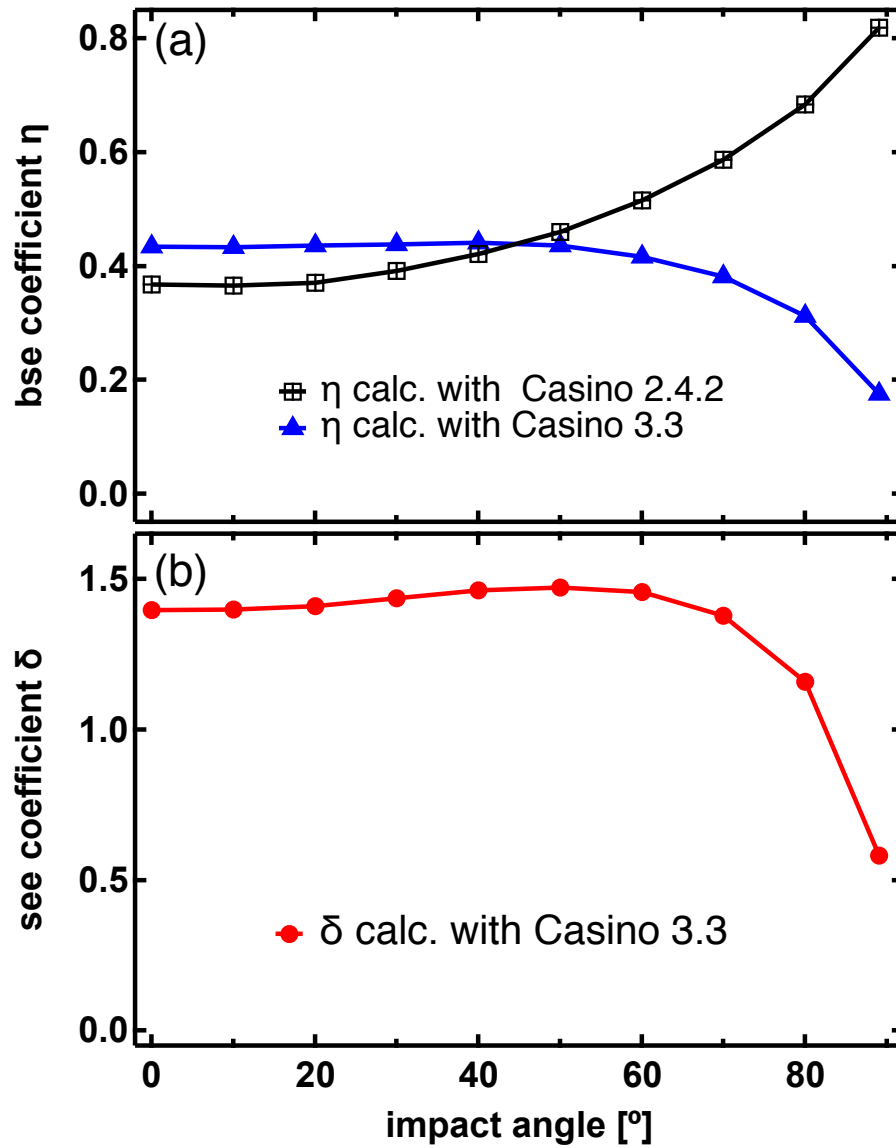


Figure 7.8: (a): Results of the simulated backscattering coefficient η as a function of the impact angle calculated using Casino 3.3 and Casino 2.4.2 for irradiation of a 40 nm thick silver film. (b): Results of the simulated secondary electron emission coefficient δ as function of the impact angle calculated using Casino 3.3 for irradiation of a 40 nm thick silver film.

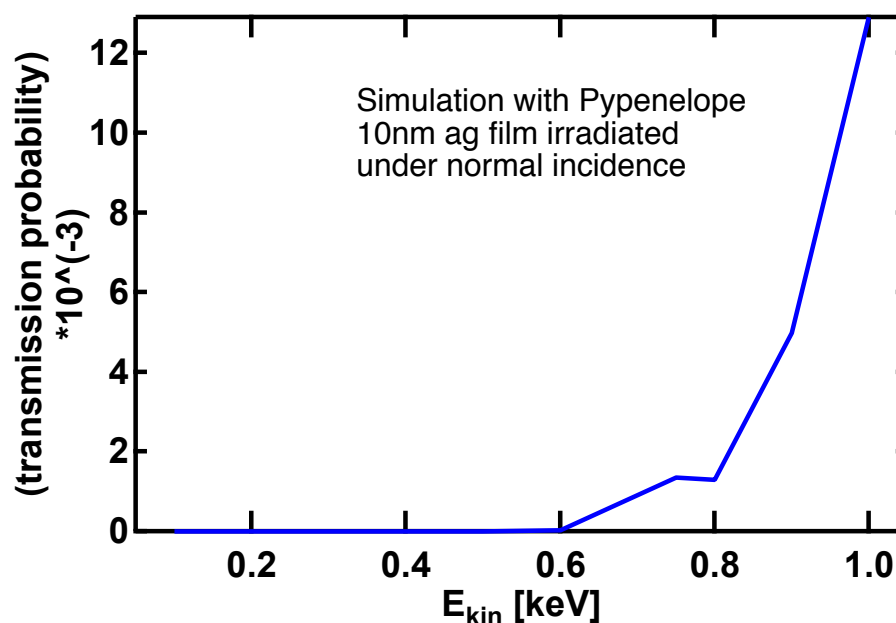


Figure 7.9: The results of simulations for the transmission through a 10 nm thick silver film calculated using pyPENELOPE are shown.

In figure 7.9 the results of the calculated transmission probability for a 10 nm thick silver film as function of the projectile energy obtained with pyPENELOPE are shown. Even if the boundary conditions may be faulty, it becomes obvious that in the energy range relevant for the experiments presented within this thesis, the transmission of projectile electrons through the top layer of the MIM, which is 50nm thick, will not occur.

In principle, simulations using Casino 3.3 provide valuable information, which are qualitatively comparable to experimental results. However, in the energy regime below 1 keV, the accordance between experimental findings and results from simulations is less distinct. The discrepancy between experimental data and calculated results are also reported in the literature, i.e. for silicon (figure 4 of [73]).

7.3 Comparison with literature data

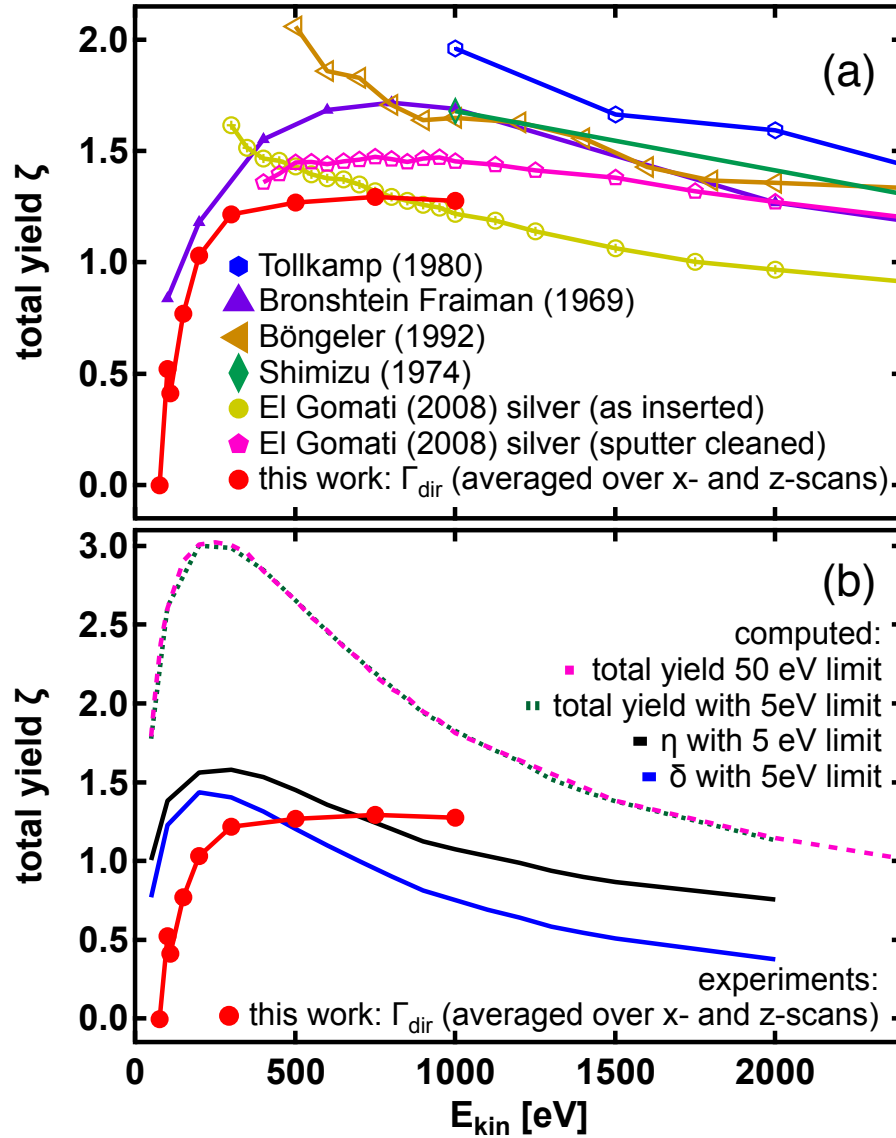


Figure 7.10: Total external electron emission yield ζ for silver as a function of the primary kinetic energy. (a): Comparison of results for Γ_{dir} from this work (averaged results obtained from x - and z -scans as shown in 7.5) with literature data obtained by summing up backscattering and secondary electron yield $\eta + \delta = \zeta$: Tollkamp 1980 (Diploma Thesis) [70], Bronshtein Fraiman (1969) [60] found in [74, 1], Böngeler (1992) [67], Shimizu (1974) [29] and El-Gomati (2008) [71, 72]. (b): Comparison of results from this work with results of Monte-Carlo simulations using Casino 3.3 [73, 20]. See also [13].

The experimental results for Γ_{dir} as shown in panel (a) of figure 7.5 can be compared to results for the total electron emission yield ζ as reported in the literature. Values for ζ were obtained by summing up results for the backscattering coefficient η and for the secondary

electron emission coefficient δ (shown in figure 7.6) using the equation $\zeta = \delta + \eta$ (see equation 4.1). The results reported in the literature are just a few [1] and the scattering between literature data from different authors are quite large. Therefore only data reported from the same authors and the same samples were summed and shown in panel (a) of the figure 7.10. In principle, the values for Γ_{dir} obtained in the experiments reported here for low primary impact energies are in good agreement to the results reported from Bronshtein Fraiman [60]; the results for higher impact energies are similar to the results reported from El-Gomati and Walker [71, 72] for silver "as inserted". Possible differences between the results might be caused by the different detection approaches, since most of the results reported in the literature were obtained by using external detectors, while the results for Γ_{dir} were obtained by evaluating the specimen current. In panel (b) of figure 7.10, the measured results for Γ_{dir} are compared to results from computer simulations using the Casino Monte-Carlo package as discussed in section 7.2 and shown in figure 7.6 for irradiation of a multi-layer sample similar to the MIM structure at the active area position. The dashed curves were obtained by summing up calculated results for δ and η as shown in figure 7.6. As discussed in the previous section, the values obtained for η and δ with an artificially reduced lower energy limit are in better agreement to the experimental findings, as visible by the blue and black solid curves shown in panel (b) of figure 7.10.

The experimental curves with the best agreement to the measured values for Γ_{dir} are shown as half-logarithmic plot in panel (a) of figure 7.11, to improve the overview. In panel (b) of the figure, results for Γ_{dir} obtained by evaluating z -scans in *probe bottom* mode for irradiation of the oxide covered aluminum are shown along with results from El-Gomati and Walker [71, 72] for irradiation of sputter cleaned and uncleaned aluminum. The values for Γ_{dir} are in good agreement to the values reported for uncleaned aluminum, which is not surprising, since the surface of the MIM's aluminum film is intentionally oxide covered; a non-sputter cleaned aluminum sample will also be covered by a generic oxide.

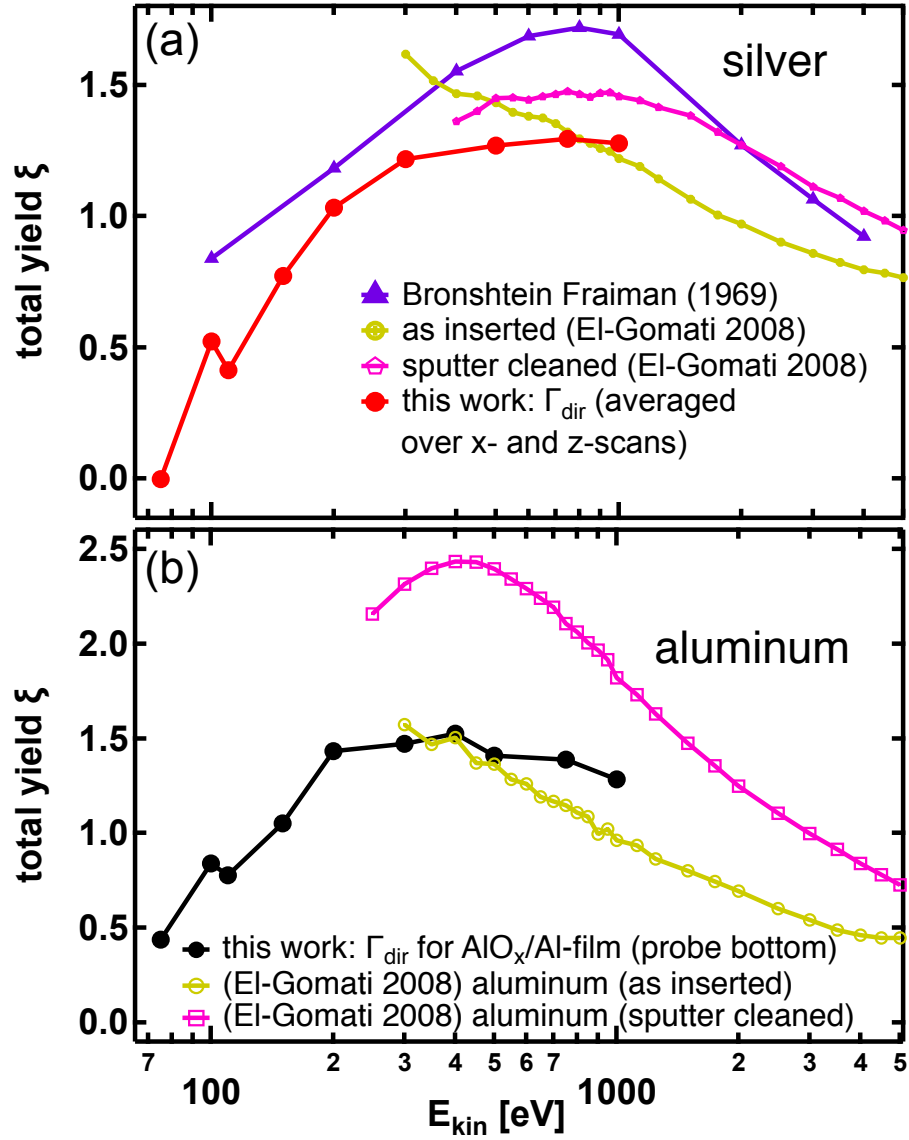


Figure 7.11: Total external emission yield ζ (a) for silver and (b) for aluminum as function of the primary impact energy: Comparison of literature data (obtained by summing up the backscattering coefficient η and the secondary electron coefficient δ) as reported in [71, 72, 60] with experimental results from this work. The values for Γ_{dir} in panel (a) are taken from figure 7.5; the values for irradiation of the oxide covered aluminum in panel (b) were evaluated from part (b) of figure 7.4 at $z = 142$ mm, calculated in the same manner. See also in [13].

7.4 Comparison of different measuring equipment

To neglect an influence of the measuring equipment on the measured sample currents, a comparison of measurements was performed using the potentiostat (Heka PG 510), a picoammeter (Keithley 6487) and current/voltage (I/U) converters (custom built and Femto DLPCA-200, respectively). As shown in figure 7.12, the obtained results measured with the potentiostat (blue curves) are practically identical with the results obtained using an I/U-converter (panels (a)-(c)). The result obtained with the picoammeter (see panel (d)) show in principle the same features like the ones obtained with the potentiostat. The normalized currents show a significant difference, when the active area is irradiated within the interval of $142.5 \text{ mm} \leq z \leq 146.5 \text{ mm}$ and are almost identical when the oxide covered aluminum is irradiated for z -values outside the interval. This is most likely not caused by the measuring method, but rather by the different kinetic energies and therefore a fingerprint of the emission behaviour. Unfortunately, no data sets with identical kinetic energy are available for comparison.

It can be concluded that the chosen measuring device does not significantly alter the results, although the the software noise filtering necessary when not the potentiostat with its built in filters is used, might change the curve form a little bit.

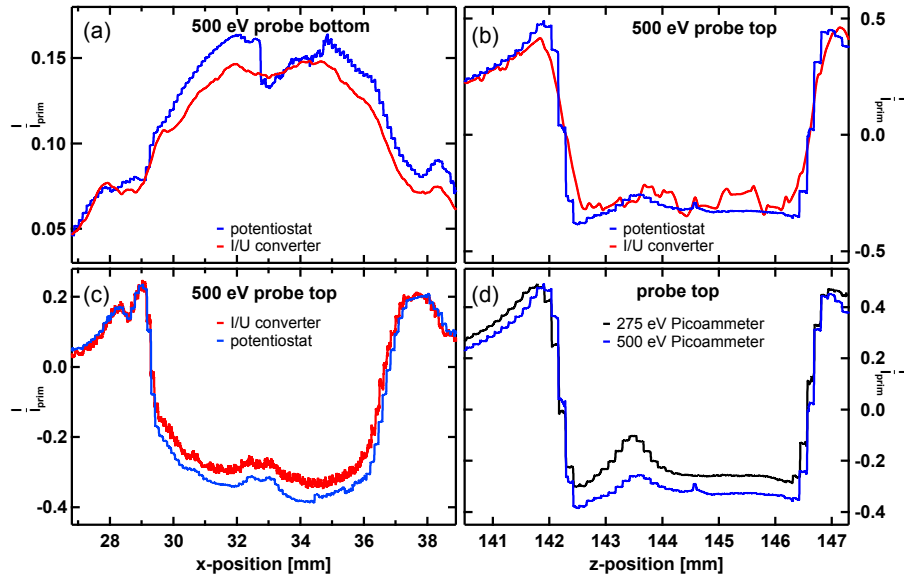


Figure 7.12: Comparison of current curves normalized to I_{prim} : blue curves: measured with potentiostat, red curves: measured with I/U converter, black curve: measured with picoammeter (a) x -scans in the *probe bottom* mode at 500 eV, (b) z -scans in the *probe top* mode at 500 eV, (c) x -scans in the *probe top* mode at 500 eV, (d) z -scans in the *probe top* mode at 300/275 eV

7.5 Dependence of the direct emission yield Γ_{dir} and the indirect emission yield Γ_{indir} on the impact angle

The impact angle dependence (with the impact angle being measured relative to the surface normal) was examined by performing x -scans, to avoid the typical beam walk-off, if a sample is rotated and not perfectly mounted on the rotational axis. Typical results for the external electron emission yield Γ_{dir} at a primary impact energy of 500 eV obtained in *probe top* mode are shown in panel (a) of figure 7.13; results for Γ_{indir} measured in *probe bottom* mode in panel (b) of the figure. In panel (c), the full width at half maximum in *probe bottom* mode as function of the impact angle is shown for primary impact energies of 250 eV, 500 eV and 750 eV. The decrease of the peak width is well-fitted by the plotted cosine-function and is therefore assigned to a geometrical effect. To evaluate the data for Γ_{dir} and Γ_{indir} , respectively, as shown in panels (a) and (b) of figure 7.13, the plateau values of the peaks were read out.

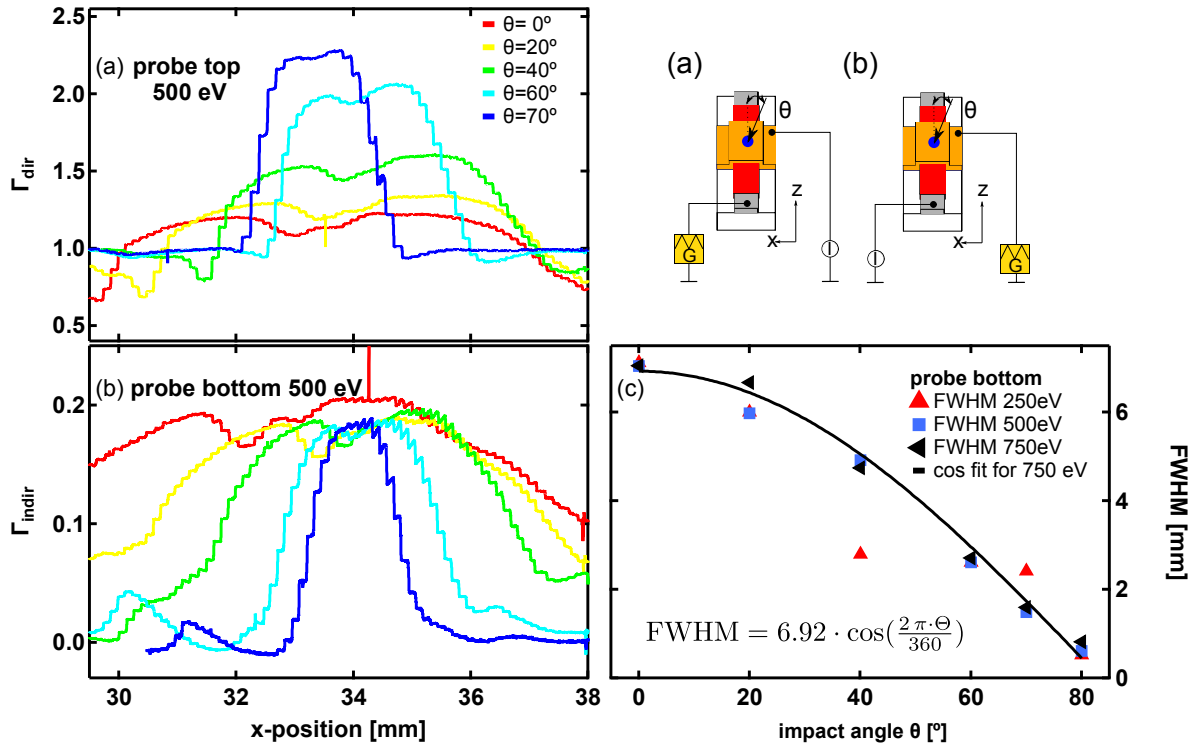


Figure 7.13: x -scans along the silver top electrode at $E_{\text{prim}} = 500 \text{ eV}$ in (a) the *probe top* mode (see insert (a)) and in (b) the *probe bottom* mode (see insert (b)), recorded at different impact angles. In (c) the full width at half maximum as function of impact angle θ for different E_{prim} is shown. See also in [13].

The results obtained this way are shown in panels (a) and (b) of figure 7.14; an impact angle of 0° corresponds to normal incidence, and of 90° to grazing incidence. The *direct* electron emission yield Γ_{dir} increases with increasing impact angle, the *indirect* emission yield Γ_{indir} is found to be practically independent of the impact angle.

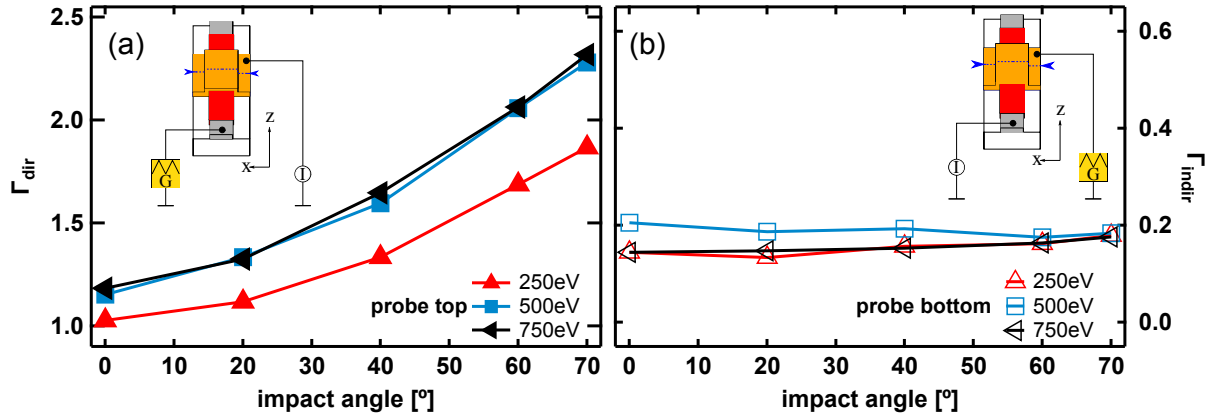


Figure 7.14: (a): Γ_{dir} measured in *probe top* mode under irradiation of the top silver electrode in the center of the active area for different primary impact energies evaluated from panel (a) of figure 7.13. (b): Γ_{indir} measured in *probe bottom* mode for different primary impact energies evaluated from panel (b) of figure 7.13. See also in [13].

The observed increase of the *direct* emission yield in line with the observed behaviour reported in the literature for the external electron emission. Unfortunately, to the best of the author's knowledge, no direct comparable experiments on silver were reported in the literature, but some on copper and gold [70, 67] and on clean molybdenum found in [75] measured by Shih and Hor. The measurements from Tollkamp [70] and from Böngeler [67] were performed in a low-voltage SEM distinguishing between secondary and backscattered electrons. Therefore the data were summed to obtain the total external electron emission yield ζ and normalized to the values at normal incidence ($= 0^\circ$ relative to surface normal). The measurements by Shih and Hor were performed on clean molybdenum ribbons, biased to negative voltages (-72 V) to push emitted electrons away from the surface. Due to the negative bias, no effort was made to distinguish between secondary electrons and backscattered electrons, which was not done, either, in this set of experiments performed for this thesis.

In figure 7.15, the experimental results for Γ_{dir} obtained on the active area of a MIM are shown, along with experimental data as reported from the literature. For comparison, the simple $\frac{1}{\cos(\theta)}$ -approach as proposed in [76] is shown as dotted line. All data are normalized to the results for normal incidence. In all cases, the increase of the measured results is smaller than the $\frac{1}{\cos(\theta)}$ -increase. However, the experimental results for Γ_{dir} show qualitatively a good agreement to the results reported by Shih and Hor and to the results reported by Böngeler and by Tollkamp. A more sophisticated comparison is not possible, since the surface roughness of the samples used by Tollkamp and Böngeler are not specified, bulk samples were used instead of thin-film devices and the materials were made of different chemical elements.

The negligible impact angle dependence of the indirect electron emission yield Γ_{indir} indicates, that a fundamentally different process seems to be involved there. This observed

behaviour contradicts the results obtained for similar MIM systems under Ar^+ -irradiation, e.g. reported in [57] and also shown in figure 8.9 on page 95, where the internal emission yield was found to be constant for impact angles from normal incidence up to 40° , and decreasing to $\approx 10\%$ of the initial value at 80° . Again, to the best of the author's knowledge, no other comparable data are available. As discussed in section 7.2, the simulation of detectable currents as function of the impact angle is not easily possible using casino 3.3. Therefore the observed behaviour cannot be compared to other data sets.

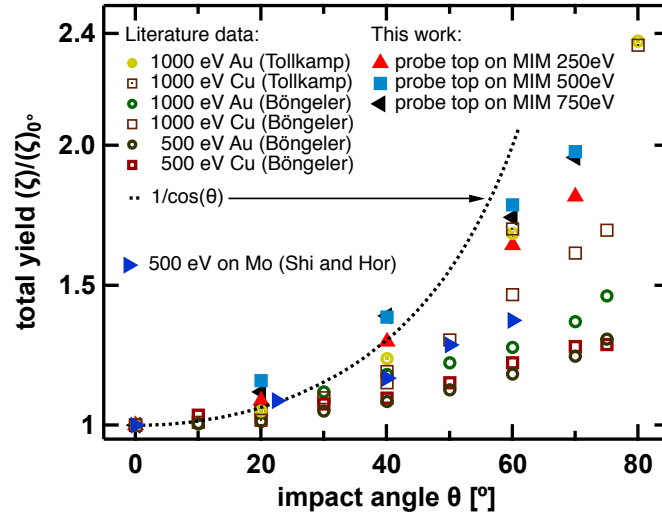


Figure 7.15: Results of the measured impact angle dependencies of the external electron emission yield Γ_{dir} in case of MIM experiments and of the total yield ζ in case of literature data. All data normalized to the signal at normal incidence. Results of MIM measurements as shown in panel (a) of figure 7.14, molybdenum ribbons from Shih and Hor [75], silver and copper bulk samples [67, 77] and Tollkamp [70]. See also in [13].

7.6 Influence of a bias voltage on Γ_{indir}

If an internal bias voltage between top and bottom electrode of the MIM is applied, the oxide barrier is modified, since the application of a bias voltage shifts the Fermi level upwards or downwards, depending on the polarity of the voltage. Therefore, either the electron or the hole transport across the internal barrier is eased or inhibited, as discussed in section 6.6. The bias voltage was applied in form of a voltage ramp to the top silver electrode of the MIM, which allows to study the functional dependency of the internal currents on the bias voltage in a convenient way. As discussed in section 5.1, the voltage feed s of the applied voltage ramp influences the dynamic capacitance C_d of the MIM, and therefore influences the current induced by the applied voltage ramp. When analyzing the bias dependence of the measured internal currents, this effect needs to be considered. The evaluation of a typical bias dependent measurement under electron irradiation is shown in figure 7.16. The left ordinate axis is the voltage axis for the applied voltage ramp (black

curve); the right ordinate axis is the current axis for the blue and the red curve. To obtain the bias dependent current curve without dielectric effects, the value for ΔI is determined from the initial current jump, when the voltage ramp starts. This value is subtracted twice from current trace between the upper and lower limit bias voltage limit. The blue current curve results from this subtraction and represents the true bias-dependent current. Using this current, the *internal* and *external* emission yields can be calculated using equations 6.5 and 6.6, respectively, which can be plotted against the applied bias voltage, as shown in figure 7.17.

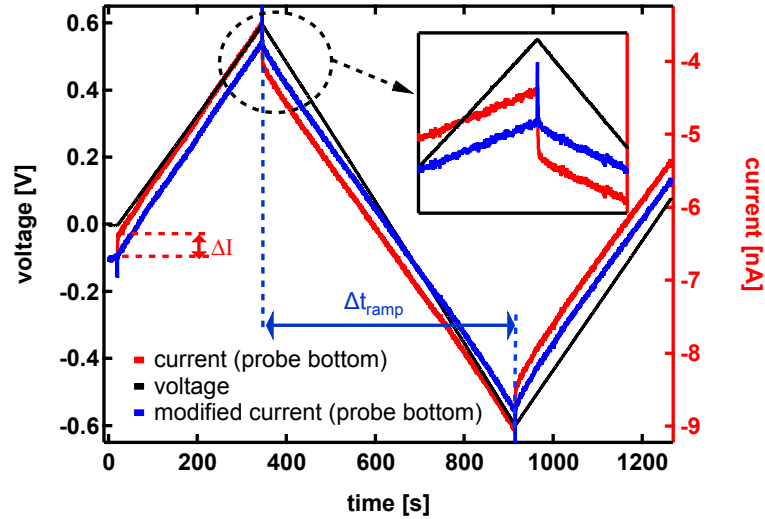


Figure 7.16: Black curve (left ordinate axis): Applied bias voltage as function of time. Red curve (right ordinate axis): Current answer of the MIM to the applied voltage ramp under electron irradiation as function of time. Blue curve (right ordinate axis): Corrected current answer of the MIM obtained by subtracting $2 \cdot \Delta I$ from the red curve between maximal and minimal bias voltage to remove the influence by dielectric effects. Measured under irradiation of the active area for $I_{\text{prim}} = -24.1$ nA at $E_{\text{prim}} = 275$ eV. See also in [13].

In figure 7.17, the influence of the bias voltage to the *indirect* emission yield is shown for different kinetic energies. While Γ_{indir} is reduced for negative bias voltages in comparison to the value at 0 V-bias, it increases for positive bias voltages. This can be explained by the retarding field for electrons established by the negative bias voltage like discussed in panel (b) of figure 6.11, combined with an eased transport of excited holes, since the *internal* current I_{int} consists of both contributions which cannot be separated (as discussed above). For positive bias voltages, a retarding field for excited holes is established by the bias voltage, combined with an eased transport of excited holes like discussed in panel (c) of figure 6.11. Apparently, the influence of positive bias voltages is weaker than the influence of negative bias, which is surprising at this point. The clear difference between the measured bias-dependence for 275 eV in comparison to the results measured for higher primary impact energies is also surprising.

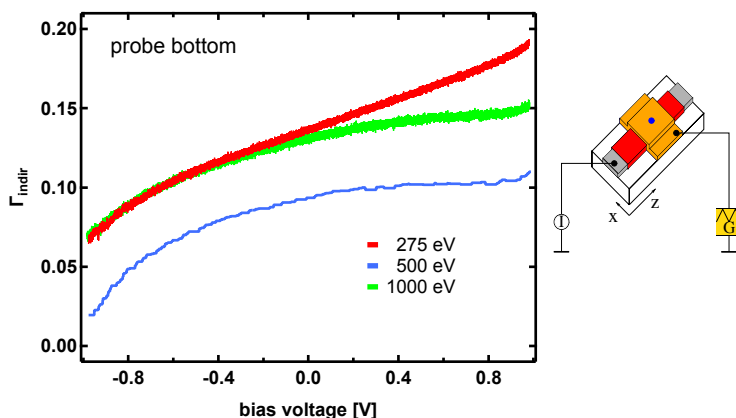


Figure 7.17: Internal emission yield Γ_{indir} as function of the bias voltage measured in *probe bottom* mode for different kinetic energies, obtained like described in 7.16. Also see in [13].

As an alternative to the *internal* transport, an *external* cross-absorption process is discussed, which might explain the observed behaviour. Therefore it is assumed, that at least a part of the low-energetic secondary electrons emitted from the irradiated surface as consequence of the primary electron irradiation are absorbed in the non-irradiated electrode circumventing the oxide barrier. As discussed above, the reasons for this cross-absorption might be the built-up of a space charge above the surface on the one hand or the change of the electrode's potential due to the application of a bias voltage on the other hand (or a combination of both processes), resulting in a notable current of externally emitted and cross-absorbed electrons. The situation is sketched in figure 7.18: In panel (a), where no bias voltage is applied, only a small fraction of the emitted low-energy electrons are reflected towards the sample by their own space-charge. High-energy electrons are less likely affected by external fields and will not significantly contribute to this process. The reflected electrons might either impinge on the irradiated electrode and contribute to the re-absorption current or impinge on the (oxide covered) aluminum and therefore contribute to the cross-absorption process. In panel (b) of the figure, the situation is sketched for a negative bias voltage, where the aluminum electrode has a negative potential with respect to the top silver electrode and low-energy electrons are deflected away from the aluminum and a cross-absorption process is unlikely. In panel (c) of the figure, the situation is sketched in case of a positive bias voltage, where the probability for across-absorption process is increased, since the positive potential on the aluminum electrode is an attractive potential for low-energetic electrons emitted from the irradiated silver electrode.

Both alternative models to describe the observed bias dependence well in case of negative bias values, since both would cause a reduction of the *internal* current in case of *negative* bias. The fact that the positive bias voltage has only a weak effect on the measured current is understandable in the terms of the cross-absorption process, since only a limited number of low-energetic electrons is attracted by a small potential difference of 1 V. The fact, that the overall shape of the curves for positive bias voltages is different for a primary

impact energy of 275 eV in comparison to the curve shape for 500 eV and 1000 eV might also point in direction of a process mediated by (external) cross-absorption.

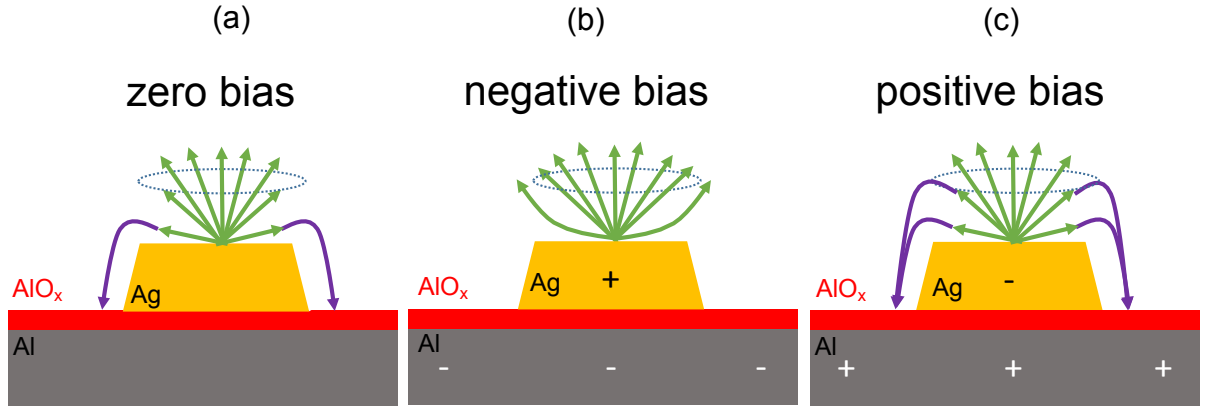


Figure 7.18: Influence of the bias voltage on the externally emitted secondary electrons: (a): zero bias; (b): negative bias (c): positive bias. See also [13].

7.7 Influence of a bias voltage on Γ_{dir}

The bias voltage dependence of the *external* electron emission yield Γ_{dir} was also measured, but is not easily understandable by the models discussed above. For the sake of completeness, the measurement is shown here in figure 7.19. However, it is hardly understandable that the modification of the internal oxide barrier causes such a strong modification of the *direct* emission yield as observed in the figure.

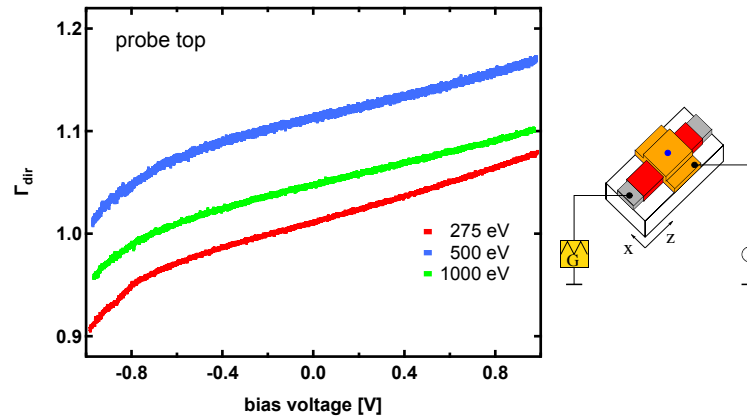


Figure 7.19: External emission yield Γ_{dir} as function of the bias voltage measured in *probe top* mode for different kinetic energies, obtained like described in 7.16. See also in [13].

The sign of the bias-voltage in case of measurements in the *probe top* mode was inverted. Therefore panel (b) of figure 7.18 describes *positive* bias voltages in case of *direct* experiments and panel (c) describes *negative* bias voltages in case of *direct* experiments. A

positive bias voltage causes an *increase* of the external electron emission yield Γ_{dir} due to the repelling of electrons away from the sample as depicted in panel (b) of figure 7.18, while a *negative* bias voltage leads to a *decrease* of Γ_{dir} due to an *increase* of a cross-absorption effect. This is also the observed behaviour in the figure 7.19, which further supports the hypothesis, that an external is involved.

7.8 Discussion

This discussion can also be found in similar form in [13].

The following findings are observed for the *direct* emission yield Γ_{dir} , which is determined in *direct* experiments: *Direct* experiments (i.e., irradiation of the active area and current measurement in *probe top* mode) show a clear dependence on the primary impact energy as observed in panel (a) of figure 7.5. This is in line with measurements reported in the literature and can be qualitatively simulated using the Casino Monte-Carlo package as shown in figures 7.10 and in 7.11. The observed *increase* of the *direct* emission yield with increasing impact angle (see figure 7.14) correlates qualitatively also to results as reported in the literature (see 7.15). The yield strongly depends on the bias voltage as visible in figure 7.19.

The following findings are observed for the *indirect* emission yield Γ_{indir} , which is determined in *indirect* experiments: *Indirect* experiments (i.e., irradiation of the active area and current measurement in *probe bottom* mode) show no significant dependence on the primary impact energy as observed in panel (b) of figure 7.5. Due to the lack of comparable experimental data in the literature, unfortunately neither a comparison to literature data nor to results from simulations can be drawn. No significant dependence on the impact angle is observed (see figure 7.14), which contradicts experimental findings obtained on similar MIM devices under Ar^+ -irradiation, e.g. reported in [57], where a clear impact angle dependence was observed. The yield strongly depends on the bias voltage as visible in figure 7.17. The behaviour can be either interpreted in terms of a retarding field for electrons in case of negative bias voltages and of a retarding field for excited holes in case of positive bias voltages or in terms of external re-absorption/cross-absorption processes circumventing the internal barrier.

The influence of *externally* mediated currents evoking by re-absorption and/or cross-absorption processes were not taken into account in earlier MIM experiments, which were interpreted by *internal* currents, only, as reported in [11, 12, 2, 12].

An additional experiment shown in figure 7.20 was performed to further examine *indirect* experiments by irradiating the silver electrode while measuring the current into the aluminum *bottom* electrode at 500 eV (which is also shown in figure 7.3) and by measuring the current in *probe top* mode while irradiating the glass substrate/ the oxide covered aluminum electrode some millimeters away from the top silver film, which is the *indirect* experiment corresponding to the experiments shown in figure 7.2. The blue curve labeled with (1) in 7.20 was performed by moving the electron beam like indicated by the dashed

blue line in pictogram (1) of the figure. The detection of positive (normalized) currents in the top silver electrode while irradiating the glass substrate corresponds to the flux of negative charge carriers into the top silver electrode, which is also the case for irradiation of the oxide covered aluminum (for $31 \text{ mm} < x < 35 \text{ mm}$). This transport over a distance of several millimeters is most likely caused by the emission of secondary electrons from the irradiated surface and a cross-absorption process as discussed in panel (c) of figure 7.18.

Also the red curve labeled with (2) in figure 7.20 shows a behaviour challenging the picture of exclusively *internal* transport effects, since an almost linear *increase* from $29 \text{ mm} \leq x \leq 31 \text{ mm}$ and symmetrical to this a *decrease* from $35 \text{ mm} \leq x \leq 37 \text{ mm}$ is observed (also indicated by the ellipsoids in the figure. This is only understandable assuming either an internal transport over long distances or, (more likely) by external electron emission and cross-absorption processes.

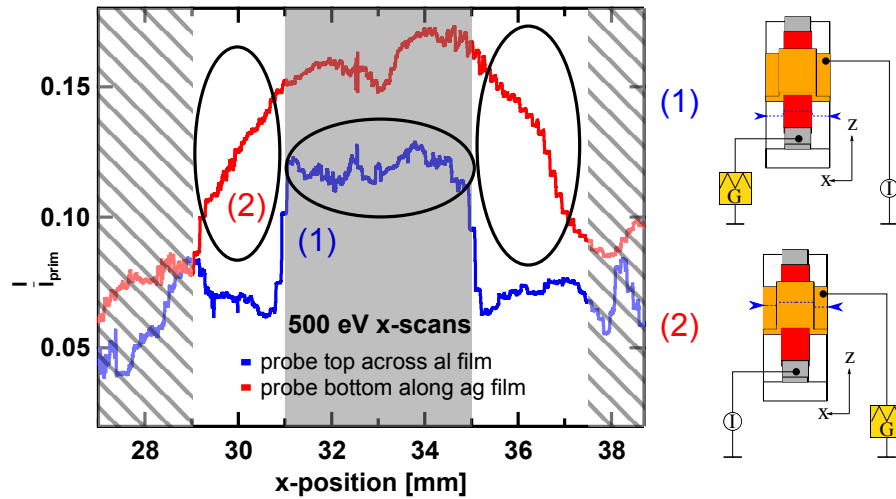


Figure 7.20: x -scans to determine the position of the active area (1) in *probe top* mode with electron beam being scanned like depicted by the dashed blue line in pictogram (1): path from glass/ AlO_x on Al/glass (2) in *probe bottom* mode with electron beam being scanned like depicted by the dashed blue line in pictogram (2): path from silver on glass/active area/silver on glass with 500 eV kinetic impact energy. The grey box indicates the position of the aluminum film, which is also the underlay of the active area. Taken from [13].

The decay observed in figure 7.20 was already observed in panel (b) of figure 7.3. Since the signal decreases with increasing distance to the active area (and increases with decreasing distance), the transport leading to this phenomenon depends linearly on the travel distance. A mean free path length of the order of 1 mm is determined from this decay. A very high mean free path length is only possible for electrons with low excitation energies of $\approx 10 \text{ meV}$ above the Fermi level, which can be deduced from the $(E - E_{\text{Fermi}})^{-2}$ scaling for the electron-electron mean free path as found in [78]. Electrons with this low excitation energy could be transported to the internal barrier, but it seems very unlikely that they would be able to overcome the barrier of several eV height and of 3 nm thickness.

For irradiation of the oxide covered aluminum, the *direct* electron emission yield is determined in a *direct* experiment (see curve (1) in figure 7.2) to a value of $\Gamma_{\text{dir}} \approx 1.1$, while the yield measured in the corresponding *indirect* experiment (see curve (1) in figure 7.20) is determined to a value of $\Gamma_{\text{indir}} \approx 0.12$. Assuming that these yields are caused by externally mediated transport effects, this can be interpreted in terms of a probability $P_{\text{abs}} \approx 10\%$, that an electron emitted from the oxide covered aluminum is (cross-) absorbed in the top silver electrode. Evaluating the curves labeled with (2) of the same figures leads to values of $\Gamma_{\text{dir}} \approx 1.2..1.3$ and of $\Gamma_{\text{indir}} \approx 0.15$ for irradiation of the active area and therefore to a (cross-) absorption probability $P_{\text{abs}} \approx 12\%$. The curves labeled with (1) were obtained by guiding the electron beam across the sample ≈ 2 mm away from the edge of the silver film, which is also the minimal distance that electrons emitted from the oxide covered aluminum have to travel to the top silver electrode to be detectable as (cross-) absorbed electrons. Electrons emitted from the silver surface (curves labeled with (2)), on the other hand, would only have to travel to the edge of the silver film to be detectable in the bottom aluminum electrode, which might imply a shorter travel distance in comparison to the one of electrons emitted from the aluminum.

Although the externally mediated transport via (cross-) absorption processes seems to explain the observed behaviour of the emission yields fairly well, the *independence* of Γ_{indir} cannot be understood easily in this picture, since the assumption that most of the detected "internal" current is in fact caused by external electrons emitted from the silver externally travelling to the aluminum electrode would imply, that Γ_{indir} shows the same primary impact energy- and impact angle dependence as observed for Γ_{dir} , which is clearly not the case.

A possible way to explain the kinetic impact energy and impact angle independent value of $\Gamma_{\text{indir}} \approx 0.15$ would be a direct penetration of the bottom aluminum electrode by at least a fraction of the primary electrons. To test the validity of this assumption, simulations for a silver film (like the top silver electrode of the MIM) using the Casino Monte-Carlo [20] code have been performed, to calculate the penetration depth of the primary electrons as well as the escape depth, which is the maximal depth (below the surface), from which electrons may be emitted as backscattered electrons into the vacuum. As shown in table 7.1, the penetration depth is even for kinetic impact energies of 2 keV small in comparison to the 40 nm-thick silver electrode. This proves that a direct penetration of primary electrons into the bottom aluminum electrode by crossing the top silver film as well as the oxide barrier is very unlikely to happen.

A truly *internal* transport therefore would require the generation of a broad distribution of low-energy electrons which are somehow transported to the oxide interface between the top silver and the bottom aluminum electrode and somehow overcome this oxide barrier to contribute to the current I_{indir} measured in the aluminum electrode (also see in [13]).

| Energy [eV] | Penetration depth of prim. e ⁻ [nm] | Escape depth of bse [nm] |
|----------------|--|--------------------------------|
| 75 | 0.33 | 0.41 |
| 100 | 0.43 | 0.60 |
| 200 | 0.96 | 1.41 |
| 300 | 1.31 | 1.72 |
| 400 | 1.62 | 1.87 |
| 500 | 1.92 | 2.05 |
| 600 | 2.30 | 1.87 |
| 700 | 2.74 | 2.45 |
| 800 | 3.06 | 1.87 |
| 900 | 3.51 | 2.42 |
| 1000 | 3.83 | 2.56 |
| 2000 | 9.42 | 2.64 |

Table 7.1: Computed impact energy dependence of the penetration depth of primary electrons and of the escape depth of backscattered electrons calculated using the Casino Monte-Carlo package [20] for a 40 nm-thick silver film. Taken from [13].

7.9 Conclusion

The observed dependence of *external* emission currents Γ_{dir} on the primary impact energy and on the impact angle are found to be in good agreement to total emission yields ζ as reported in the literature for measurements on bulk samples. The observed results of the apparently *internal* processes Γ_{indir} suggest a significant influence of *external* processes in form of (cross-) absorption processes circumventing the *internal* barrier, while a direct penetration of the bottom electrode was found to be very unlikely, as simulations with the Casino package prove. At this point it remains an open question, in how far the assumption of involved *external* process is justified. To shed more light on this processes, further experiments with an external collector/repeller electrode were performed (see chapter 8) to control the electric field above the sample.

8 Experimental results obtained with external collector/repeller electrode

Since the experimental findings discussed in the preceding chapter suggest that *external* processes contribute to apparently *internal* device currents, experiments with an additional, bias-able *external* collector/repeller electrode have been performed. The set-up of the experiments is shown in chapter 6.4, the irradiation scenarios in chapter 6.9.

The majority of the figures, all of the results and the whole discussion is going to be submitted to the "Journal of electron spectroscopy and related phenomena" [14]. The discussion follows closely the discussion as given in the submitted manuscript.

Similar to the preceding chapter, experiments as function of the electron impact point will be presented in form of x - and z -scans, respectively, where all other coordinates are fixed and the current is measured during the scan. This is done, since the geometrical impact point influences the irradiation scenario as discussed in 6.9. As before, all currents shown in the following figures are normalized to the primary electron current I_{prim} as measured in the Faraday cup.

This chapter is organized as follows:

- The sample currents in *probe top* and in *probe bottom* mode as function of the position for static voltages of $U_d = \pm 40$ V applied to the external collector/repeller electrode are shown in section 8.1 in the following order:
 1. In sections 8.1.1 and 8.1.2, results of measured sample currents in *probe top* and *probe bottom* mode are shown and discussed.
 2. In section 8.1.3, results of measurements as function of the z -position are shown and discussed. Similar to the results discussed in 7.1.3, the nature of the experiments changes as function of the actual z -position of the primary beam onto the sample surface.
 3. The results of the x -scans are evaluated in terms of the (cross-) absorption current I_{abs} as function of the kinetic impact energy by using the equations shown in section 8.1.4.
 4. The impact angle dependence of the *direct* and *indirect* emission yields Γ_{dir} and Γ_{indir} are shown and discussed in section 8.1.5.

- The dependence of device currents in *direct* as well as in *indirect* experiments on the external electric field above the sample (modified by varying the repeller/collector voltage U_d applied to the external electrode) for a fixed position are presented in section 8.2. This section is organized in the following order:
 1. *Direct* experiments for irradiation of the active area and for irradiation of the silver film outside the active area measured in *probe top* mode and for irradiation of the oxide covered aluminum in *probe bottom* mode are presented in section 8.2.1. From these results, the primary impact energy dependence is extracted.
 2. *Indirect* experiments obtained by irradiating the active area as well as the silver film outside the active area in *probe bottom* mode and by irradiating the oxide covered aluminum in *probe top* mode are presented in section 8.2.2. Also from these results, the primary impact energy dependence is extracted.
- The total (external) electron emission yield ζ is determined from the sample current measured in *direct* experiments (x -scans) and from the current measured onto the external electrode and these findings are compared to literature data in section 8.2.3.
- The dependence of Γ_{indir} in case of an applied internal bias voltage on the external electric field is presented and discussed in section 8.2.4 as measured in *probe bottom* mode for irradiation of the active area.
- The dependence of Γ_{dir} in case of an applied internal bias voltage on the external electric field is presented and discussed in section 8.2.5 as measured in *probe bottom* mode for irradiation of the active area.

8.1 Position dependent current measurements

As shown in figure 6.14 on page 41, the impact point of the e^- -beam - in connection with the current measuring mode (*probe top* and *probe bottom*, respectively) influences the nature of the experiments (*direct* vs. *indirect*).

i) Irradiation on positions 1 and 2 (located on the silver film *within* and *outside* the active area, respectively) along with a current measurement in *probe top* mode represents a *direct* experiment, since the current into the irradiated electrode is monitored. The same applies to irradiation on position 3 (located on the aluminum film on top of the glass) and measurement in *probe bottom* mode.

ii) Irradiation on the positions 1 and 2 (silver film) along with a current measurement in the *probe bottom* mode and irradiation on position 3 (aluminum electrode) along with a current measurement in the *probe top* mode constitute *indirect* experiments, where the current monitoring electrode is different from the irradiated electrode. Therefore, during a z -scan from position 1 to position 3 the nature of the experiment changes from *direct* to *indirect* in *probe top* mode and vice versa in *probe bottom* mode. Examples of such experiments are discussed in section 8.1.3. In contrast, the nature of the experiment does

not change during x -scans from position 1 to position 2, which are discussed in sections 8.1.1 and 8.1.2. More specifically, the experiment remains *indirect* in *probe bottom* mode and *direct* in *probe top* mode throughout the entire scan. This means that x - and z -scans need to be analyzed differently depending on the irradiation scenario.

8.1.1 x -scans – Finding the active area on the sample

Similar to experiments described in chapter 7.1.1, the first aim was to determine the x -coordinates of the active area. Therefore, x -scans with a primary kinetic impact energy of 500 eV in the probe bottom mode were performed following a path outside the silver film (at $z = 149.5$ mm, about 1 mm away from the edge of the active area) as indicated by the dashed blue line in pictogram (1) of figure 8.1 on page 81). Following this path, the electron beam irradiates the external electrode above the sample for $x < 34$ mm, the glass substrate for $x < 35$ mm, the oxide covered aluminum film for $35 \text{ mm} \leq x \leq 39$ mm and again the glass substrate for $x > 39$ mm. In case a positive voltage U_d is applied to the external electrode (like in panel (a) of figure 8.1), electrons emitted from the irradiated electrode are drained towards the external electrode and are therefore prevented from reaching the sample again. In this case, the external electrode is no source of electrons. As a consequence of this external field, the current measured onto the aluminum electrode is practically zero (see curve (1) in panel (a) of 8.1) if the glass substrate is irradiated, and reaches negative values, if the oxide covered aluminum is irradiated (for $35 \text{ mm} \leq x \leq 39$ mm). The measured negative currents of $\frac{I}{I_{\text{prim}}} \approx -1.5$ in the latter case correspond to an external electron emission yield of $\Gamma_{\text{dir}} = 2.5$, indicating the emission of 2.5 electrons per impinging primary electron. Such a high emission yield on oxide covered aluminum is in the literature known as Malter effect [79] and can be explained by a reduced work-function due to the thin oxide layer [80]. The corresponding experiment performed with a negative voltage U_d applied to the external electrode is shown as curve (1) in panel (b) of the figure. In this case, secondary electrons emitted from the irradiated electrode are repelled towards the sample and, in addition, electrons emitted from the external electrode may impinge on the sample. As a consequence, the current for irradiation of the glass substrate measured in the aluminum electrode is positive, indicating a flux of electrons into the aluminum electrode. This indicates, that also in the experiments without external electrode (as described in section 7.1.1), a repelling of secondary electrons occurred. If the oxide covered aluminum is irradiated in case that $U_d = -40$ V, the external electron emission yield Γ_{dir} remains positive at values of ≈ 0.5 .

Results from x -scans in *probe top* mode across the top silver electrode performed at $z = 147.3$ mm are labelled with (2) in figure 8.1. Results obtained with $U_d = +40$ V applied to the external electrode are shown in panel (a) of the figure, the ones obtained with $U_d = -40$ V in panel (b). Both curves labelled with (2) show a linear signal change between $33 \text{ mm} \leq x \leq 34$ mm, which is caused by the fact that there the electron beam leaves the external electrode towards the sample.

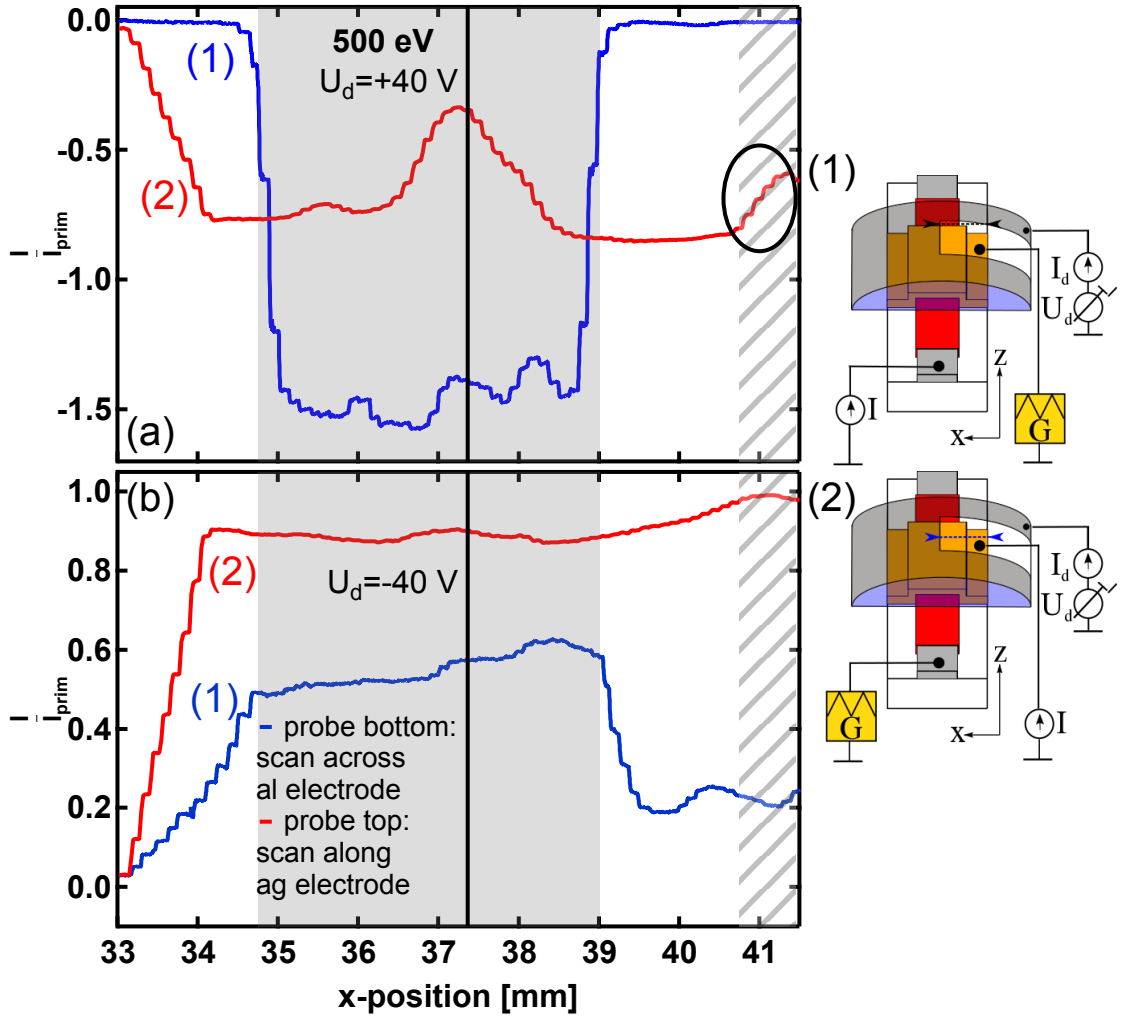


Figure 8.1: (a): (1) Normalized current measured in the bottom aluminum electrode as a function of the x -position with $U_d = +40$ V during a scan of the primary electron beam across the aluminum electrode (see pictogram (1)). (2) Normalized current measured in the silver top electrode as a function of the x -position with $U_d = +40$ V for scanning across the silver electrode (see pictogram (2)). (b): like in (a) but for $U_d = -40$ V. The black line indicates the x -position where the z -scans (see below) were performed. The area for $x > 40.5$ mm is shaded, since the silver film is left there towards a carbon contact. See also in [14].

In case of $U_d = +40$ V, the irradiation of the silver film leads to a negative normalized current of $\frac{I}{I_{\text{prim}}} \approx -0.75$ with a local maximum at a x -position of 37.4 mm. Since at this x -position the z -scans were performed, this is assigned to a local carbon contamination as discussed in chapters 7.1.2 and 6.1.4. The measured (normalized) currents correspond to $\Gamma_{\text{dir}} = 1.75$ for irradiating the silver film outside the carbon contamination and to values $\Gamma_{\text{dir}} \approx 1.4$ for irradiation within the carbon contamination. For $34 \text{ mm} \leq x \leq 41 \text{ mm}$ the silver top electrode of the MIM is irradiated. The change in the measured normalized

current for $x > 41$ mm can be assigned to an irradiation of the carbon contact area like discussed in section 7.1.1, therefore this scan area is shaded and not shown in the following plots. The reason for the difference between the current measured for $x < 37$ mm and for $x > 39$ mm remains unclear at this point.

In case of $U_d = -40$ V, the current measured in *probe top* mode (see panel (b) of figure 8.1) for irradiation of the silver top electrode ($x > 34$ mm) shows an almost constant normalized current of $\frac{I}{I_{\text{prim}}} \approx +0.9$, which indicates an electron flux of about 90% of I_{prim} into the top silver electrode, since the normalized current is positive. The corresponding external electron emission yield Γ_{dir} reaches values of $\Gamma_{\text{dir}} \approx 0.1$ according to $\Gamma_{\text{dir}} = 1 - \frac{I}{I_{\text{prim}}}$. At these negative voltages of U_d , the external electrode is also a source of electrons, which may be caused by electrons backscattered from the sample towards the external electrode. During their impact on the external electrode, they might cause the emission of low energetic, secondary electrons that leave the external electrode towards the sample. The electrons backscattered on the sample might also be backscattered again on the external electrode and leave this electrode towards the sample, as discussed in chapter 6.10.2. The position of the active area is indicated by the grey box in the figure (as well as in the following figures) and is located between $x \approx 35$ mm and $x < 39$ mm, since in this x -range especially the signal in *probe bottom* mode at *positive* external collector voltage shows a pronounced change due to irradiation of oxide covered aluminum instead of irradiating the glass substrate.

The fact, that secondary electrons are emitted from the glass substrate, may be surprising on the first glance, but in fact this was already measured in case of Pyrex glass in 1945 [81]. The electrons impinging on the glass interact with a good insulator. The band gap of glass is ≈ 8 eV [82], while the energy of the impinging primary electrons is at least 13 times higher, which will lead to a secondary electron emission from the glass substrate. If the total emission yield $\zeta < 1$, the surface will charge up negatively, which will guide primary electrons away from that spot. In case of $\zeta > 1$, a positive charge will build up, holding back a part of the secondary electrons. As a consequence of this, a dynamic equilibrium is established which causes a zero net current into the glass substrate. However, secondary electrons emitted from the glass substrate might be reflected by the external electron field and can possibly impinge on the silver surface, where they are detected.

As discussed in chapter 11, when the external field in case $U_d < 0$ V is applied, the field indeed causes a reflection of emitted electrons, but these electrons may impinge anywhere on the sample and not necessarily on their emission position, which complicates the re-absorption/cross-absorption processes.

8.1.2 x -scans for different kinetic impact energies

Results of x -scans performed at different primary impact energies in the *probe top* mode for positive voltages $U_d = +40$ V applied to the external electrode are shown in panel (a) of figure 8.2, results of similar scans with the only difference, that $U_d = -40$ V was applied, are shown in panel (b) of the same figure. The path of the electron beam is indicated by the

blue dashed line in the pictogram in the corresponding figure. In both panels and for all kinetic impact energies, a linear change of the signal is observed for $33 \text{ mm} \leq x \leq 34 \text{ mm}$ due to the fact, that the electron beam leaves the external electrode and irradiates the sample instead, like discussed in the preceding section. For $U_d = +40 \text{ V}$ (see panel (a)) of figure 8.2), the curves resulting from primary impact energies of 125..250 eV show a more or less constant negative normalized current of $\frac{I}{I_{\text{prim}}} \approx -0.85$ throughout the scan. The curves resulting from measurements at higher kinetic energies 500..1000 eV show pronounced local extreme values at $x = 37.3 \text{ mm}$ due to a carbon contamination, corresponding to a reduced external electron emission yield at this position. Also outside the carbon contaminated area, a pronounced dependence on the primary electron impact energy is observed in case of primary energies above 500 eV.

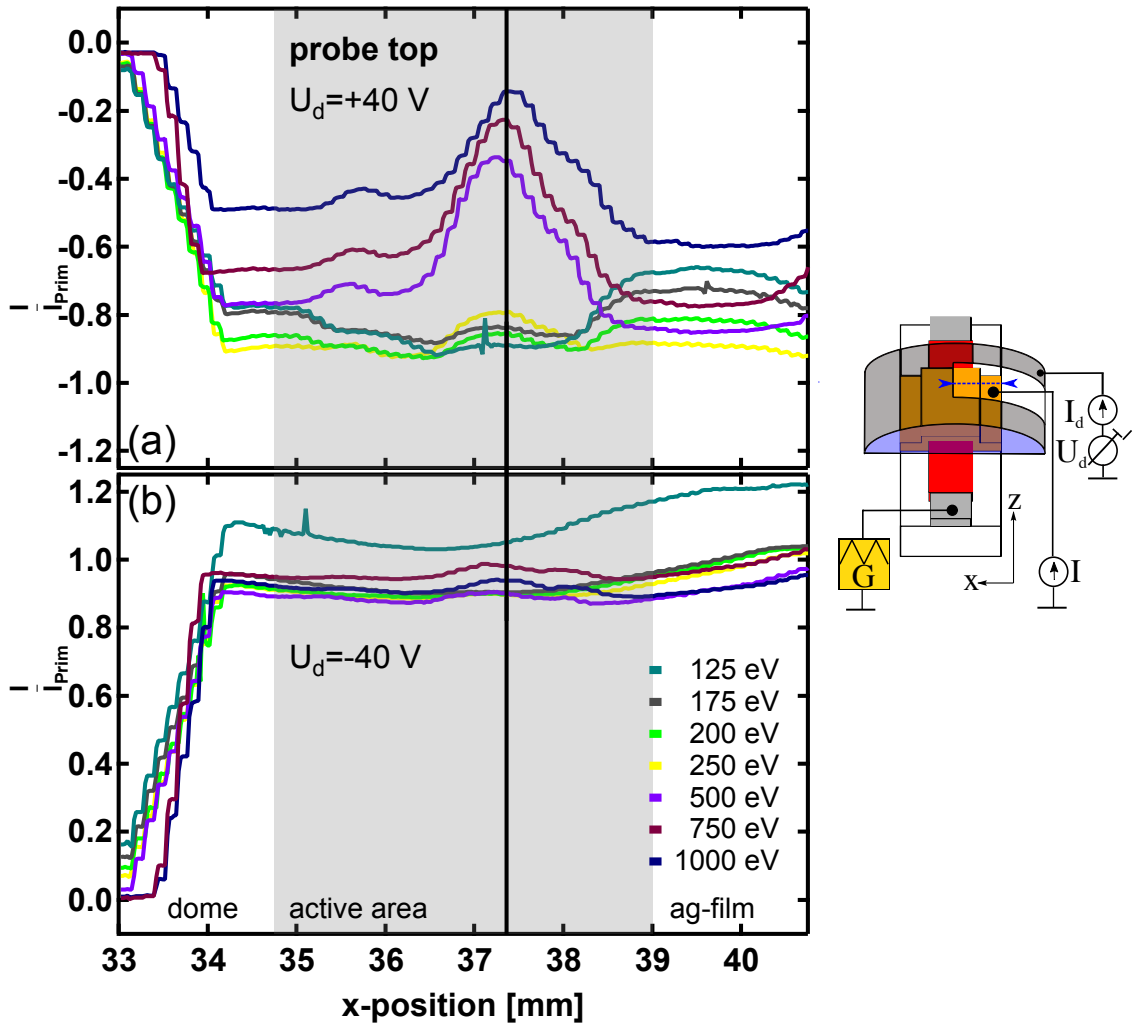


Figure 8.2: (a): Current in *probe top* mode measured in the silver electrode normalized to the primary current as function of the x -position scanning across the active area for $U_d = +40 \text{ V}$. The black line indicates the x -position at which the z -scans were performed. (b): Like in (a) but with $U_d = -40 \text{ V}$. See also in [14].

In case, the emitted secondary electrons are repelled by the negative repeller voltage of $U_d = -40$ V (panel (b) of figure 8.2), no pronounced dependence on the primary impact energy is observed. Only the curve for the lowest impact energy of 125 eV reaches higher positive values of $\frac{I}{I_{\text{prim}}} \approx 1.1$, corresponding to a direct electron emission yield of $\Gamma_{\text{dir}} = -0.1$, while for the other energies a direct electron emission yield of $\Gamma_{\text{dir}} \approx 0$ (corresponding to a detected current of the magnitude I_{prim}) is observed.

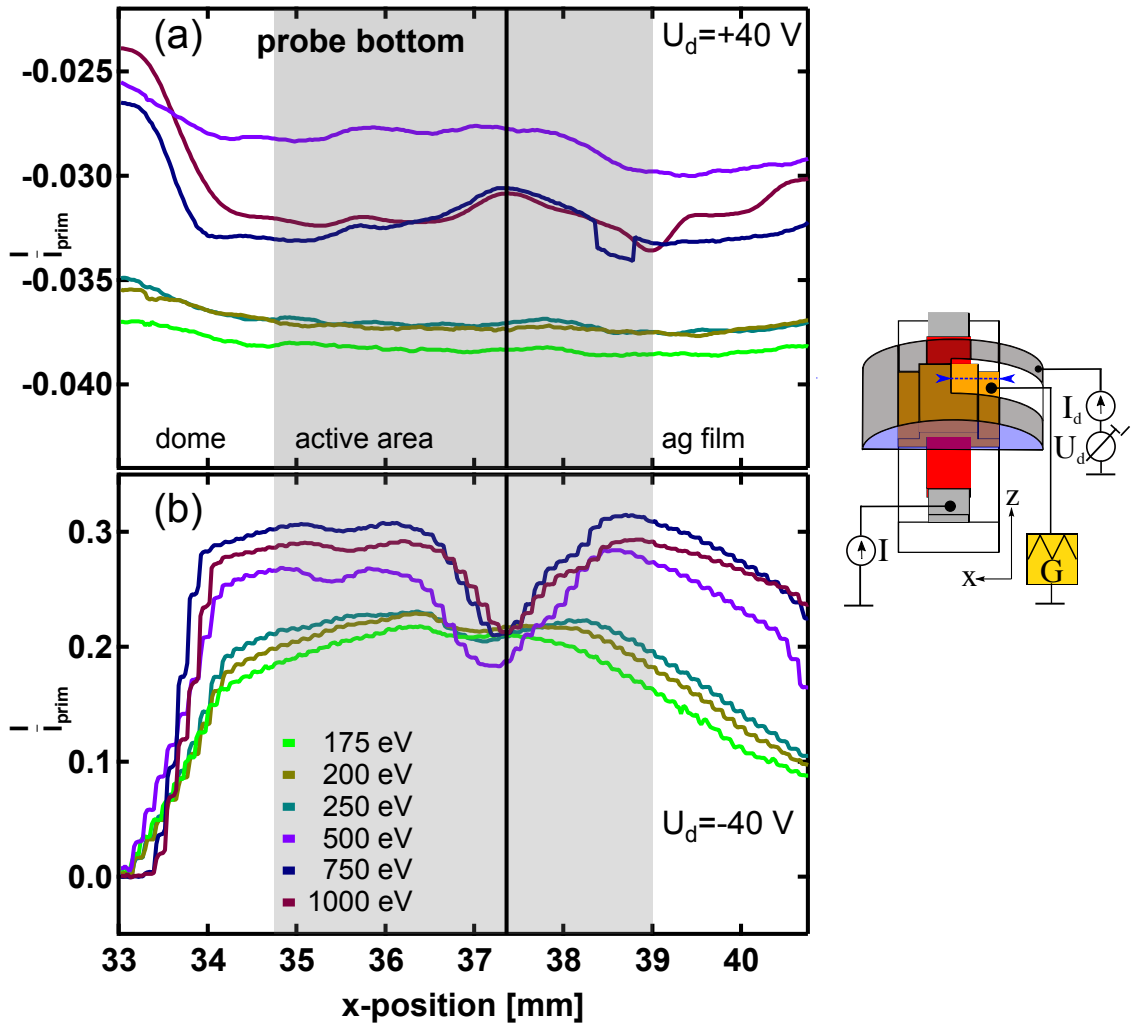


Figure 8.3: (a): Current in the *probe bottom* mode measured in the aluminum electrode normalized to the primary current as function of the x -position scanning across the active area for $U_d = +40$ V for different kinetic energies. The black line indicates the x -position at which the z -scans were performed. (b): Like in (a) but with $U_d = -40$ V. See also in [14].

The measurements were repeated in *probe bottom* mode as shown in figure 8.3; panel (a) contains results for $U_d = +40$ V, panel (b) for $U_d = -40$ V. Since the silver electrode is irradiated throughout the scan, while the current was measured in *probe bottom* mode, these are *indirect* experiments. For $U_d = +40$ V, the measured currents are negative in

all cases, corresponding to a net flow of electrons from the bottom aluminum to the top silver electrode. If primary electrons would directly penetrate the aluminum electrode, the current would be positive, which is unlikely, as discussed in section 7.8.

To explain the appearance of such small currents, one has to keep in mind that the *internal* current consist of contributions from electrons and -with opposing sign- of holes and these contributions are superimposed during the measurement process (see equation 6.3). Therefore a negative normalized current as detected in this *indirect* experiment corresponds to a distortion of the equipartition, where the hole contribution predominates, which was also previously observed in MIM experiments, when the modification of the bias voltage between top and bottom electrode of the MIM leads in some case to a complete annihilation of the internal current [12] and see section 8.2.4. The appearance of a negative current over the whole x -range of the scan (see panel (a) of figure 8.3) is somehow surprising on the first glance, since for $x < 33$ mm the external electrode instead of the sample is irradiated. As discussed before, the negative sign of the measured current points to an emission of electrons from the oxide covered aluminum electrode, since an absorption of negative charge carriers would cause a positive current signal. This signal is therefore attributed to the irradiation of the oxide covered aluminum electrode by the wings of the primary electron beam, which causes the negative sign of the measured current due to the high secondary electron emission yield of the oxide covered aluminum.

The transition from the irradiation of the external electrode towards the MIM's silver top electrode is indicated by a change in the current signal, which is visible at $x \approx 34$ mm in panel (a) of 8.3. Apparently, there is no difference in the measured currents between irradiation of the silver film within and without the active area.

Like observed in panels (a) of figures 8.2 and of 8.3, the resulting currents for energies below 250 eV are very close to each other, while for energies of 500 eV and above an energy dependence is visible. Since the positive voltage applied to the external electrode drains secondary electrons to the collector and hinders them to be reflected towards the sample and since the external electrode is no source of (low-energetic) electrons in this case, the measured currents in *probe bottom* mode for $U_d = +40$ V are the true *internal* currents.

However, the measured (normalized) currents are very small in comparison to similar experiments without external electrode as shown in panel (b) of figure 7.3, where for all energies values of $\frac{I}{I_{\text{prim}}} = +0.12$ were observed. This also indicates, that the measured currents without external field above the sample are influenced by re-/cross-absorption processes.

The results of x -scans in probe bottom mode at $U_d = -40$ V as shown in panel (b) of figure 8.3 show in principle a similar behaviour as observed without external electrode as shown in figure 7.3, although the measured current values with external field are about twice of the value without external field above the sample. The linear increase observed for $33 \text{ mm} < x < 34 \text{ mm}$ in panel (b) of figure 8.3 is caused by the primary electron beam leaving the external electrode towards the sample, while the increase observed in panel (b) of figure 7.3 was caused by the approach of the impact point of the primary beam to the active area. The linear decrease observed for $x > 39$ mm in panel (b) of figure 8.3

and for $x > 35$ mm in panel (b) of figure 7.3 is in both cases caused by the increasing distance between impact point and active area. For kinetic impact energies below 500 eV, no pronounced energy dependence is observed in panel (b) of figure 8.3 and the carbon contaminated area does not play a special role, while the measured currents for kinetic energies of 500 eV and above show both an energy dependence and a local extremum at the carbon contaminated area. For irradiation within this contaminated area, the energy dependence is almost negligible. The detected currents are positive in all cases and reach values of $\frac{I}{I_{\text{prim}}} \approx 0.2$ for low and of about $\frac{I}{I_{\text{prim}}} \approx 0.3$ for high kinetic impact energies, indicating a flux of electrons into the bottom aluminum electrode.

With a more detailed comparison between the data presented in panel (b) of figure 8.3 and in panels (a) of figures 8.1 and 8.2, one finds that

- the effective emission current into the aluminum bottom electrode increases with increasing impact energy from $\Gamma_{\text{indir}} \approx 0.18$ at 175 eV electrons to $\Gamma_{\text{indir}} = 0.31$ at 750 eV electrons (according to an analysis of the data in panel (b) at $x \approx 35.5$ mm). This is the opposite effect to the external electron emission into the vacuum (panel (a) of figure 8.2), where an increase of the electron energy caused a reduction in the total electron emission from the irradiated silver surface.
- The electron emission from the silver top electrode into the vacuum shows a monotonous decrease with increasing electron energy, whereas the effective current into the aluminum bottom electrode shows a maximum at 750 eV energy and decreases again at 1000 eV.

A detailed conclusive discussion of these results together with those of the in z -scans presented in section 8.1.3 will be given in section 9.1.

8.1.3 z -scans for different kinetic impact energies

Scans in z -direction have been performed at a fixed value of $x = 37.5$ mm (corresponding to a position in the middle of the aluminum electrode) to compare the impact on silver with the impact on oxide covered aluminum, to further study the emission behaviour of the oxide covered aluminum and to determine the z -coordinates of the active area. The results in *probe top* mode are shown in figure 8.4, the results obtained in *probe bottom* mode in figure 8.5. For $z < 146$ mm and for $z > 150.5$ mm, the external electrode is irradiated, the active area is irradiated for $146 \text{ mm} > z < 149$ mm and the oxide covered aluminum for $149 \text{ mm} > z < 150.5$ mm. Therefore, the change of the measured current signals at $z = 146$ mm and at $z = 150.5$ mm is caused by the fact that the primary electron beam enters and leaves the external electrode, respectively, at these impact points of the primary beam. In contrast to this, a change of the measured current signals at $z = 149$ mm is caused by the change in the nature of the experiment, as already discussed in section 7.1.3: In *probe top* mode, the experiment changes from a *direct* experiment, if the active area is irradiated, to an *indirect* experiment, if the oxide covered aluminum is irradiated; in the *probe bottom* mode, the situation is inverse.

As visible in panel (a) of figure 8.4 for irradiation of the active area at $U_d = +40$ V, the measured current signal reaches negative values for all kinetic energies and shows a pronounced peak for higher kinetic impact energies at the carbon contaminated spot at $z = 147.5$ mm. The behaviour is in good agreement with the one observed in panel (a) of figure 8.2. The measured current is $\frac{I}{I_{\text{prim}}} \approx 0$, if the oxide covered aluminum is irradiated instead, which is in good agreement with the results for irradiation of the glass substrate as shown in panel (a) of figure 8.1.

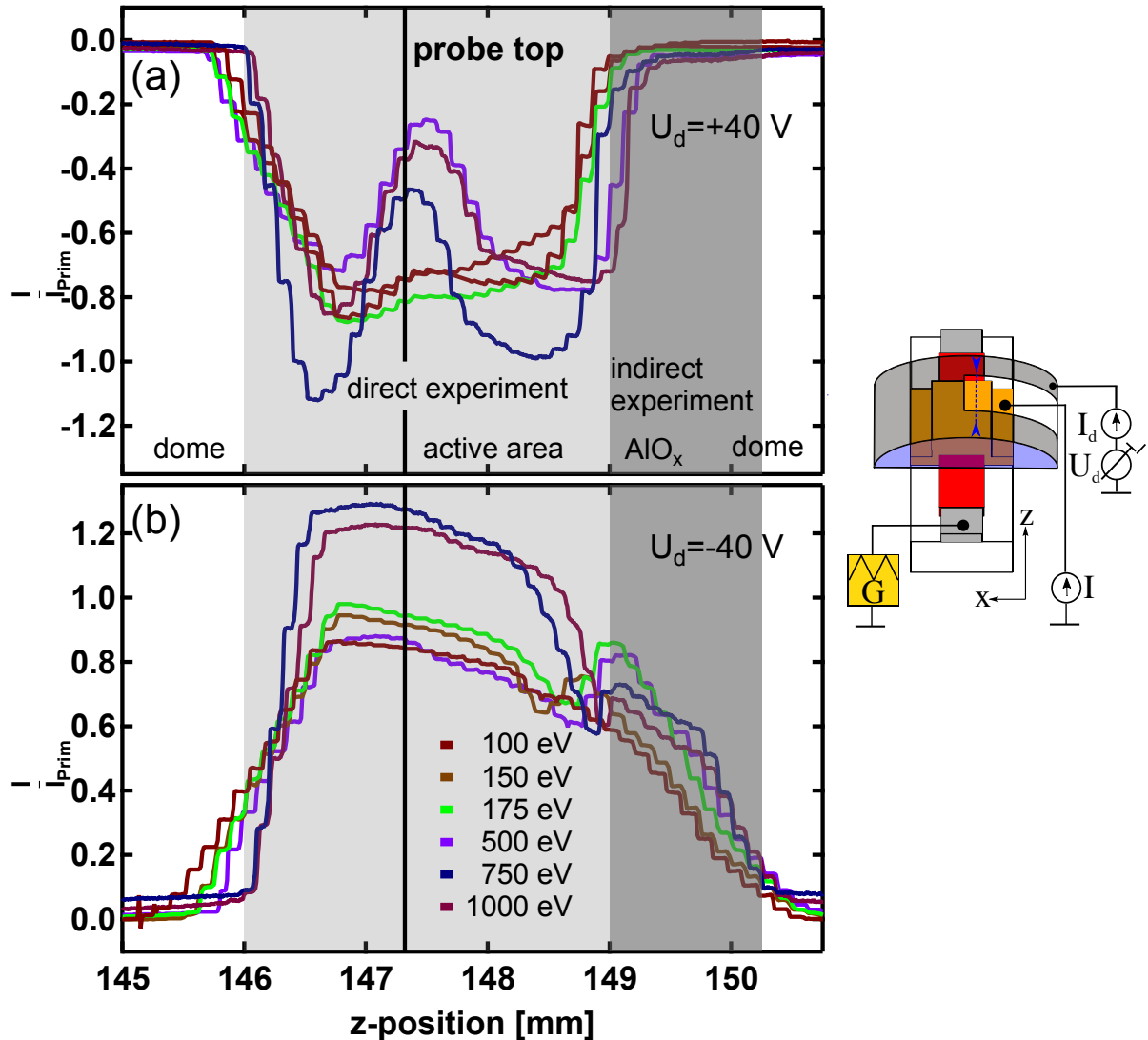


Figure 8.4: (a): Normalized current measured in *probe top* mode with positive collector/repeller voltage $U_d = +40$ V as a function of the z -position while scanning the primary electron beam at different kinetic energies across the active area. (b): Same as (a) but for $U_d = -40$ V. The black vertical line at $z \approx 147.2$ mm in panels (a) and (b) indicates the z -position, at which the x -scans were performed. See also in [14].

As visible in panel (b) of figure 8.4 for irradiation of the active area at $U_d = -40$ V, the measured current signal reaches positive values for all kinetic energies, while the carbon contaminated spot does not seem to play a special role, which is in line with the experimental findings observed in panel (b) of figure 8.2, but unlike to the plateau values there, the signal measured during the z -scans decreases with increasing z -values. The measured current reaches positive values and shows a linear decrease with increasing z -value, if the oxide covered aluminum is irradiated instead. A similar behavior was observed in curve (1) in panel (b) of figure 8.1 at $x \approx 39$ mm.

However, an influence of the inhomogeneity of the external electric field due to the slit in the external electrode may be the reason for the observed decreasing tendency by going from low to high z -values for irradiation of the active area in *probe top* mode at $U_d = -40$ V. As shown in section 11, the emission area of secondary electrons from the sample and the area to which they are reflected by the external field are not identical. So it seems plausible, that a part of the secondary electrons emitted from the top silver electrode is reflected towards the oxide covered aluminum or might leave the enclosed volume surrounded by the external electrode through the slit.

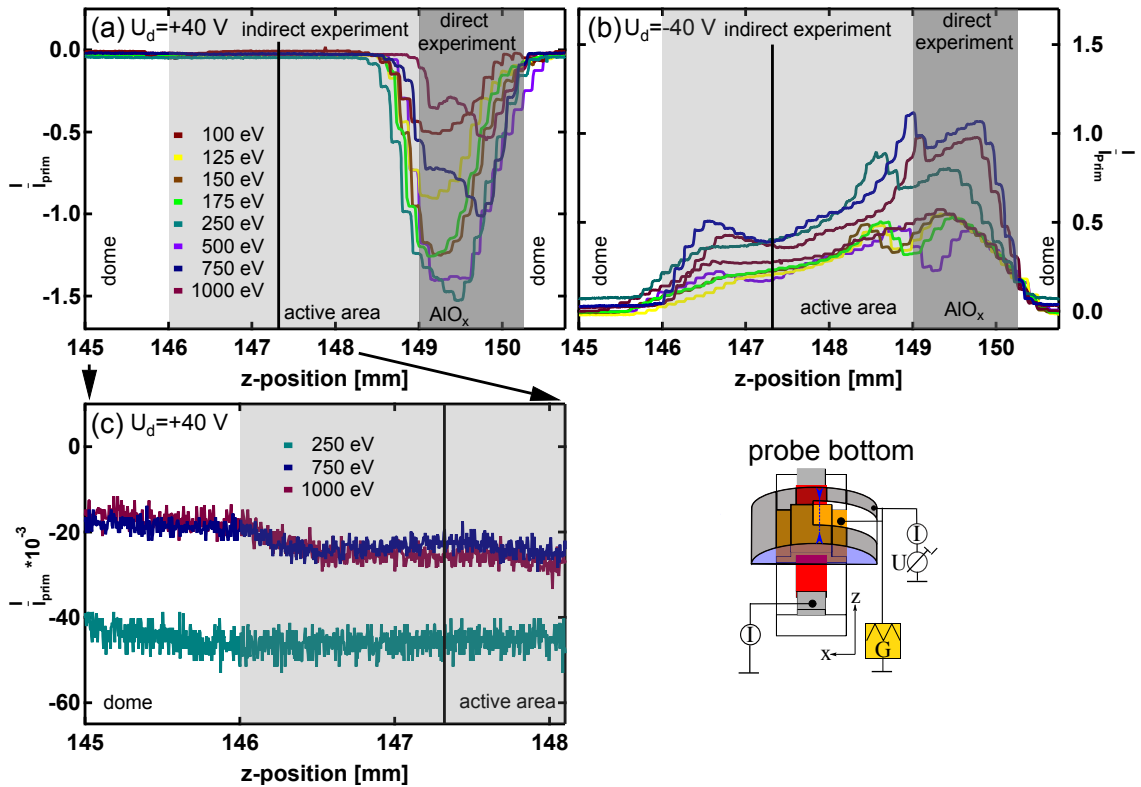


Figure 8.5: (a): Normalized current measured in *probe bottom* mode with positive collector/repeller voltage $U_d = +40$ V as a function of the z -position while scanning the primary electron beam at different kinetic energies across the active area. (b): Enlarged view of panel (a) for $145 \text{ mm} \leq z \leq 148 \text{ mm}$. (c): Same as (a) but for $U_d = -40$ V. The black line at $z \approx 147.2$ mm in panels (a) and (c) indicates the z -position at which the x -scans were performed.

If the active area is irradiated in *probe bottom* mode at $U_d = +40$ V, as shown in panel (a) of figure 8.5, this is an *indirect* experiment. As also visible in panel (a) of figure 8.3, the detection of small negative current values is expectable. A zoom of the z -interval from 145..148 mm is shown in panel (c) of figure 8.5. As seen there, the measured currents are indeed negative, even if the external electrode is irradiated instead of the sample, which is found to be in good agreement to the results shown in panel (a) of figure 8.3. If the oxide covered aluminum is irradiated instead (indicated by the dark-grey box in panel (a) of figure 8.5), this is a *direct* experiment showing negative normalized currents for all energies and a pronounced dependence on the primary impact energy. As described during the discussion of the preceding figure, no pronounced plateau is visible. In case of $U_d = -40$ V, as shown in panel (b) of figure 8.5, the measured currents are positive in all cases. A pronounced difference between irradiation of the active area and the oxide covered aluminum is visible. In principle, the observed behaviour for irradiation of the active area is very similar to the behaviour shown in panel (b) of figure 8.3, although the plateau structure is disturbed by the pronounced cross-absorption process and the inhomogeneity of the external field. The irradiation of the oxide covered aluminum (indicated by the dark-grey box) is again a *direct* experiment showing a pronounced dependence on the primary impact energy.

8.1.4 Cross-absorption currents in indirect experiments

The results obtained within the x -scans for irradiation of the active area are evaluated to calculate *direct* as well as *indirect* emission yields as function of the primary impact energy. The *direct* yield Γ_{dir}^+ is calculated using equation 6.5 from the results obtained by direct experiments, i.e. irradiation of the active area in *probe top* mode at $U_d = +40$ V as shown in panel (a) of figure 8.2. In the same way but using results recorded at $U_d = -40$ V as shown in panel (b) of figure 8.2, Γ_{dir}^- is calculated. The *indirect* emission yields Γ_{indir}^+ and Γ_{indir}^- are calculated using equation 6.6 and the results of panels (a) and (b) of figure 8.3. In all cases the evaluation was performed outside the carbon contaminated area. These yields as function of the primary impact energy are shown in the panels (a)-(d) of figure 8.6.

Γ_{dir} describes the net number of negative charge carriers *leaving* the irradiated electrode per impinging primary electron. In case $\Gamma_{\text{dir}} > 0$, more electrons leave the irradiated electrode than impinge on it; in case $\Gamma_{\text{dir}} < 0$, more electrons impinge on the irradiated electrode than leave it. For $\Gamma_{\text{dir}} = 0$, impact and emission are in equipartition.

Γ_{indir} describes the net number of negative charge carriers *entering* the non-irradiated electrode per impinging primary electron. This *indirect* yield actually describes the internal current I_{internal} normalized to the primary electron current I_{prim} and has, according to equation 6.2, contributions from electron- and hole-currents with opposite sign. Therefore $\Gamma_{\text{indir}} > 0$ indicates a predominating electron-current, $\Gamma_{\text{indir}} = 0$ an equipartition between electron- and hole-current and $\Gamma_{\text{indir}} < 0$ a predominating hole current.

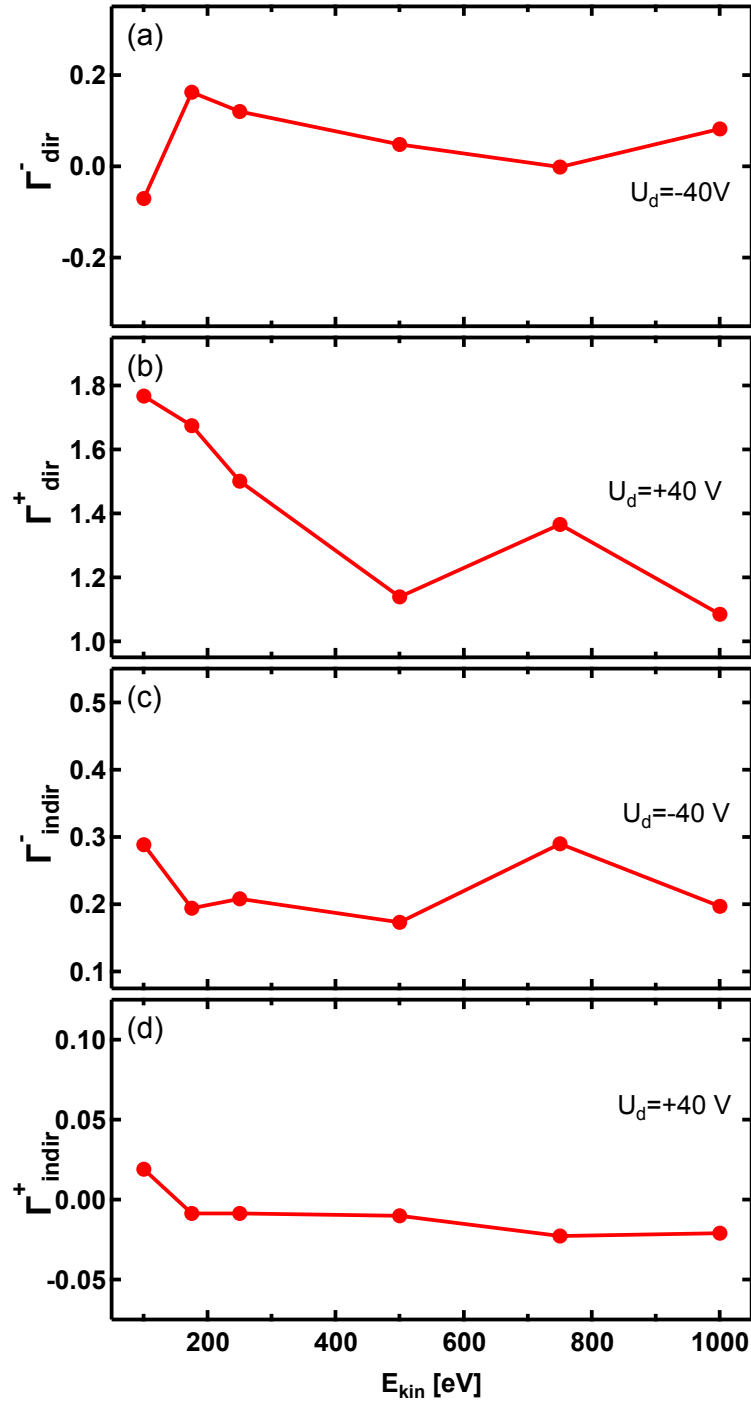


Figure 8.6: *Direct* and *indirect* emission yield calculated from the current measured in the irradiated silver electrode (*direct* experiments) (panels (a)-(b)) and in the underlying, non-irradiated aluminum electrode (*indirect* experiments) (panels (c)-(d)) measured during irradiation of a MIM's active area for positive and negative collector/repeller voltages, respectively. All current values were normalized to the primary electron current I_{prim} . See also in [14].

As depicted in panel (a) of figure 8.6, the direct yield Γ_{dir}^- remains slightly positive for all energies above 150 eV, indicating that about 10..20% more electrons are emitted from the irradiated surface than impinge on it. This can be easily understood, since the external field repels (low-energy) electrons emitted from the irradiated surface back towards the surface and the external electrode is simultaneously a source of electrons accelerated towards the sample.

As depicted in panel (b) of same figure, the direct yield Γ_{dir}^+ remains above 1 for all energies and shows a strong dependence on the primary impact energy. Since emitted electrons are drained towards the external electrode, which is no source of (low-energetic) electrons at the applied $U_d = +40$ V, the value for Γ_{dir}^+ is equal to the total external emission yield ζ ; values between $\zeta = 1.8$ for the lowest and of $\zeta \approx 1.1$ for the highest primary impact energy are determined.

As depicted in panel (c) of same figure, the indirect yield Γ_{indir}^- remains positive for all energies and shows, apart from the statistical scatter, no pronounced dependence on the primary impact energy. About 20..30% of the primary electron current I_{prim} are detected as flux of electrons into the aluminum bottom electrode. Like shown in equation 6.17, the detected current may consist of contributions crossing the internal barrier as well as of contributions circumventing it by (cross-) absorption processes. The corresponding yield at $U_d = +40$ V, Γ_{indir}^+ , probes the current as defined by equation 6.11 on page 47 and is therefore *independent* from (cross-) absorption processes, which are suppressed due to the external field. The negative values for Γ_{indir}^+ indicate, that the internal current is slightly predominated by the transport of holes.

Assuming a full contribution of the reabsorption current I_{reabs} to Γ_{indir}^- through the repelling of secondary electrons along with electrons emitted from the external electrode, and assuming a total inhibition of the reabsorption in case of Γ_{indir}^+ through the positive external field, the magnitude of the cross-absorption current can be determined using equation 6.21 and the values for Γ_{indir}^+ and Γ_{indir}^- as shown in panels (c) and (d) of figure 8.6.

This way, the current I_{abs} normalized to the primary electron current I_{prim} can be determined, which is of particular interest, since this cross-absorption process of electrons emitted from the irradiated surface and externally circumventing the internal barrier significantly modifies the detected apparent "internal" device current, as discussed in section 7.8.

As will be shown in the following section 8.1.5 in figure 8.13, an electric field caused by the application of a voltage $U_d = +40$ V is sufficient to fully suppress a contribution of electrons reflected towards the sample, while for $U_d = -40$ V the reflection process is fully activated.

Using the current I_{abs} as discussed above, a cross-absorption yield Γ_{abs} as the ratio $\frac{I_{\text{abs}}}{I_{\text{prim}}}$ can be defined.

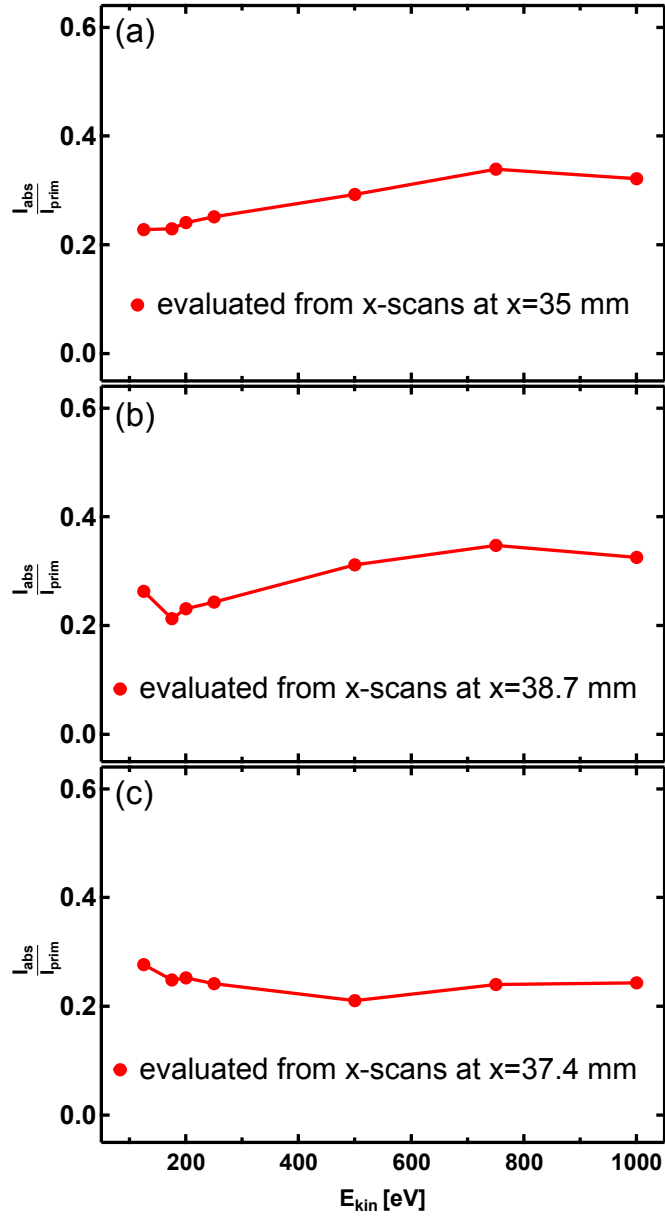


Figure 8.7: **(a)**: Cross-absorption yield, i.e., cross-absorption current calculated using equation 6.21 normalized to the primary electron current, measured under irradiation of the top silver surface at three different spots of the active MIM junction area: (a) the clean silver surface at $x = 35$ mm on one edge of the active area; (b): the clean silver surface at $x = 38.7$ mm on the other edge of the active area; (c): the carbon contaminated spot in the center of the active area ($x = 37.4$ mm). See also in [14].

This cross-absorption yield was evaluated for irradiation of three different positions as shown in figure 8.7: Panel (a) contains the data evaluated from x -scans in *probe bottom* mode at $x = 35$ mm (on the active area left to the carbon contaminated spot), panel (b) as in (a) for $x = 38.7$ mm (on the active area right to the carbon contaminated spot), panel

(c) like in (a) and (b) but within carbon contaminated spot at $x = 37.4$ mm. As visible in the figure, the curves in panels (a) and (b) show (about) the same weak dependence on the primary impact energy, 20..30% of the primary electron current are circumventing the internal oxide barrier, which explains well the high apparently "internal" device currents as observed in panels (b) of figures 7.5, 7.14 and 8.3. In panel (c), for irradiation of the carbon contaminated spot, the energy dependence is negligible and about 22% of the primary electron current is circumventing the internal barrier.

This finding means, that the cross absorption yield Γ_{abs} slightly increases with increasing primary kinetic energy. Since Γ_{abs} is expected to scale with the secondary electron yield δ , it would be interesting to determine the value for δ from the experimental results discussed here. Unfortunately, the influence of tertiary electrons emitted from the external electrode towards the sample is high, so that the current measured on the external electrode strongly depends on the emission behaviour of the external electrode. As a consequence of this, the determination of δ as proposed by Schou [15] from the currents measured on the external electrode at positive and negative voltage applied, respectively, becomes impossible and only the total emission yield ζ can be determined from the data presented here. Literature data as shown in panel (a) of figure 7.6 indicate an increase of δ with increasing energy (up to 1 keV), which is in line with the the increase of Γ_{abs} as shown in figure 8.7.

8.1.5 Dependence of the direct emission yield Γ_{dir} and the indirect emission yield Γ_{indir} on the impact angle

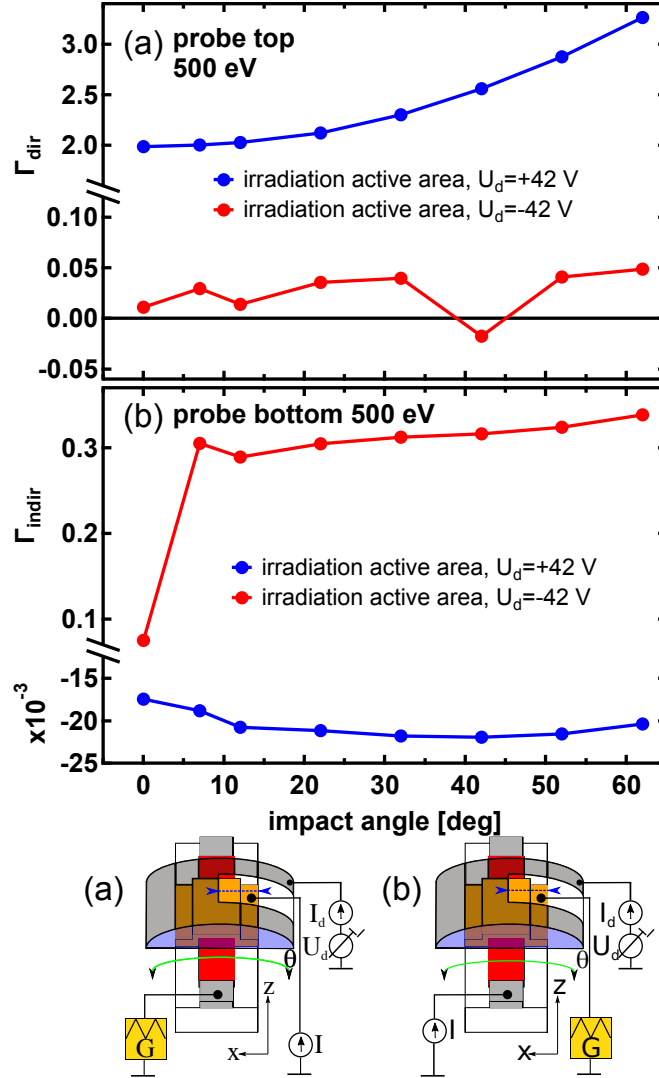


Figure 8.8: (a): Γ_{dir} as function of the impact angle (relative to surface normal) obtained from x -scans in *probe top* mode at 500 eV primary impact energy for $U_d = \pm 40$ V. (b): like (a) but Γ_{indir} obtained from *probe bottom* experiments.

The impact angle dependence was studied by performing x -scans to avoid a beam walk-off from the sample as discussed in section 7.5. These scans were performed at a primary impact energy of 500 eV in *probe top* and *probe bottom* mode at $U_d = \pm 40$ V for different impact angles (relative to the surface normal). The current (normalized) to the primary electron current I_{prim} was read out from the plateaus and using the formulae 6.5 and 6.6, the *direct* as well as the *indirect* yields were calculated.

As shown in section 7.5 (also see [13]), Γ_{dir} without external field was found to increase with increasing impact angle, while Γ_{indir} without external field was observed to be independent

from the impact angle. The results for Γ_{dir} in case of $U_d = +40$ V show a clear increase with increasing impact angle (relative to surface normal), while Γ_{dir} in case of $U_d = -40$ V only shows a slight increase. This slight increase is also found in the corresponding measurement for Γ_{indir} in case of $U_d = -40$ V after an initial jump when the primary electron beam is steered away from normal incidence. The observed jump of Γ_{indir} in case of $U_d = -40$ V may be interpreted in terms of a total repelling of secondary electrons towards the active area at an impact angle of 0° , while for impact angles different from normal incidence, a part of the electrons emitted from the sample is reflected to different areas so that the re-absorption current decreases. Γ_{indir} in case of $U_d = +40$ V shows a slight *decrease* with increasing impact angle and is slightly negative for all impact angles. As explained above, in case of $U_d = +40$ V, secondary electrons are drained towards the external electrode and the emission from this external electrode towards the sample is suppressed, so that the measurement for Γ_{indir} in this case truly reflects the *internal* device current within the MIM system, while the measurement of Γ_{indir} in case of $U_d = -40$ V is superimposed by re- and cross-absorption processes.

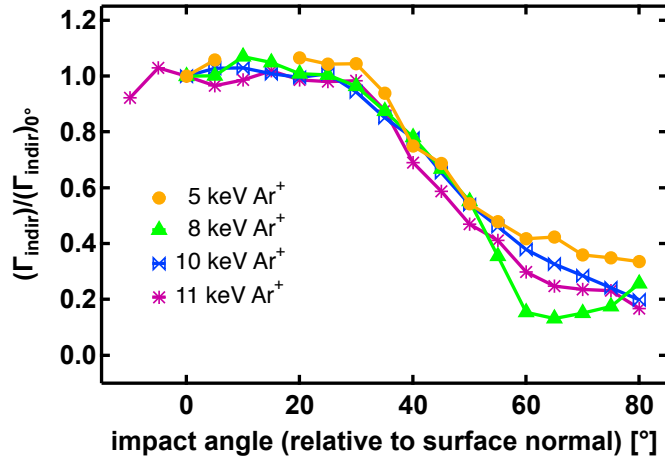


Figure 8.9: (a): Γ_{MIM} normalized to the signal obtained for normal incidence as function of the impact angle (relative to surface normal) obtained from measurements on similar MIM devices under irradiation with Ar^+ -ions for different kinetic impact energies without external electrode. Reproduced from [46, 57].

As also mentioned in section 7.5, in case of Ar^+ -bombardment of similar MIM samples [83, 84, 57], qualitatively also a *decrease* of the *internal* MIM device current with increasing impact angle (also measured relative to surface normal) was observed, although the shape of the curve was fundamentally different in this case, as shown in figure 8.9. The measured yield is identically defined like the yield Γ_{indir} , since the experiments under argon irradiation were performed in *probe bottom* mode without external electric fields. The decrease of the internal current with increasing impact angle in case of Ar^+ -bombardment was interpreted in terms of a reduced penetration depth of the projectile and therefore a generation of excited charge carriers farther away from the oxide barrier, causing the decrease in the internal current.

8.2 Signal dependence as function of external collector/repeller voltage

By varying the voltage U_d applied to the external electrode, the external field above the sample is modified. As result of the previously discussed x - and z -scans, the position of the active area is known. With this knowledge, a fixed x - y - z -position was chosen representing an irradiation spot within the active area, allowing to determine the influence of the *external* field to the measured currents discussed in terms of Γ_{dir} and Γ_{indir} . The dependence of Γ_{dir} on the external field probes the energy of emitted electrons. A saturation in case of $U_d > 0$ V indicates, that all available emitted electrons are drained towards the external electrode, while a saturation in case of $U_d < 0$ V indicates, that all emitted electrons are repelled towards the sample.

8.2.1 Direct emission yield Γ_{dir} as function of the external field

The *direct* emission yield Γ_{dir} was measured for a fixed irradiation position on the active area as function of the voltage U_d applied to the external electrode (solid lines in figure 8.10) for different kinetic impact energies along with the corresponding current I_d measured on the external electrode (indicated as dotted lines in figure 8.10). In all panels of figure 8.10, a strong dependence on the external field for voltages ≈ -15 V $< U_d < \approx +7$ V is observed, while for U_d below -15 V or above $+7$ V, a saturation of Γ_{dir} as well as of I_d occurs.

In case of 100 eV (panel (a) of figure 8.10), both measured currents are almost identical, while for higher kinetic energies especially for $U_d < -15$ V a clear difference is observed. As discussed above, the external electrode is no source of low-energetic electrons in case of sufficiently high values $U_d > 0$ V, but emits electrons towards the sample in case of sufficient low values for $U_d < 0$ V. On the other hand, reabsorption and cross-absorption processes are suppressed in case sufficiently high positive values of U_d , since all electrons are drained towards the external electrode. This indicates, that the information obtained from the measurement of Γ_{dir} on the sample on the one hand and the measurement of I_d on the external electrode on the other hand contain the identical information in case that U_d is high enough. The observed difference in case of negative values for U_d is thereby caused by the emission of electrons from the external electrode towards the sample. While all electrons emitted from the sample reach the external electrode in case $U_d > 0$ V, electrons emitted from from the external electrode may also hit the glass substrate or the non-irradiated film of the sample.

The values obtained for $U_d = 0$ V are comparable to the values determined without external field, but obviously, even a small electric field above the sample will significantly alter the results. The small remaining slopes of the measured curves for low and high values of U_d prove, that the majority of electrons is either reflected from or drained towards external electrode, so that a further increase of the field strength would not change the results.

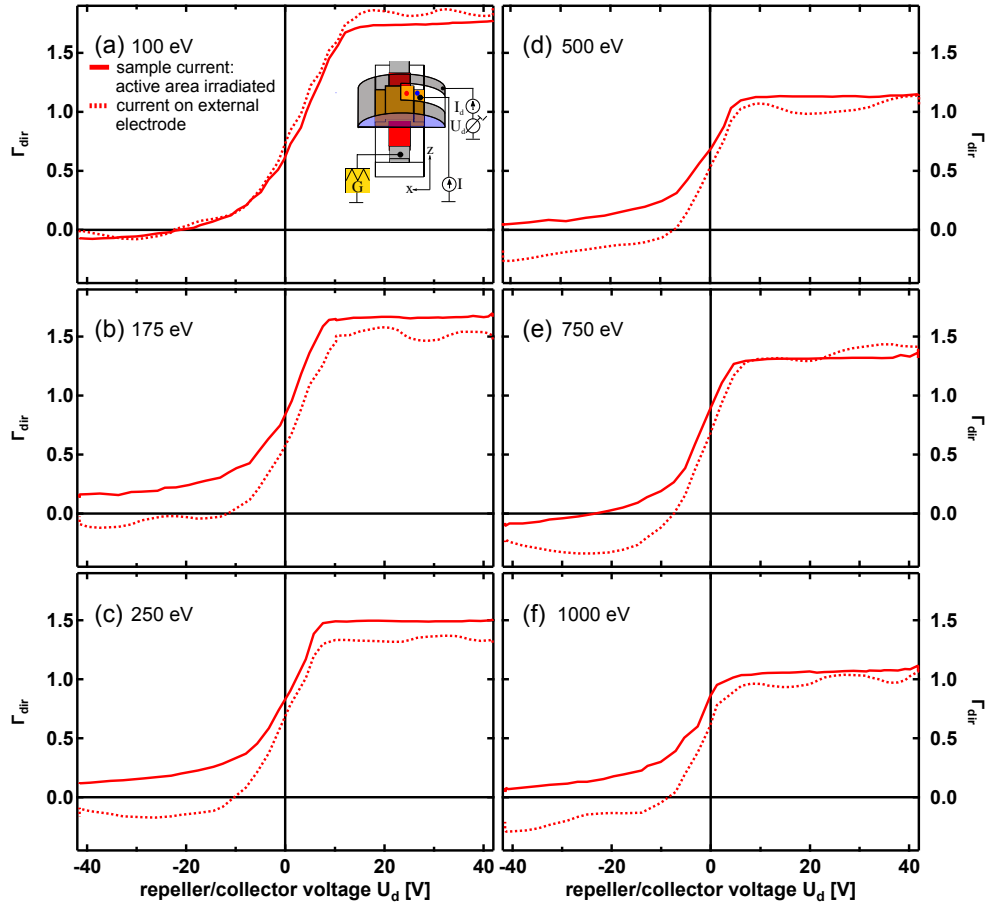


Figure 8.10: **Solid lines:** Γ_{dir} obtained from measurements of the current into the irradiated top electrode for irradiation of the active area as function of voltage U_d applied to external electrode for different kinetic impact energies. **Dashed lines:** Current I_d measured simultaneously to sample current on the external electrode. See also in [14].

In addition to the measurements for irradiation of the active area as shown in figure 8.10, measurements on the silver film outside the active area are shown in figure 8.11. While the values for negative U_d are very similar in both cases, the yields determined for positive U_d differ significantly. Since the irradiated position for measurements on the silver lies far outside the active area, the electric field may change significantly and more electrons emitted from the silver film may leave the area controlled by the electric field through the entrance slit. The leaving of electrons through the slit causes most likely the observed difference between measured sample-current and measured I_d as visible in figure 8.11 for $U_d > 0$ V. The reason why the observed sample currents differ between measurements on the active area and on the silver film remains unclear at this point.

An additional way to obtain results from *direct* experiments is the irradiation of the oxide covered aluminum while measuring the current in *probe bottom* mode, as shown in figure 8.12.

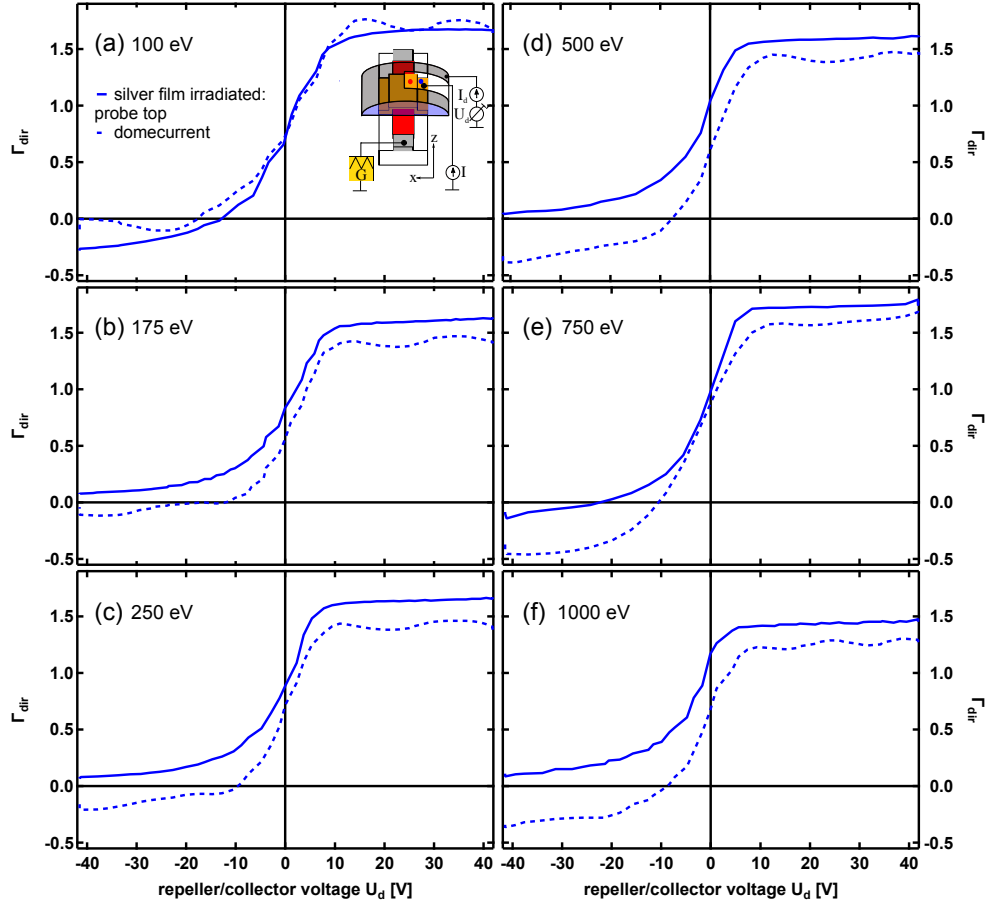


Figure 8.11: **Solid lines:** Γ_{dir} obtained from measurements of the current into the irradiated top electrode for irradiation of the silver film outside the active area as function of voltage U_d applied to external electrode for different kinetic impact energies. **Dashed lines:** Current I_d measured simultaneously to sample current on the external electrode.

In case of measurements on the oxide covered aluminum for negative values of U_d , an even more pronounced difference between measurements on the sample and on the external electrode is observed, along with a clear plateau. In case of $U_d > 0$ V, the obtained results are practically identical, but a non-negligible slope indicates, that the external electric field is not strong enough to fully attract all electrons emitted from the sample.

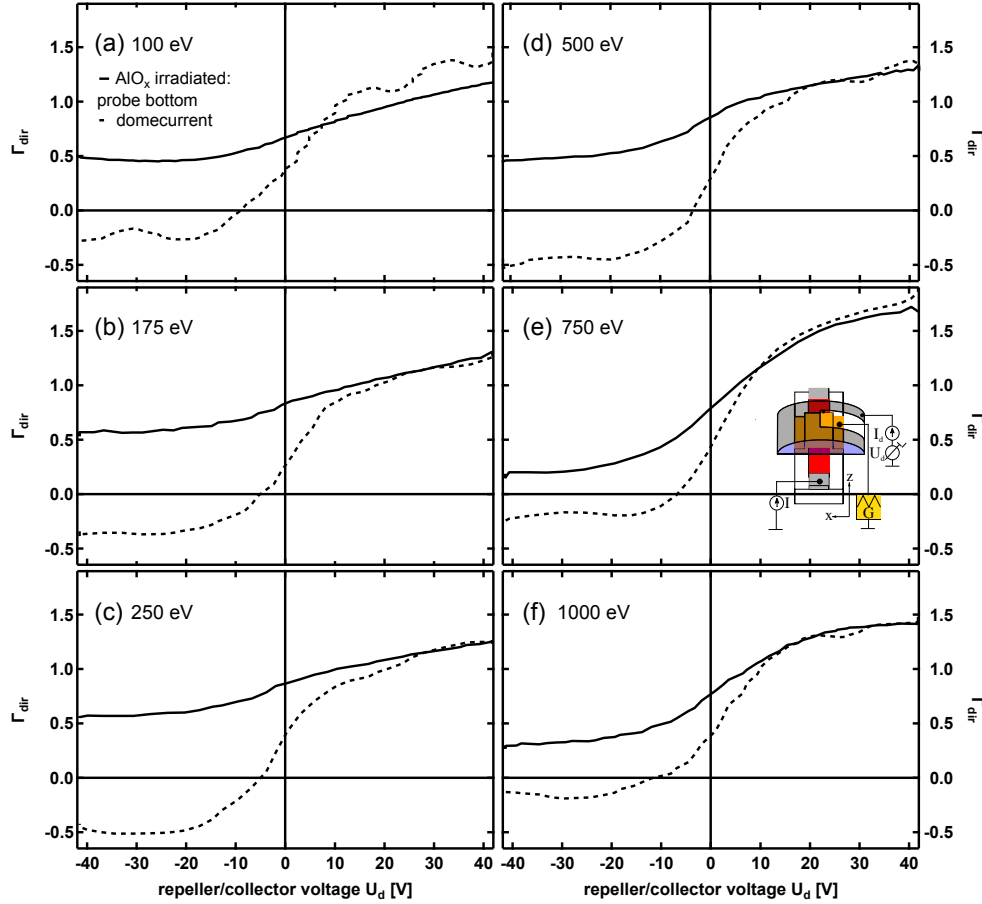


Figure 8.12: **Solid lines:** Γ_{dir} obtained from measurements of the current into the irradiated bottom electrode for irradiation of the oxide covered aluminum film as function of voltage U_d applied to external electrode for different kinetic impact energies. **Dashed lines:** Current I_d measured simultaneously to sample current on the external electrode.

8.2.2 Indirect emission yield Γ_{indir} as function of the external field

The dependence of the *indirect* emission yield Γ_{indir} on the external electric field is shown in 8.13 for different kinetic impact energies at three different impact positions, which coincide with the irradiated spots used before for the measurements in figures 8.10 for red curves, 8.11 for the blue curves and 8.12 for the black curves. Obviously, the dependence of the measured *indirect* emission yields is almost identical, since the curve shapes are very similar in all cases, although the obtained values for Γ_{indir} clearly depend on the irradiated area, especially in case of $U_d < -10$ V. In case of $U_d < -10$ V, electrons emitted from the irradiated sample surface as well as from the external electrode are repelled towards the sample and the measured values for Γ_{indir} are dominated by the normalized absorption current I_{abs} with contributions of both mentioned mechanisms. The very high values obtained for irradiation of the oxide covered aluminum in case of $U_d < -10$ V are

most likely a consequence of the high secondary electron emission yield of the sample in combination with the relatively large open surface area of the oxide covered aluminum on which electrons may impinge. The pronounced difference between measurements on the silver film within (red curves) and outside the active area (blue curves) can be assigned to the differences already observed in the *direct* experiments in figures 8.11 and 8.10. As already discussed in the preceding section, the reason for this difference is unclear and might be due to the leaving of electrons through the entrance slit of the external electrode or due to a inhomogeneity of the external field above the sample in the region of the entrance slit.

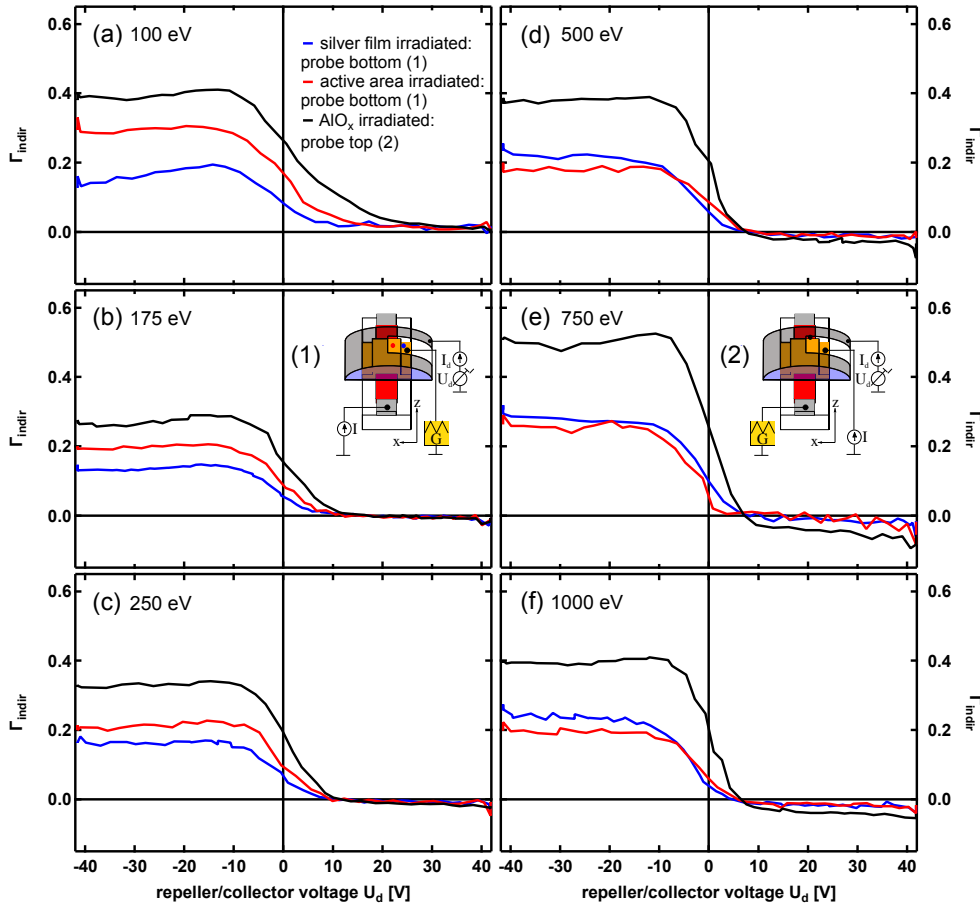


Figure 8.13: Overview of *indirect* experiments where the active area is irradiated while the current is measured in the *probe bottom* mode. Γ_{indir} is calculated by the formula 6.6 and shown as a function of the collector/repeller voltage U_d for different kinetic energies from 100 eV (a) to 1000 eV (c). Taken from [14].

In case of $U_d > +15$ V, the indirect emission yield Γ_{indir} becomes *independent* of the external electric field, which is interpreted as a full suppression of re-absorption and cross-absorption processes by the external field. Therefore, these measured currents truly represent currents *internally* transported across the barrier. This finding also justifies the fairly low collector/repeller voltages of ± 40 V, which are found to be sufficient to guarantee measurements with and without the influence of externally mediated processes.

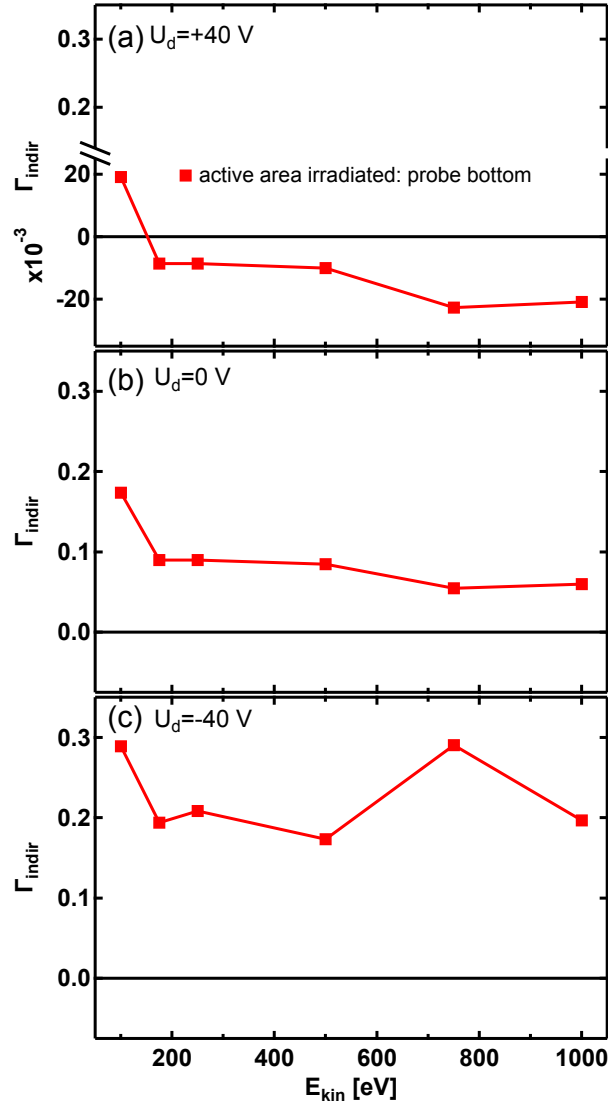


Figure 8.14: Evaluation of *indirect* experiments as a function of the kinetic energy for different collector/repeller voltages: +40 V in (a), 0 V in (b) and -40 V in (c). Taken from [14].

In figure 8.14, the energy dependence of the obtained results for irradiation of the active area as shown in figure 8.13 are evaluated in panel (a) for $U_d = +40$ V, in panel (b) for $U_d = 0$ V and in panel (c) for $U_d = -40$ V. The values obtained for $U_d = 0$ V are comparable to the results obtained in experiments without external field. This becomes obvious by comparing panel (b) of figure 8.14 with panel (b) of figure 7.5. The strong dependence of the measured values for Γ_{indir} for $U_d \approx 0$ V justifies the interpretation, that in case of measurements without external field a non-negligible part of the signal is actually caused by externally mediated processes. This is further supported by the fact, that the observed energy dependence as shown in panels (a) and (b) of figure 8.14 has almost the same curve shape, but the total values differ. As discussed above, in panel

(a) of the figure, the true *internal* (normalized) current is shown, which is negative in all cases except for the lowest kinetic impact energy, indicating a predominating hole-contribution to the measured current for the higher kinetic energies. As indicated in panel (b) of the same figure, the normalized current in case of $U_d = 0$ V is shifted to positive values, indicating a flux of electrons into the aluminum electrode, which is dominated by externally mediated processes. In panel (c) of the figure, the results for $U_d = -40$ V are shown, which corresponds to a complete repelling of the electrons emitted from the irradiated surface and plus impact of electrons emitted from the external electrode. These results are completely dominated by *external* transport effects.

8.2.3 Evaluation of the total emission yield ζ

Due to the significant emission of electrons from the external electrode towards the sample, the discrimination into η and δ as discussed in [15] is not possible here. Therefore also in case of experiments with external electrode only the *total emission yield* ζ can be extracted, which was already the case in experiments without external field as discussed in section 7.3 on page 64. As shown in equation 6.13 on page 47, ζ can be obtained by calculating the difference between I_{dir}^+ and I_{indir}^+ , both measured at $U_d = +40$ V. Alternatively, the current measured on the external electrode in case of $U_d = +40$ V can also be evaluated to determine ζ , which is discussed in equation 6.14 on page 47. Four different sets of data are available for this purpose:

- Data obtained in position dependent *direct* and *indirect* experiments at $U_d = +40$ V (x -scans in figures 8.2 and 8.3) evaluated via equation 4.1.
- Data obtained in position dependent *direct* and *indirect* experiments at $U_d = +40$ V (z -scans in figures 8.4 and 8.5) evaluated via equation 4.1. Since the results from z -scans are superimposed by field effects (as discussed in section 8.1.3), the data are not evaluated here.
- Data obtained in *direct* and *indirect* experiments at fixed x - y - z -position measured with variable collector/repeller voltage U_d (figures 8.10 and 8.13) evaluated via equation 4.1.
- Current measured on the external electrode in *direct* and *indirect* experiments at $U_d = +40$ V evaluated using equation 6.14.

In panel (a) of figure 8.15, results for the total emission yield ζ as function of the primary impact energy are shown as reported in the literature for irradiation of silver samples. This figure can also be found in similar form in panel (a) of 7.10, and is shown again here to allow a direct comparison of the literature data measured on silver samples with experimental findings of this work. As discussed above, the results from literature data were obtained by summing up results for δ and for η from [71, 72] and from [60]. In addition, results from x - and z -scans measured without external field (taken from figure 7.5, see also in [13]) and the results of simulations as discussed in chapter 7.2 are shown in the figure, which are in best agreement with measurements described within this thesis.

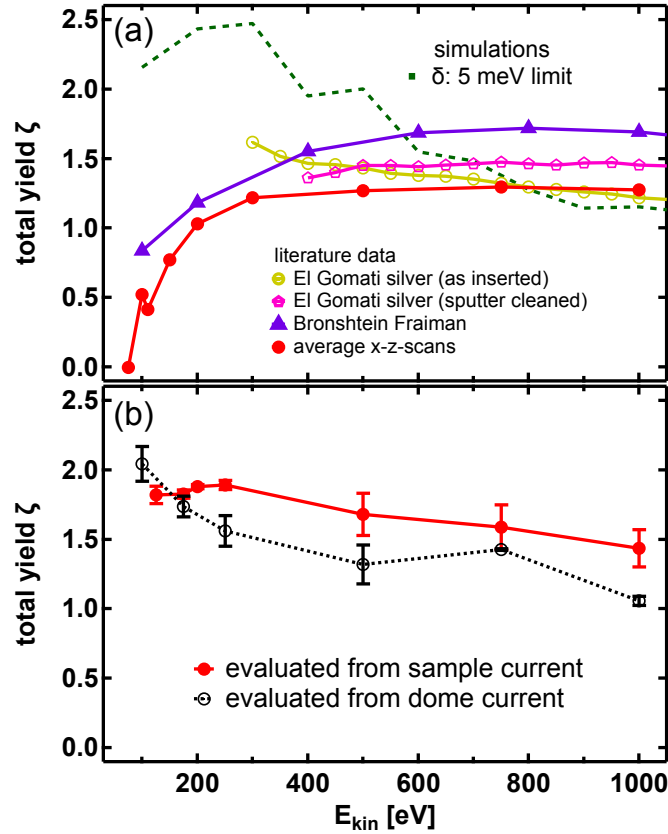


Figure 8.15: (a): Total emission yield ζ as a function of the kinetic electron impact energy during irradiation of a silver film as reported in the literature obtained by summing η and δ : El-Gomati from [71, 72], Bronshtein Fraiman from [60] and average of results from x - and z -scans (see figure 7.5 and [13]) along with results calculated using Casino Monte Carlo for modified settings (see figure 7.6 in chapter 7.2 and [20, 13]). (b): Results of experiments discussed within this thesis obtained by evaluating I_d^+ (black curve) and by evaluating the sample current using equation 4.1 (red curve), respectively. See also in [14].

The results obtained from x -scans for irradiation inside and outside the carbon contaminated region on the active area as shown in figures 8.2 and 8.3 for $U_d = +40$ V were evaluated using equation 4.1 and averaged, yielding in the red curve shown in panel (b) of figure 8.15. The black (dotted) line in the figure was obtained by averaging all results of measurements of the current into the external electrode for irradiation of the active area in case of $U_d = +40$ V.

The measured results for ζ as function of the kinetic impact energy as shown in panel (b) of figure 8.15 are in the same order of magnitude as observed in the literature data shown in panel (a) of the figure. In principle, also the trend of decreasing values with increasing impact energy as observed by El-Gomati and Walker and also as simulations using Casino (with modified setting) show, is observed in panel (b) of the figure. However, these results contradict the results obtained without external electrode (red curve in panel (a)) and the

results measured by Bronshtein and Fraiman, which both show a strong increase of ζ in the energy range from ≈ 100 eV to 300 eV and a fairly constant yield for energies above 300 eV.

Since the values obtained without external field above the surface were found to be influenced by externally mediated processes via re- and cross-absorption, the values shown in panel (b) of figure 8.15 seem to be more reliable.

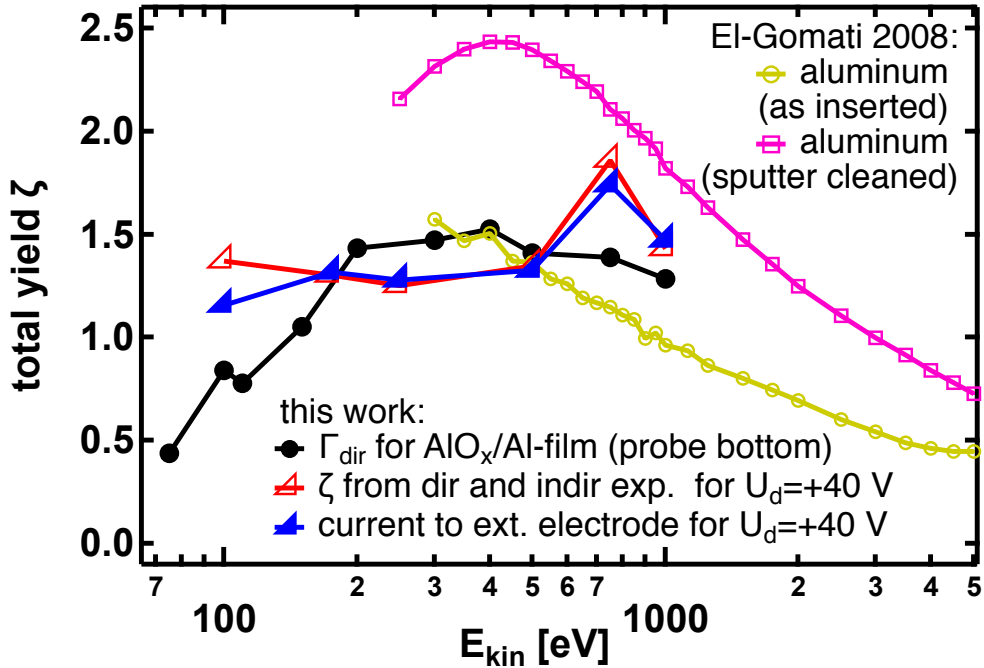


Figure 8.16: Total emission yield ζ as a function of the kinetic electron impact energy during irradiation of aluminum film as reported in the literature obtained by summing η and δ : El-Gomati from [71, 72], results from z-scans measured without external electrode (black curve) see section 7.1.3 (see also [13]) along with results evaluated from figures 8.12 and 8.13 evaluated using equation 4.1 (red curve) and with current measured onto the external electrode for irradiation of the oxide covered aluminum (blue curve).

The fact that yield obtained by evaluating the current on the external electrode underestimate the emission yield is most likely caused by the emission of elastically backscattered electrons from the external electrode towards the sample, which are not held back by the field above the sample. These elastically backscattered electrons may be emitted when high-energetic electrons are backscattered on the sample. When these backscattered electrons leave the surface of the external collector, the current measured on the collector is reduced.

The data shown in panel (b) of figure 7.11 on page 66 can be used to draw a comparison with results obtained from *direct* and *indirect* measurements at constant position and varied U_d as shown in figure 8.12 and 8.13. The results were evaluated using equation 4.1 and shown as function of the primary impact energy as red curve in figure 8.16 along

with the measured current onto the external electrode (shown as blue curve in the same figure). Also in this case, the obtained values have the correct order of magnitude but do not match the shown results.

8.2.4 Bias voltage dependence of Γ_{indir}

As already discussed in sections 7.6, the *internal* field caused by the application of a bias voltage between top and bottom electrode of the MIM influences the transport mechanisms for electrons and holes across the internal oxide barrier and therefore distort the equipartition of the electron- and hole-current. The influence of a bias voltage on the internal barrier is shown in figure 6.11 on page 36 in section 6.6. As discussed in section 7.6 in figure 7.18 on page 73, the bias voltage may also affect the re- and cross-absorption, since the potentials of the electrodes are shifted. Technically, the potentiostat applies a negative potential to the non-metered electrode in case a positive bias voltage is desired. In case of measurements in *probe bottom* mode, a *positive* bias voltage is therefore provided by the application of a *negative* potential to the MIM's top electrode and vice versa.

To remind the reader, the important facts are repeated here:

- The *internal* current consists of an electron and a hole contribution with opposite sign (see equation 6.3).
- The application of a bias voltage shifts the barrier by shifting the potential of the top silver electrode with respect to the potential of the bottom aluminum electrode.
- By chosen convention, a *negative* bias acts as retarding field for electrons and decreases the electron flux from the irradiated top towards the metered bottom electrode, while simultaneously the transport of holes is eased.
- A *positive* bias voltage acts as retarding field for holes, while the transport of electrons is eased.

As shown in figures 8.10 and in 8.13, the external field controlled by the voltage U_d applied to the external electrode has significant influence on the signals measured in *direct* and *indirect* experiments, respectively, which was explained in terms of externally mediated processes by re- and cross-absorption, which were found to be fully suppressed, when a sufficiently high voltage $U_d > +10$ V was applied to the external electrode. Therefore results obtained for these positive voltages U_d are of peculiar interest, since they are thought to represent the true *internal* current across the barrier. Unlike the experiments discussed in section 7.6, the bias voltage was applied as static voltage to cancel the influence of the dynamic capacity on the one hand and to allow the interpretation in terms of one variable, namely on the voltage U_d . All measurements were performed for 500 eV primary impact energy with static bias voltages in the range of ± 1 V, limited by the oxidation potential as discussed above. Figure 8.17 contains the results of such experiments, where the top silver electrode was irradiated with 500 eV electrons within the active area, while the current was measured in *probe bottom* mode. Therefore, the bias voltage was applied to the irradiated electrode, while keeping the metered electrode at ground potential.

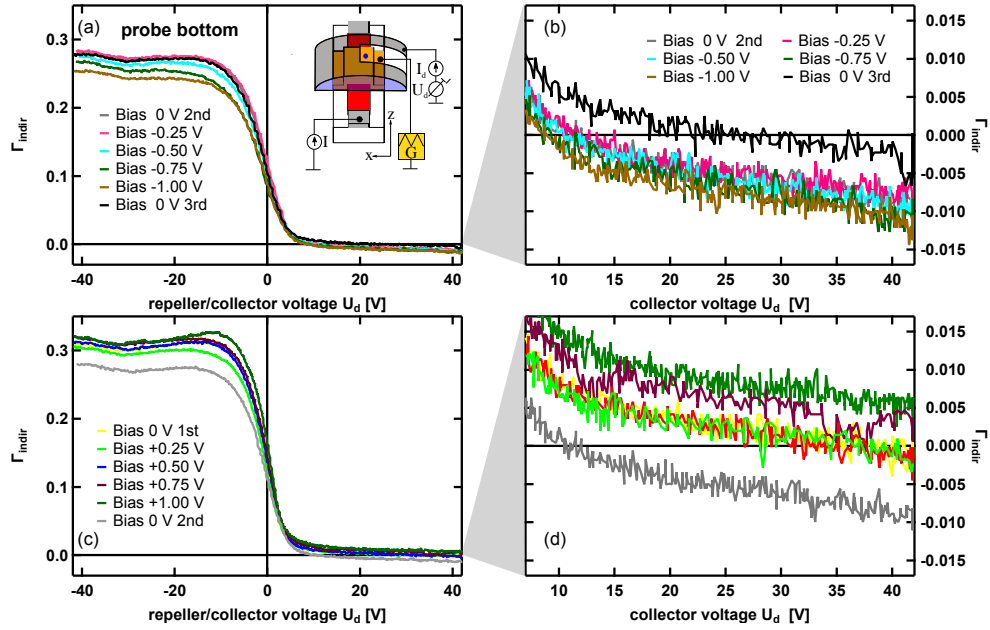


Figure 8.17: Yield in the *probe bottom* mode as a function of the collector/repeller voltage for different static bias voltages taken under irradiation of the active area with 500 eV electrons. **(a)**: Negative bias voltage. **(b)**: Zoomed view of (a) of the negative collector/repeller voltage. **(c)**: Positive bias voltage. **(d)**: Zoomed view of (c) of the positive collector/repeller voltage. Taken from [14].

As shown in panels (a) and (c) of figure 8.17, the measured signals strongly react on the applied bias voltage. The overall curve shape remains constant, but especially in case of *negative* values for U_d , the bias voltage shifts the observed yields Γ_{indir} downwards in case of negative bias (see panel (a)) and upwards in case of positive bias (see panel (c)). In case of $U_d < 0$ V, this is probably more a consequence of changes in the externally mediated processes than of the barrier's shift, since the application of a negative bias voltage in *probe bottom* mode is done by the application of a positive potential to the top silver electrode. This potential shift may significantly alter the trajectories of low-energetic electrons at the intersection of the oxidized aluminum and the silver electrode; this may influence the cross-absorption/re-absorption processes.

In panels (b) and (d) of the same figure, zoomed views of the measured values for $5 \text{ V} < U_d \leq 40 \text{ V}$ are shown to improve the visibility of the bias effects for $U_d > 10 \text{ V}$. The observed behaviour of a reduced yield in case of negative bias voltages and of an increased yield in case of positive bias is also true for $U_d > 0 \text{ V}$ as visible in panels (b) and (d), although the absolute values are much smaller in this case. For negative bias voltages, the sign of the polarity changes from positive to negative (see panel (b)), caused by a predominating of the hole current as discussed above. All curves exhibit a remaining slope pointing downwards, which is obviously independent of the applied bias voltage. This slope is therefore explained in terms of a decreasing emission from the external electrode towards the sample, due to the increasing external field strength which withholds more

electrons, while the shift of the whole curves is a consequence of the applied bias voltage and explained in terms of a modified oxide barrier.

The also observed differences between curves for 0 V bias labeled with 1st, 2nd and 3rd run point towards a modified barrier by the application of the bias voltage. If a positive bias voltage was followed by a negative bias voltage, these differences were extinguished, which also indicates that mobile charge carriers within the oxide were moved. Such so called remanence effects are indeed commonly reported in thin oxide layers (see [45, 85] for aluminum oxide and [56] for titanium oxide).

8.2.5 Bias voltage dependence of Γ_{dir}

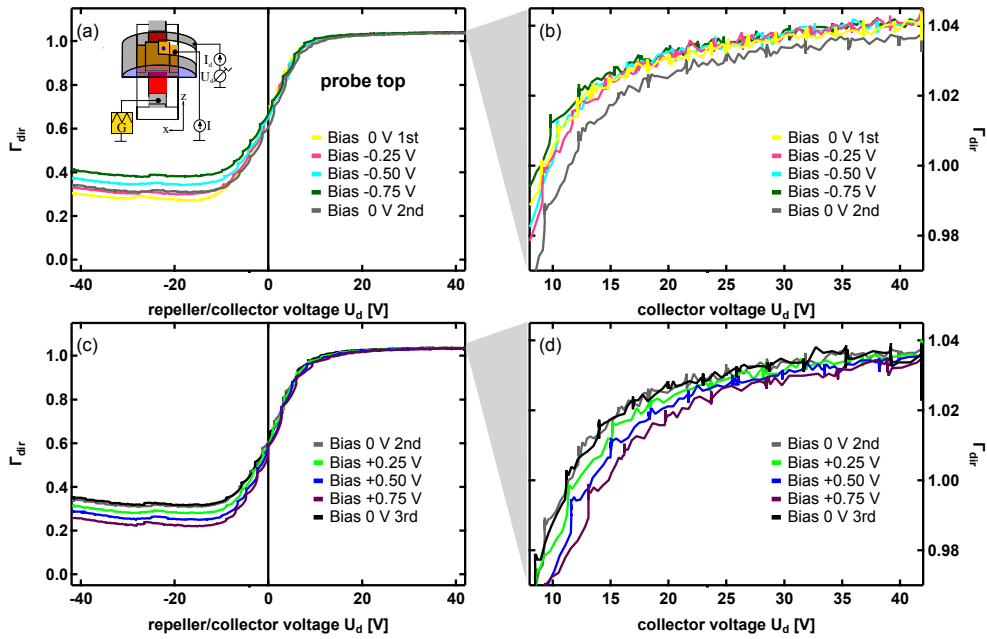


Figure 8.18: Yield in the *probe top* mode as a function of the repeller/collector U_d voltage for different static bias voltages taken under irradiation of the active area with 500 eV electrons. (a): Negative bias voltage. (b): Zoomed view of (a) of the negative collector/repeller voltage. (c): Positive bias voltage. (d): Zoomed view of (c) of the positive collector/repeller voltage.

Similar to the experiments in section 7.7, experiments of a bias dependence of Γ_{dir} in *probe top* mode for irradiation of the active area were performed under variation of the external electric field. The results are shown in figure 8.18. Obviously, the application of a bias voltage influences the obtained yield values especially in case of $U_d < -10$ V, when the electric field repels electrons emitted from the sample and accelerates electrons emitted from the external electrode towards the sample. A negative bias in this case is achieved by the application of positive potential to the bottom aluminum electrode and vice versa. This way, the re- and cross-absorption currents are influenced which causes the observed behaviour. This can be proven by looking at $U_d > +10$ V, where the external electrode

acts as collector and the influence of the bias voltage is negligible, which is expectable in a process, where the external electron emission is the dominating process.

8.3 Summary

The main findings for the **internal current** can be summarized as follows:

- True internal transport of excited charge carriers can be observed only in case a collector field is established (for $U_d > 0$) in *probe bottom* mode.
- The energy dependence in this case is weak.
- Also the impact angle dependence in this measuring mode is weak, a yield below zero indicated that the current of excited holes is dominant.
- The application of a bias voltage has a significant influence on the measured internal current.

The main findings for the **external current** can be summarized as follows:

- External emission is observed in the *probe top* mode at $U_d > 0$.
- The energy dependence in this case is strong as the yield Γ_{dir} decreases monotonous from values ≈ 1.7 at 100 eV to ≈ 1 for 1000 eV with the exception of 750 eV.
- The impact angle dependence is strong as the detected yield Γ_{dir} increases monotonous from values of 2.0 for normal incidence to 3.5 for 55°
- The application of a bias voltage only has a negligible influence on the measured external current.
- External measurements are influenced (adulterated) by emission of tertiary electrons

9 Conclusion

9.1 Conclusion

In a first series of experiments using MIM devices under electron irradiation, an *external* transport channel contributing to *internal* currents was suspected. The existence could be clearly proven in a second series of experiments with an externally controlled electric field above the sample. Two processes, namely a re-absorption of emitted electrons in the irradiated electrode and a cross-absorption from the irradiated towards the non-irradiated electrode could be identified. By the application of an external collector field, the cross- and re-absorption processes were effectively suppressed, revealing the existence of **true internal** processes.

By comparison of measurements with a collector field (for $U_d > 0$ V) to measurements with with a repeller field (for $U_d < 0$ V) established above the sample, a clear correlation between impact point and measured signal was observed, which allows an identification of the irradiated part of the MIM device. By comparing the results of *indirect* measurements with collector field to measurements with repeller field, the current arising from the cross-absorption process could be determined, which was found to be surprisingly high (about 20..30 % of I_{prim}).

The comparison of the results determined in *direct* experiments with collector and with repeller field, allows the determination of the *total external emission yield* ζ , which could also be obtained from measurements of the current I_d onto the collector/repeller electrode. The observed energy dependence shows a **decrease** with **increasing energy** and the determined yield ζ is qualitatively in reasonable agreement to literature data. The analysis of measurements on the oxide covered aluminum also allow a comparison with literature data, again revealing a reasonable agreement with literature data for irradiation of oxide covered aluminum.

In case, a collector field is established above the sample, the currents measured in *indirect* experiments are identical with **true internal currents**.

A dependence of the **true internal** emission yield Γ_{indir}^+ on the impact angle was determined, indicating a decrease by a factor 1.22 going from normal towards perpendicular incidence. In contrast to this finding, the true external emission yield Γ_{dir}^+ increases significantly by a factor of 1.5 with increasing impact angle, in case a collector field is established above the sample.

The true internal yield Γ_{indir}^+ shows a clear dependence on an internal bias voltage (applied between the MIM's top and bottom electrode). The observed behaviour can be well explained in terms of a modification of the internal barrier by the applied bias voltage. The determined values around $\Gamma_{\text{indir}}^+ \approx 0$ are explained in terms of an equipartition of a current of holes and a current of electrons, that cancel each other out. Depending on the applied bias voltage, this equipartition is distorted, either discriminating the electron or the hole contribution.

A discrimination of the emitted electrons in secondary and in backscattered electrons is not possible, since the emission of electrons from the collector/repeller electrode significantly alters the measured sample currents as well as the currents measured onto the collector/repeller electrode.

However, the question regarding the involvement of **external** processes to apparently **internal** device currents measured into the bottom electrode of the MIM devices under electron irradiation of the top silver electrode could be clearly answered. In case of electron irradiation, actually the majority of the obtained "internal" device current measured in *indirect* experiments originates from **external** emitted electrons cross-absorbed in the non-irradiated electrode, in case no external **collector field** is applied.

However, it could be also proven, that true internal processes exist, although they might be superimposed by external processes.

9.2 Outlook

From the findings, that an external collector field is - at least in experiments under electron irradiation - essential to determine true internal currents, it would be interesting to repeat at least some measurements for ion-impact on MIM devices, to examine, if a similar influence of externally mediated processes contributing to apparently internal processes is observed there.

10 Appendix

10.1 Acknowledgements

There are so many people who helped me:

At first I'd like to thank my wife and my children for their endless support and their patience with me. Also many thanks to my parents and my step-father.

I'd like to thank Andreas Wucher, Detlef Diesing, Christian Heuser and Domi Kovacs for the mentoring and the helpful discussions.

I'd like to thank Hendrix Demers for his assistance using Casino and for providing a programmed MIM multilayer.

Thanks to Matthias Herder for helping with me with the SIMION simulations.

There are so many other people who helped me during other experimental issues regarding the use and the repair of lasers:

Thanks to Joe Juennemann from Newport, to Samuel Goldwasser from Sam's Laser FAQ and to Mart Rahkema from Radiant Dyes.

Thanks to the DFG for funding in the Framework of the SFB 616 and partly in the SFB 1242.

Last, but not least I'd like to thank Mike Toepel for all he did for me!

Thank you!

11 Simulations of the collector/repeller field using SIMION

In a nutshell, the SIMION [86, 87] program package allows to simulate the trajectories of charged particles in electrical (and magnetic) fields for given electrode configurations, which is widely used to simulate e.g. electron optics as well as mass spectrometers by solving the Laplace equation. The calculations performed here were intended to estimate the influence of the collector's/repeller's electric field upon secondary electrons as well as on the primary electrons.

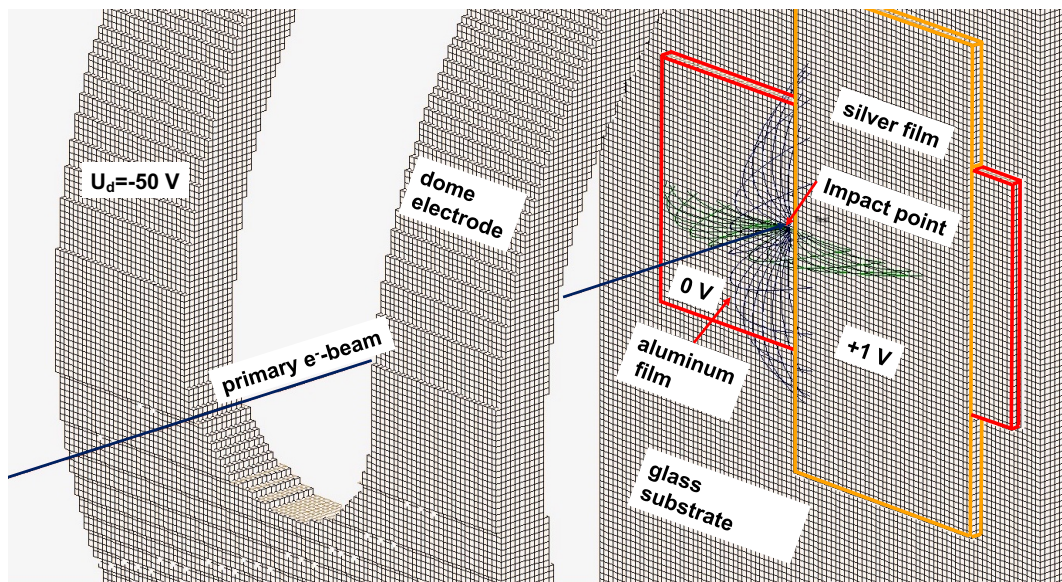


Figure 11.1: 3d view of a result of a SIMION simulation: The impact of a 250 eV primary electron beam was simulated in case of a collector/repeller voltage $U_d = -50V$. The so called "dome electrode" represents the collector/repeller electrode

In figure 11.1, the screen-shot of a simulation using the SIMION program package is shown. The orange box indicates the position of the silver film, the red box of the oxide covered aluminum. The primary electron beam is indicated as a black arrow coming from the left and entering the collector/repeller electrode ($U_d = -50 V$) through the slit towards the sample. To estimate the influence of the external electric field, a distribution of secondary electrons with a kinetic energy of 10 eV was started. The blue trajectories correspond to secondary electrons emitted in the x -direction of the sample's coordinate

system in direction of the slit; the green ones to electrons emitted perpendicular to the slit in z -direction. As visible, regardless to the emission direction, the secondary electrons are reflected back towards the surface by the external electric field. Since the dimensions of the system are approximately drawn to scale, the distance between point of emission and point of impact can be estimated to be half of the silver film's width and therefore 2 mm for 10 eV secondary electrons. To improve the visibility, the same simulation is shown from a different viewing angle in figure 11.2. Please note that the layer structure of the MIM cannot be simulated due to technical limitations (such thin layers are interpreted as mesh). The image shows a cut through the external electrode in x -direction. The blue trajectories are trajectories of 10 eV secondary electrons leaving the surface in an angular interval of $[-45^\circ, +45^\circ]$ in x -direction.

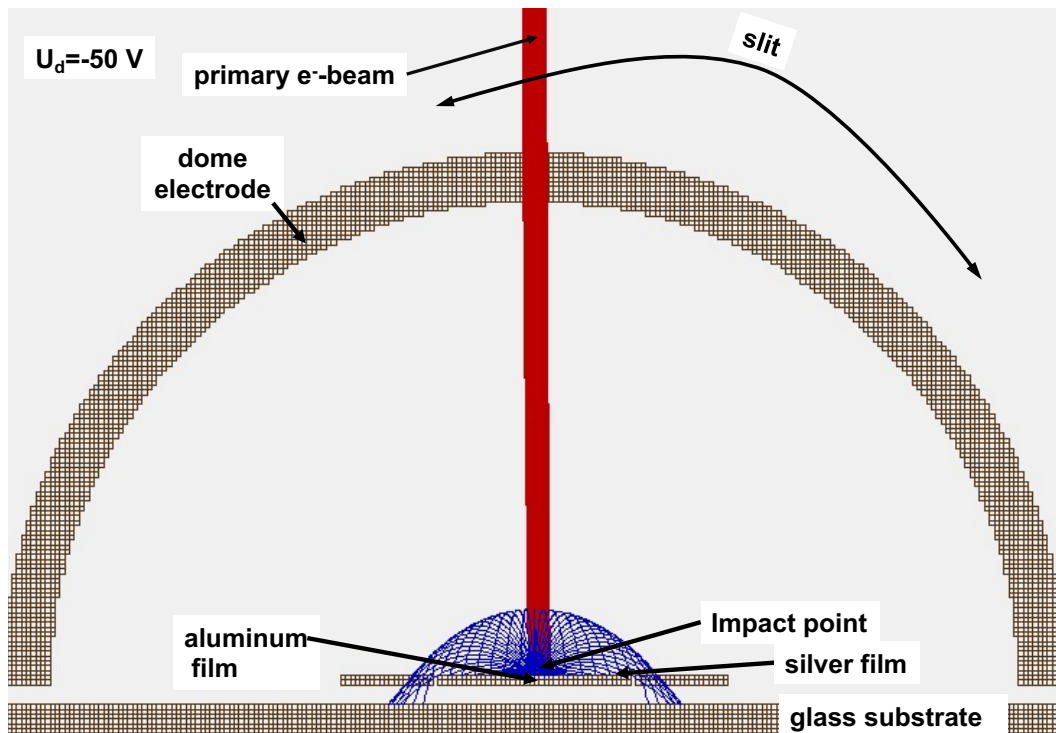


Figure 11.2: Side view of a result of a SIMION simulation: The impact of a 250 eV primary electron beam was simulated in case of a repeller voltage $U_d = -50\text{V}$.

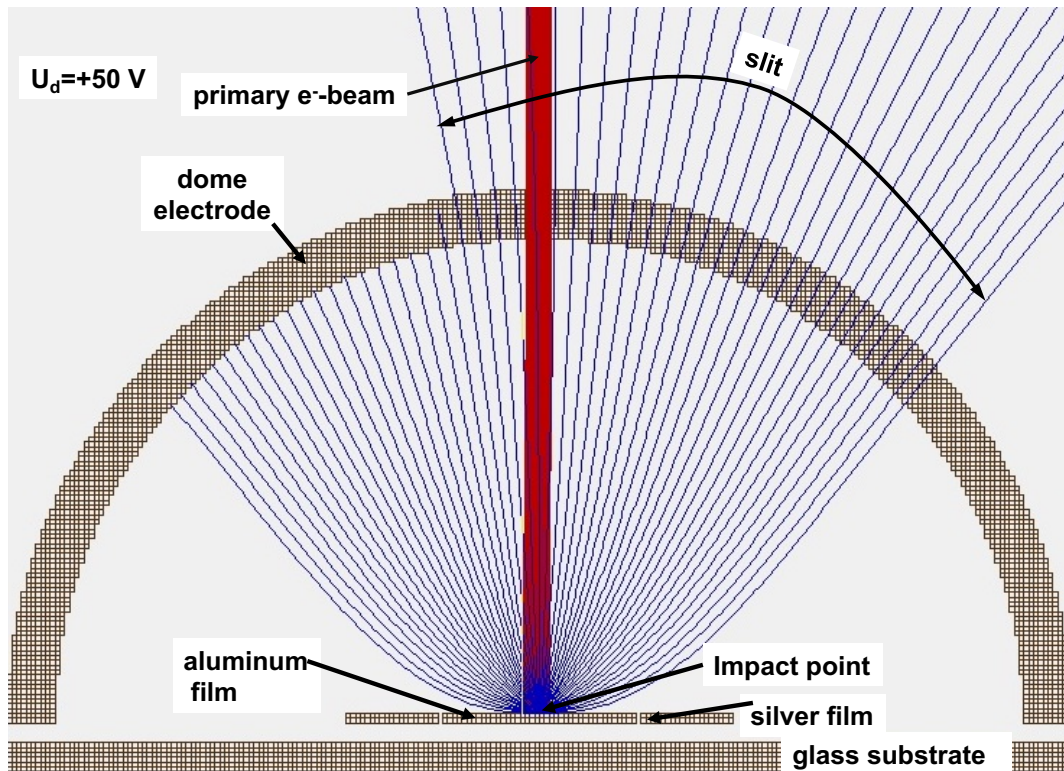


Figure 11.3: Side view of a result of a SIMION simulation: The impact of a 250 eV primary electron beam was simulated in case of a collector voltage $U_d = +50\text{V}$.

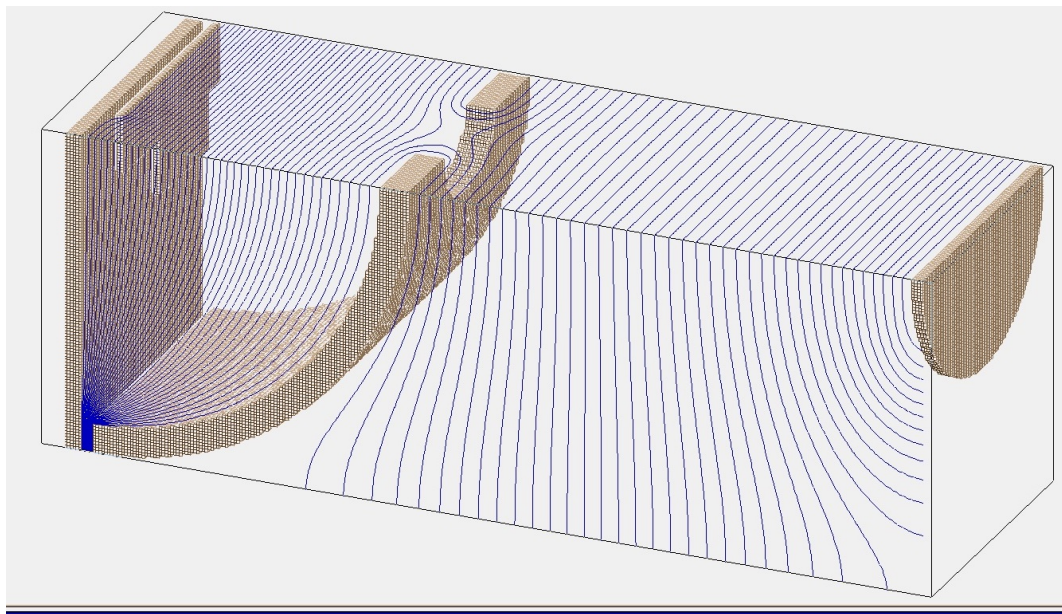


Figure 11.4: Side view of a result of a SIMION simulation: The potential of the external electric field.

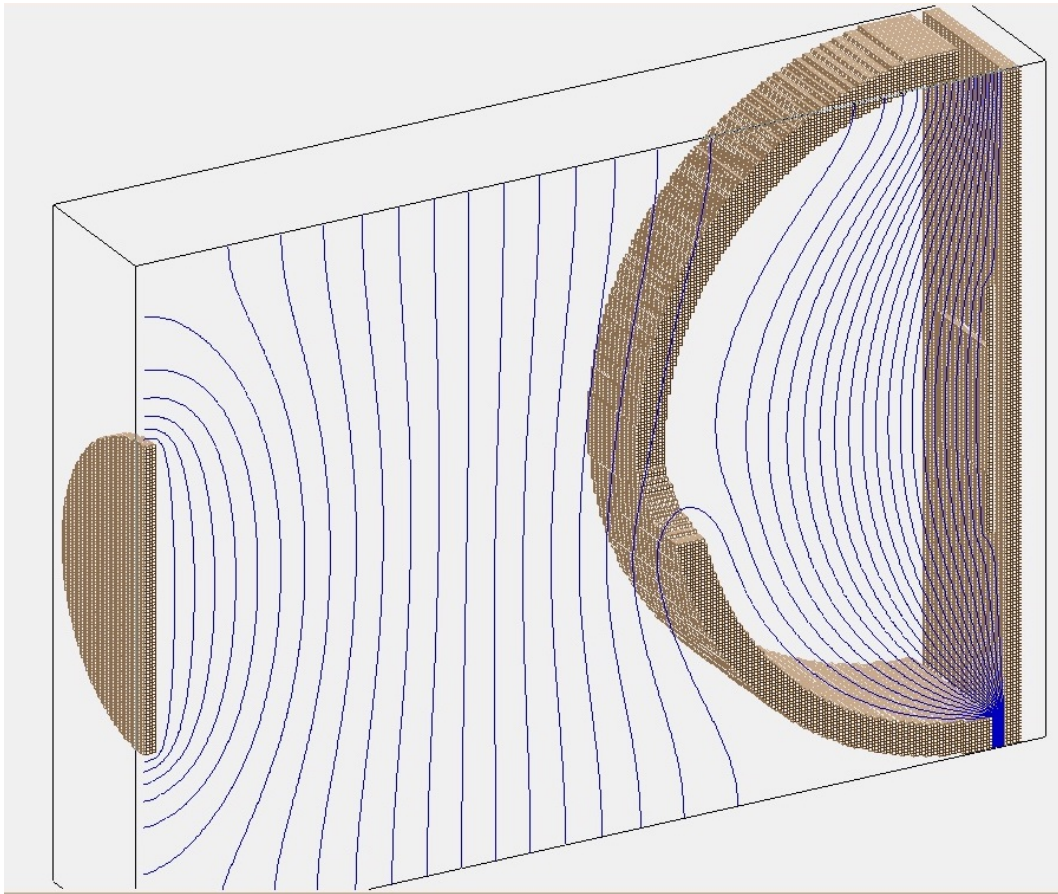


Figure 11.5: Side view of a result of a SIMION simulation: The potential of the external electrical field.

In figure 11.3, the result of a SIMION simulation at positive collector voltage U_d is shown. A part of the secondary electrons is able to leave the volume through the entrance slit.

Summarizing the results of the SIMION simulations, it was found that:

- Secondary electrons are reflected towards the surface in case of a negative repeller voltage U_d , but the impact point and the emission point are not identical. The distance between these points may be several mm for 10 eV secondary electrons.
- In case of positive collector voltages U_d , the secondary electrons may leave the volume through the entrance slit.
- The focal properties of the primary electron beam are not severely influenced by the application of the external electric field, although the impact point varies especially in case of low energetic primary electrons.
- SIMION is suitable to calculate the trajectories, but the excitation/emission process cannot be simulated using this software. Therefore all the electrons are started using a starting energy and a starting angle interval chosen in the software.

- The variation of the impact points' coordinates observed within the experiments in the x -scans can be explained by the influence of the collector's/repeller's electric field.
- The fact that emission point and impact point of back-reflected secondary electrons are not necessary identical but can be some mm away from each other, can be explained by the SIMION simulations. This means that re-absorption and cross-absorption currents may in principle evoke from emitted secondaries which are reflected to different areas of the MIM sample.

Bibliography

- [1] Joy, D. C. A database on electron-solid interactions. [web.utk.edu/ srcutk/-database.doc](http://web.utk.edu/srcutk/-database.doc), (2008).
- [2] Meyer, S., Diesing, D., and Wucher, A. Kinetic electron excitation in atomic collision cascades. *Phys. Rev. Lett.* **93**, 137601, Sep (2004).
- [3] Hopster, J., Diesing, D., Wucher, A., and Schleberger, M. Comparison of ion beam and electron beam induced transport of hot charge carriers in metal-insulator-metal junctions. *MRS Proceedings* **1354**, 1 (2011).
- [4] Kovacs, D. A., Winter, J., Meyer, S., Wucher, A., and Diesing, D. Photo and particle induced transport of excited carriers in thin film tunnel junctions. *Physical Review B* **76**(23) (2007).
- [5] Differt, D., Pfeiffer, W., and Diesing, D. Scanning internal photoemission microscopy for the identification of hot carrier transport mechanisms. *Applied Physics Letters* **101**(11), 111608–4, 09 (2012).
- [6] Kovacs, D. A., Peters, T., Haake, C., Schleberger, M., Wucher, A., Golczewski, A., Aumayr, F., and Diesing, D. Potential electron emission induced by multiply charged ions in thin film tunnel junctions. *Phys. Rev. B* **77**, 245432, Jun (2008).
- [7] Mildner, B., Hasselbrink, E., and Diesing, D. Electronic excitations induced by surface reactions of h and d on gold. *Chemical Physics Letters* **432**, 133 (2006).
- [8] Diesing, D., Kritzler, G., Stermann, M., Nolting, D., and Otto, A. Metal/insulator/metal junctions for electrochemical surface science. *J. Solid State Electrochemistry* **7**, 389 (2003).
- [9] Diesing, D., Kovacs, D. A., Stella, K., and Heuser, C. Characterization of atom and ion-induced "internal" electron emission by thin film tunnel junctions. *Nuclear Instruments and Methods in Physics Research Section B: Beam Interactions with Materials and Atoms* **269**, 1185 (2011).
- [10] Bernhart, A. *Mikroskopie mit ballistischen Elektronen und Löchern*. PhD thesis, Universität Duisburg-Essen, Fakultät für Physik, (2012).
- [11] Meyer, S., Diesing, D., and Wucher, A. The use of mim tunnel junctions to investigate kinetic electron excitation in atomic collision cascades. *Nuclear Instruments and Methods in Physics Research Section B: Beam Interactions with Materials and Atoms* **230**(1-4), 608–612 (2005).

-
- [12] Meyer, S., Heuser, C., Diesing, D., and Wucher, A. Kinetic electronic excitation of solids by fast-particle bombardment. *Phys. Rev. B* **78**, 035428, Jul (2008).
- [13] Marpe, M., Wucher, A., and Diesing, D. Transport of 75-1000 eV electrons in metal–insulator–metal devices. *Journal of Electron Spectroscopy and Related Phenomena* **223**, 37 – 52 (2018).
- [14] Marpe, M., Wucher, A., and Diesing, D. Preprint to be submitted: The influence of internal and external electric fields on the transport of energetic electrons in nanostructures. *Journal of Electron Spectroscopy and Related Phenomena* **xxx**, xxx (2018).
- [15] Schou, J. Secondary electron emission from solids by electron and proton bombardment. *Scanning Microscopy* **2(1988)**, 607–632 (1988).
- [16] Reimer, L. *Image Formation in Low-Voltage Scanning Electron Microscopy*, 98–99. Electron Optics. SPIE-The International Society for Optical Engineering (1993).
- [17] Seiler, H. Einige aktuelle Probleme der Sekundärelektronenemission. *Zeitschrift für angewandte Physik* **22(3)**, 249–263 (1967).
- [18] Cazaux, J. About the role of the various types of secondary electrons (se1; se2; se3) on the performance of lvsem. *Journal of Microscopy* **214(3)**, 341–347 (2004).
- [19] Pinard, P. T., Demers, H., Salvat, F., Gauvin, R., PENELOPE by Salvat, F., Fernández-Varea, J. M., Acosta, E., Sempau, J., and Llovet, X. `pypenelope`. <http://pypenelope.sourceforge.net/index.html>, (2012).
- [20] Demers, H., Poirier-Demers, N., Réal Couture, A., Joly, D., Guilmain, M., de Jonge, N., and Drouin, D. Casino monte carlo software. <http://www.gel.usherbrooke.ca/casino/index.html>, (2016).
- [21] Drouin, D., Couture, A. R., Joly, D., Tastet, X., Aimez, V., and Gauvin, R. Casino v2.42—a fast and easy-to-use modeling tool for scanning electron microscopy and microanalysis users. *Scanning* **29(3)**, 92–101 (2007).
- [22] Joy, D. A database of electron-solid interactions. extras.springer.com/2003/978-1-4613...3/Database/Joy%20Electron%20Database.doc, (2008).
- [23] Dekker, A. J. *Secondary Electron Emission*, volume 6 of *Solid State Physics*, 251 – 311. Academic Press (1958).
- [24] Bronshtein, R. and Segal, I. M. Inelastic scattering of electrons and secondary-electron emission in certain metals i. *Soviet Physics Solid State* **1(10)**, 1365–1496 (1960).
- [25] Seiler, H. Secondary electron emission in the scanning electron microscope. *Journal of Applied Physics* **54(11)**, R1 (1983).
- [26] Kanaya, K. and Ono, S. The energy dependence of a diffusion model for an electron probe into solid targets. *Journal of Physics D: Applied Physics* **11** (1978).

- [27] Oppel, W. and Jahrreiss, H. Messungen der Winkelverteilung von Sekundärelektronen an dünnen freitragenden Al- und Au-Schichten. *Zeitschrift für Physik* **252**(2), 107–117, Apr (1972).
- [28] Everhart, T. E., Saeki, N., Shimizu, R., and Koshikawa, T. Measurement of structure in the energy distribution of slow secondary electrons from aluminum. *Journal of Applied Physics* **47**(7), 2941–2945 (1976).
- [29] Shimizu, R. Secondary electron yield with primary electron beam of kiloelectron volts. *Journal of Applied Physics* **45**(5), 2107–2111 (1974).
- [30] Bindi, R., Lanteri, H., and Rostaing, P. Secondary electron emission induced by electron bombardement of polycrystalline metallic targets. *Scanning Microscopy* **1**(4), 1475–1490 (1987).
- [31] Pillon, J., Roptin, D., and Cailler, M. Secondary electron emission from aluminium. *Surface Science* **57**(2), 741 – 748 (1976).
- [32] Koshikawa, T. and Shimizu, R. A monte carlo calculation of low-energy secondary electron emission from metals. *Journal of Physics D: Applied Physics* **7**(9), 1303 (1974).
- [33] Seiler, H. Electron beam interactions with solids, (1984).
- [34] Langley, R., Bohdansky, J., Eckstein, W., Mioduszewski, P., Roth, J., Taglauer, E., Thomas, E., Verbeek, H., and Wilson, K. Data compendium for plasma-surface interactions. *Nuclear Fusion* **24**(S1), S9 (1984).
- [35] Reimer, L. *Scanning electron microscopy: physics of image formation and microanalysis: Ludwig Reimer*. Springer, (1985).
- [36] Salow, H. Über die winkelabhängigkeit der Sekundär-elektronen Emission von Isolatoren. *Physikalische Zeitschrift* **1**(41), 434–442 (1940).
- [37] Bruining, H. *Physics and Applications of Secondary Electron Emission*, chapter 4.4. Pergamon Science Series. Pergamon Press LTD (1954).
- [38] Jonker, J. On the theory of secondary electron emission. *Philips Research Reports* **7**(1), 1–20 (1952).
- [39] Hachenberg, O. and Brauer, W. Secondary electron emission from solids. In *Advances in Electronics and Electron Physics*, Marton, L. and Marton, C., editors, 413 – 499. Academic Press (1959).
- [40] Schou, J. Transport theory for kinetic emission of secondary electrons from solids. *Phys. Rev. B* **22**, 2141–2174, Sep (1980).
- [41] Sigmund, P. and Tougaard, S. *Electron Emission from Solids During Ion Bombardment. Theoretical Aspects*, 2–37. Springer Berlin Heidelberg, Berlin, Heidelberg (1981).

- [42] Segrè, E., Staub, H. H., Bethe, H. A., Ashkin, J., Ramsey, N. F., and Bainbridge, K. T. *Experimental nuclear physics*, volume 1. John Wiley & Sons, New York, (1953).
- [43] Hassel, A. W. and Diesing, D. Breakdown of ultrathin anodic valve metal oxide films in metal-insulator-metal-contacts compared with metal-insulator-electrolyte contacts. *Thin Solid Films* **414**(2), 296–303, 7 (2002).
- [44] Hassel, A. W. and Diesing, D. Modification of trap distributions in anodic aluminum tunnel barriers. *Journal of The Electrochemical Society* **154**(10), C558–C561 (2007).
- [45] Achim W. Hassel and Diesing, D. Trapping of transient processes in aluminium oxide thin films in a voltage pulse experiment. *Electrochem. Comm.* **4**, 1 (2002).
- [46] Marpe, M. Untersuchungen zur kinetischen Anregung von Festkörpern unter Clustertonbeschuss. Diploma thesis, University of Duisburg-Essen, (2009).
- [47] Krishna, S. *Handbook of thin film deposition*. William Andrew, (2012).
- [48] Stratton, R. Volt-current characteristics for tunneling through insulating films. *Journal of Physics and Chemistry of Solids* **23**, 1177–1190, September (1962).
- [49] Gundlach, K. H. Theory of metal-insulator-metal tunnelling for a simple two-band model. *J. Appl. Phys* **44**, 5005 (1973).
- [50] Diesing, D., Hassel, A. W., and Lohregel, M. M. Aluminium oxide tunnel junctions: influence of preparation technique, sample geometry and oxide thickness. *Thin Solid Films* **342**(1-2), 282–290, 3 (1999).
- [51] Stella, K., Bürstel, D., Franzka, S., Posth, O., and Diesing, D. Preparation and properties of thin amorphous tantalum films formed by small e-beam evaporators. *Journal of Physics D: Applied Physics* **42**, 135417 (2009).
- [52] Tomita, T., Harada, Y., Watanabe, H., and Etoh, T. Reduction of contamination in analytical electron microscopy. *SHINKU* **22**(4), 158–164 (1979).
- [53] Kovacs, D. A., Golczewski, A., Kowarik, G., Aumayr, F., and Diesing, D. Low-energy ion-induced electron emission in metal-insulator-metal sandwich structures. *Physical Review B* **81**(7) (2010).
- [54] Binnig, G., Rohrer, H., Gerber, C., and Weibel, E. Surface studies by scanning tunneling microscopy. *Phys. Rev. Lett.* **49**, 57–61, Jul (1982).
- [55] Schindler, B., Diesing, D., and Hasselbrink, E. Electronic excitations induced by hydrogen surface chemical reactions on gold. *The Journal of Chemical Physics* **134**(3), 034705 (2011).
- [56] Stella, K., Kovacs, D. A., Diesing, D., Brezna, W., and Smoliner, J. Charge transport through thin amorphous titanium and tantalum oxide layers. *Journal of The Electrochemical Society* **158**(5), P65–P74, 05 (2011).

- [57] Marpe, M., Heuser, C., Diesing, D., and Wucher, A. Internal electron emission in metal–insulator– metal thin film tunnel devices bombarded with kev argon and gold-cluster projectiles. *Nuclear Instruments and Methods in Physics Research Section B: Beam Interactions with Materials and Atoms* **269**(9), 972–976 (2011).
- [58] Lowney, J. R. Monte carlo simulation of scanning electron microscope signals for lithographic metrology. *Scanning* **18**(4), 301–306 (1996).
- [59] Lowney, J. R. Use of monte carlo modeling for interpreting scanning electron microscope linewidth measurements. *Scanning* **17**(5), 281–286 (1995).
- [60] Bronshtein, I. and Fraiman, B. S. Vtorichnaya elektronnaya emissiya.(secondary electron emission), (1969).
- [61] Myers, H. P. The secondary emission from copper and silver films obtained with primary electron energies below 10 ev. *Proceedings of the Royal Society of London A: Mathematical, Physical and Engineering Sciences* **215**(1122), 329–345 (1952).
- [62] Wittry, D. Secondary electron emission in the electron probe. In *Proc. 4th Int. Conf. on X-ray Optics and X-ray Microanalysis*, 168–180, (1966).
- [63] Bruining, H. and de Boer, J. H. Secondary electron emission part i secondary electron emission of metals. *Physica* **V**(1), 17–30 (1938).
- [64] Moncrieff, D. A. and Barker, P. R. Secondary electron emission in the scanning electron microscope. *Scanning* **1**(3), 195–197 (1978).
- [65] Reimer, L. and Tollkamp, C. Measuring the backscattering coefficient and secondary electron yield inside a scanning electron microscope. *Scanning* **3**(1), 35–39 (1980).
- [66] Hunger, H.-J. and KÜchler, L. Measurements of the electron backscattering coefficient for quantitative epma in the energy range of 4 to 40 kev. *physica status solidi (a)* **56**(1), K45–K48 (1979).
- [67] Böngeler, R. Rasterelektronenmikroskopie mit niedrigen Energien. Master thesis, Universität von Münster, (1992).
- [68] El–Gomati, M. M. and Assad, A. M. D. *On the Measurement of the Backscattering Coefficient for Low Energy Electrons*, 325–331. Springer Vienna, Vienna (1998).
- [69] Palluel, M. P. Composante rediffusée du rayonnement électronique secondaire des métaux. *Comptes Rendus Hebdomadaires Des Séances de L’Académie des Sciences* **224**(21), 1492–1494 (1947).
- [70] Tollkamp, C. Messungen zum Rückstreukoeffizienten und zur Sekundärelektronenausbeute in einem Rasterelektronenmikroskop. Diploma thesis, Universität von Münster, (1980).
- [71] El-Gomati, M. M., Walker, C. G. H., Assa’d, A. M. D., and Zadrazil, M. Theory experiment comparison of the electron backscattering factor from solids at low electron energy (250–5,000 ev). *Scanning* **30**(1), 2–15 (2008).

- [72] Walker, C. G., El-Gomati, M. M., Assa'd, A. M. D., and Zadrazil, M. The secondary electron emission yield for 24 solid elements excited by primary electrons in the range 250–5000 eV: a theory/experiment comparison. *Scanning* **30**(5), 365–380 (2008).
- [73] Demers, H., Poirier-Demers, N., Couture, A. R., Joly, D., Guilmain, M., de Jonge, N., and Drouin, D. Three-dimensional electron microscopy simulation with the casino monte carlo software. *Scanning* **33**(3), 135–146 (2011).
- [74] Joy, D. C. A database on electron-solid interactions. *Scanning* **17**(5), 270–275 (1995).
- [75] Shih, A. and Hor, C. Secondary emission properties as a function of the electron incidence angle. *IEEE Transactions on Electron Devices* **40**(4), 824–829, Apr (1993).
- [76] McKay, K. G. Secondary electron emission. *Advances in Electronics and Electron Physics* **1**, 65 – 130 (1948).
- [77] Böngeler, R., Golla, U., Kässens, M., Reimer, L., Schindler, B., Senkel, R., and Spranck, M. Electron-specimen interactions in low-voltage scanning electron microscopy. *Scanning* **15**(1), 1–18 (1993).
- [78] Quinn, J. J. Range of excited electrons in metals. *Physical Review* **126**(4), 1453–1457 (1962).
- [79] Malter, L. Thin film field emission. *Phys. Rev.* **50**, 48–58, Jul (1936).
- [80] Agarwala, V. K. and Fort, T. Effect of pressure and temperature on changes in the work function of aluminum during interaction with oxygen. *Surface Science* **48**(2), 527 – 536 (1975).
- [81] Mueller, C. W. The secondary electron emission of pyrex glass. *Journal of Applied Physics* **16**(8), 453–458 (1945).
- [82] Schneider, P. M. and Fowler, W. B. Band structure and optical properties of silicon dioxide. *Phys. Rev. Lett.* **36**, 425–428, Feb (1976).
- [83] Heuser, C., Marpe, M., Diesing, D., and Wucher, A. Kinetic excitation of solids induced by energetic particle bombardment: Influence of impact angle. *Nuclear Instruments and Methods in Physics Research Section B: Beam Interactions with Materials and Atoms* **267**(4), 601–604 (2009).
- [84] Heuser, C., Marpe, M., Diesing, D., and Wucher, A. The possible role of anisotropy in kinetic electronic excitation of solids by particle bombardment. *Nuclear Instruments and Methods in Physics Research Section B: Beam Interactions with Materials and Atoms* **269**(11), 1190–1194 (2011).
- [85] Lohrengel, M. Thin anodic oxide layers on aluminium and other valve metals: high field regime. *Materials Science and Engineering: R: Reports* **11**(6), 243 – 294 (1993).
- [86] Manura, D., Dahl, D., and et al. Simion, (January 2008).
- [87] Simion 8.0. www.simion.com, (2006-20018).

List of Tables

| | | |
|-----|---|----|
| 7.1 | Computed impact energy dependence of the penetration depth of primary electrons and of the escape depth of backscattered electrons calculated using the Casino Monte-Carlo package [20] for a 40 nm-thick silver film. Taken from [13]. | 77 |
|-----|---|----|

List of Figures

| | | |
|-----|---|----|
| 4.1 | Secondary electrons excited immediately after the penetration of the sample's surface by an primary electron are called secondary electrons δ_0 ; secondary electrons excited by a primary electron reflected back towards the surface in deeper layers of the irradiated sample, are called secondary electrons δ_1 . Primary electrons dissipate kinetic energy to the sample's electronic subsystem during their way through the solid. The amount of dissipated energy is proportional to the traveled way of the primary electrons within the solid. Reproduced from [15]. | 7 |
| 4.2 | (a) Geometry of the escape of a liberated electron from depth x with the initial energy E_0 for normal incidence (relative to surface normal) (reproduced from [15]) (b) Electron passing the surface barrier: For planar barrier, the energy component parallel to surface remains unchanged (reproduced from [15]). | 11 |
| 5.1 | Black curve: voltage ramp applied between top and bottom electrode; red curve: current induced in the bottom electrode by the voltage ramp. The charging current ΔI gives the dynamic capacitance C_d (see equation 5.2).See also [13]. | 15 |
| 5.2 | Charging current as a function of the voltage feed: ΔI is affected linearly by the voltage feed.See also [13]. | 15 |
| 5.3 | Equivalent circuit diagram of the most simplified description of a MIM . . . | 16 |
| 5.4 | Equivalent circuit diagram of the more realistic description of a MIM . . . | 17 |
| 5.5 | Equivalent circuit diagram of the description of a realistic MIM | 18 |
| 6.1 | Sketches of the MIM samples: (a) : Schematic sketch of a MIM device indicating the layer structure as well as the coordinate system (b) : Schematic cross sectional view (not drawn to scale) along the x -direction in the middle of the active area (crossing area of bottom and the top electrode); Δ denotes the increase of the film's length due to shadowing effects during the evaporation process. See also [13]. | 22 |
| 6.2 | (a) Top panel: AFM image of a MIM's active area scanned across a scratch; the position of the line-scan (bottom panel) is indicated by the red line. (b)Top panel: AFM image of the same sample at the step from silver film to the glass substrate; the position of the line-scan (bottom panel) is indicated by the red line. See also [13]. | 23 |

| | | |
|-----|--|----|
| 6.3 | Microscopic pictures of an irradiated MIM device taken by a Keyence digital microscope (data: courtesy of J.-C. Knoblich). (a) Zoom image of the area marked with the black line in the overview shown in panel (c): transition between the active area and the oxide covered aluminum film; the sharpness of the edge is defined by the sharpness of the evaporation masks. (b) like (a), but further zoomed in. (c) Overview of the sample. The black line marks the edge between the active area and the AlO_x film; the red line the edge between silver on glass and the active area. (d) Zoom image of the edge marked by the red line in (c) showing a transition area of about $4.6 \mu\text{m}$ where the silver film runs out over the edge of the aluminum film. See also [13]. | 25 |
| 6.4 | SEM images of MIM samples (data courtesy of A. Reichert) (a) : Overview (900x magnification) of the overlap between the active area, the silver film and the AlO_x film on the glass substrate, showing visible contamination where the sample was frequently irradiated. (b) : Zoom image of the active area (magnification 10000x): Typical diameter of the contamination is $2 \mu\text{m}$ (c) : Image (magnification 900x) of the silver film next to the active area where the sample was rarely irradiated: nearly flat surface without contamination. (d) : Image (magnification 900x) of the active area where the sample was frequently irradiated, a rod like dust particle and small circular structures are visible. (e) : Image (magnification 430x) of the edge between active area/ silver film of an irradiated sample; a needle scratch made intentionally for AFM thickness measurements is visible. (f) : Image (magnification 900x) of the silver film of a non-irradiated sample showing dust flakes, but no circular structures. | 27 |
| 6.5 | Different measuring modes used for MIM samples: (a) : <i>probe top</i> mode where the silver top electrode is metered with the current meter input of the potentiostat, while the bottom aluminum electrode is connected to the bridged counter-/reference inputs and kept at virtual ground. The x -coordinate is chosen to run along the silver film and the z -coordinate along the aluminum film. The blue dashed lines indicate the path the sample is steered during the electron irradiation. (b) : Same as (a), but in the <i>probe bottom</i> mode, where the bottom electrode is metered and the top electrode kept at virtual ground. Taken from [13]. | 28 |
| 6.6 | Wiring diagram in case no external collector/repeller electrode is installed. | 29 |
| 6.7 | Schematic of the set-up of experiments with collector/repeller electrode: (a) <i>probe top</i> mode where the current to the silver top electrode is measured while keeping the aluminum bottom electrode at a constant potential; the collector/repeller electrode is kept at U_d while metering the current I_d to the electrode. The sample is either moved horizontally in x -direction or vertically in z -direction symbolized by the blue dashed lines while detecting all currents as function of the momentary beam position. (b) same as (a), but in the <i>probe bottom</i> mode, where the current into the aluminum bottom electrode is measured and the silver top electrode being kept at a constant potential. See [14]. | 31 |

| | | |
|------|--|----|
| 6.8 | Wiring diagram in case of measurements as function of the collector/repeller voltage U_d | 32 |
| 6.9 | Photograph of the ultra high vacuum chamber and the equipment related to the MIM experiments. The numbers in the photograph denote: (1) UHV chamber, (2) view port towards the sample, (3) electron gun, (4-7): rotatable x - y - z -manipulator:(4) micrometer measuring screw for the y -direction, (5) like (4) for the x -direction, (6) measuring screw for the z -direction, (7) voltage feed-throughs, (8) turbo molecular pump, (9) potentiostat, (10) data logger, (11) vacuum gauge controller, (12) residual gas analyzer, (13) ion gun | 33 |
| 6.10 | (a-c) : Photographs of the sample holder (a) : Typical configuration for the experiments without external collector/repeller electrode. The numbers denote: (1) front shield of the Faraday cup (FC) with entrance hole, (2) oxide covered aluminum electrode of the MIM, (3) active area of the MIM. (b) : Typical configuration for the experiments with external collector/repeller electrode. The numbers denote: (1) front shield of the Faraday cup (FC) with entrance hole, (2) oxide covered aluminum electrode of the MIM, (3) active area of the MIM, (4) collector/repeller electrode, (5) slit. (c) : Typical configuration for the experiments with external collector/repeller electrode mounted inside the UHV vessel. The numbers denote: (1) front shield of the Faraday cup (FC) with entrance hole, (4) collector/repeller electrode, (5) slit, (6) electron gun, (7) vacuum gauge. | 34 |
| 6.11 | (a) : Energy levels in the MIM device at 0 V bias voltage between silver top and aluminum bottom electrode. (b) : A negative bias voltage on the bottom electrode acts as retarding field for excited electrons in the top electrode and eases the transport of excited holes. (c) : A positive bias voltage on the bottom electrode acts as retarding field for excited holes in the top electrode and eases the transport of excited electrons. | 36 |
| 6.12 | Current measured on the FC_{front} – and into the FC as function of the x -position: panel (a) for 110 eV, panel (b) for 500 eV, panel (c) for 750 eV and panel (d) for 1000 eV. | 38 |
| 6.13 | Schematic of the different irradiation/detection scenarios: (a) : Schematic cross-sectional view in x -direction across the active area. (b) : Schematic cross-sectional view in z -direction across the aluminum film. Currents are explained in section 6.10. The table explains, which combination of irradiated position and measuring mode corresponds to <i>direct</i> and which to <i>indirect</i> experiments. See also [13]. | 39 |
| 6.14 | Schematic of the irradiation scenarios and the resulting current contributions to the measured sample current: (a) current contributions and possible irradiation spots during x -scans for collector/repeller voltages $U_d > 0V$; (b) same as (a) for collector/repellervoltages $U_d < 0V$; (c) during z -scans for collector/repeller voltages $U_d > 0V$; (d) like (c) for collector/repellervoltages $U_d < 0V$. Taken from [14]. | 41 |

| | | |
|-----|---|----|
| 7.1 | Visualization of position dependent experiments: The image shows a schematic of a MIM and the results (normalized currents) of three different scans performed for a primary kinetic energy of 500 eV: (a) <i>x</i> -scan outside the active area for a path across the glass substrate towards the oxide covered aluminum towards the glass again while measuring the current into the aluminum bottom electrode (<i>probe bottom</i> mode). (b) <i>x</i> -scan across the active area starting on a contact pad of conductive carbon (used for wiring the MIM) along the silver film outside the active area, crossing the active area, along the silver film outside the active area towards the second contact pad of carbon while measuring the current into the silver top electrode. (c) <i>z</i> -scan along the aluminum film starting on the oxide covered aluminum film, crossing the silver film within the active area and ending again on the oxide covered aluminum while measuring the current into the top silver electrode. | 50 |
| 7.2 | <i>x</i> -scans to determine the position of the active area (1) in <i>probe bottom</i> mode with electron beam being scanned like depicted by the dashed blue line in pictogram (1): path from glass/ AlO_x on Al/glass (2) in <i>probe top</i> mode with electron beam being scanned as depicted by the dashed blue line in pictogram (2): path from silver on glass/ active area / silver on glass with 500 eV kinetic impact energy. The grey box indicates the position of the aluminum film, which is also the underlay of the active area. Taken from [13]. | 51 |
| 7.3 | (a) : Results of <i>x</i> -scans in <i>probe top</i> mode (see pictogram (a)) for different kinetic impact energies in the range of 75..1000 eV. The <i>z</i> -coordinate (as well as the <i>y</i> -coordinate) were identical for all scans. (b) : same as (a) in <i>probe bottom</i> mode (see pictogram (b)). The grey box indicates the position of the active area, which is defined by the width of the underlying aluminum film. See also [13]. | 53 |
| 7.4 | (a) : Results of <i>z</i> -scans in <i>probe top</i> mode (see pictogram (a)) for different kinetic impact energies in the range from 75..1000 eV. The <i>x</i> -coordinate (as well as the <i>y</i> -coordinate) were identical for all scans. (b) : same as (a) in <i>probe bottom</i> mode (see pictogram (b)). The grey box indicates the position of the active area. For $142 \text{ mm} \leq z \leq 146 \text{ mm}$, the active area is irradiated (shown as grey shaded area), while otherwise the e^- -beam impinges on the AlO_x /aluminum film. See also [13]. | 55 |
| 7.5 | Evaluation of the <i>x</i> - and <i>z</i> -scans as function of the primary impact energy. (a) : Direct emission yield in <i>probe top</i> mode evaluated by reading out plateau values from parts (a) of figure 7.3 and of figure 7.4, respectively, along with averaged result (red curve). (b) : Indirect emission yield in <i>probe bottom</i> mode evaluated by reading out plateau values from parts (b) of figure 7.3 and of figure 7.4, respectively, along with averaged result (red curve). See also [13]. | 57 |

| | | |
|------|---|----|
| 7.6 | <p>(a): Results of simulations computed using Casino for δ in comparison to available literature data as function of the kinetic impact energy for irradiation of silver. (b): Results of simulations computed using Casino and pyPENELOPE for η in comparison to available literature data as function of the kinetic impact energy also for irradiation of silver. Bronshtein Fraiman [60], Myers [61], Wittry [62], Bruining de Boer [63], Shimizu [29], Moncrieff Barker [64], Reimer Tollkamp [65], Hunger K uchler [66], B ngeler [67], El-Gomati Assa'd [68], Palluel [69], Diploma Thesis Tollkamp [70], Casino [20, 21], pyPENELOPE [19], El-Gomati [71, 72]</p> | 59 |
| 7.7 | <p>(a): Results of the simulated backscattering coefficient η as a function of the primary kinetic energy calculated using Casino 3.3, Casino 2.42 and pyPENELOPE for 40 nm- thick silver layers and using Casino 3.3 and a MIM multi-layer (provided by H. Demers). (b): Results of the simulated secondary electron emission coefficient δ as function of the primary kinetic energy calculated using Casino 3.3 for 40 nm-thick silver layer and for a MIM multi-layer (provided by H. Demers).</p> | 61 |
| 7.8 | <p>(a): Results of the simulated backscattering coefficient η as a function of the impact angle calculated using Casino 3.3 and Casino 2.4.2 for irradiation of a 40 nm thick silver film. (b): Results of the simulated secondary electron emission coefficient δ as function of the impact angle calculated using Casino 3.3 for irradiation of a 40 nm thick silver film.</p> | 62 |
| 7.9 | <p>The results of simulations for the transmission through a 10 nm thick silver film calculated using pyPENELOPE are shown.</p> | 63 |
| 7.10 | <p>Total external electron emission yield ζ for silver as a function of the primary kinetic energy. (a): Comparison of results for Γ_{dir} from this work (averaged results obtained from x- and z-scans as shown in 7.5) with literature data obtained by summing up backscattering and secondary electron yield $\eta + \delta = \zeta$: Tollkamp 1980 (Diploma Thesis) [70], Bronshtein Fraiman (1969) [60] found in [74, 1], B ngeler (1992) [67], Shimizu (1974) [29] and El-Gomati (2008) [71, 72]). (b): Comparison of results from this work with results of Monte-Carlo simulations using Casino 3.3 [73, 20]. See also [13].</p> | 64 |
| 7.11 | <p>Total external emission yield ζ (a) for silver and (b) for aluminum as function of the primary impact energy: Comparison of literature data (obtained by summing up the backscattering coefficient η and the secondary electron coefficient δ) as reported in [71, 72, 60] with experimental results from this work. The values for Γ_{dir} in panel (a) are taken from figure 7.5; the values for irradiation of the oxide covered aluminum in panel (b) were evaluated from part (b) of figure 7.4 at $z = 142$ nm, calculated in the same manner. See also in [13].</p> | 66 |
| 7.12 | <p>Comparison of current curves normalized to I_{prim}: blue curves: measured with potentiostat, red curves: measured with I/U converter, black curve: measured with picoammeter (a) x-scans in the <i>probe bottom</i> mode at 500 eV, (b) z-scans in the <i>probe top</i> mode at 500 eV, (c) x-scans in the <i>probe top</i> mode at 500 eV, (d) z-scans in the <i>probe top</i> mode at 300/275 eV . . .</p> | 67 |

| | | |
|------|---|----|
| 7.13 | <i>x</i> -scans along the silver top electrode at $E_{\text{prim}} = 500 \text{ eV}$ in (a) the <i>probe top</i> mode (see insert (a)) and in (b) the <i>probe bottom</i> mode (see insert (b)), recorded at different impact angles. In (c) the full width at half maximum as function of impact angle θ for different E_{prim} is shown. See also in [13]. | 68 |
| 7.14 | (a) : Γ_{dir} measured in <i>probe top</i> mode under irradiation of the top silver electrode in the center of the active area for different primary impact energies evaluated from panel (a) of figure 7.13. (b) : Γ_{indir} measured in <i>probe bottom</i> mode for different primary impact energies evaluated from panel (b) of figure 7.13. See also in [13]. | 69 |
| 7.15 | Results of the measured impact angle dependencies of the external electron emission yield Γ_{dir} in case of MIM experiments and of the total yield ζ in case of literature data. All data normalized to the signal at normal incidence. Results of MIM measurements as shown in panel (a) of figure 7.14, molybdenum ribbons from Shih and Hor [75], silver and copper bulk samples [67, 77] and Tollkamp [70]. See also in [13]. | 70 |
| 7.16 | Black curve (left ordinate axis): Applied bias voltage as function of time. Red curve (right ordinate axis): Current answer of the MIM to the applied voltage ramp under electron irradiation as function of time. Blue curve (right ordinate axis): Corrected current answer of the MIM obtained by subtracting $2 \cdot \Delta I$ from the red curve between maximal and minimal bias voltage to remove the influence by dielectric effects. Measured under irradiation of the active area for $I_{\text{prim}} = -24.1 \text{ nA}$ at $E_{\text{prim}} = 275 \text{ eV}$. See also in [13]. | 71 |
| 7.17 | Internal emission yield Γ_{indir} as function of the bias voltage measured in <i>probe bottom</i> mode for different kinetic energies, obtained like described in 7.16. Also see in [13]. | 72 |
| 7.18 | Influence of the bias voltage on the externally emitted secondary electrons: (a) : zero bias; (b) : negative bias (c) : positive bias. See also [13]. | 73 |
| 7.19 | External emission yield Γ_{dir} as function of the bias voltage measured in <i>probe top</i> mode for different kinetic energies, obtained like described in 7.16. See also in [13]. | 73 |
| 7.20 | <i>x</i> -scans to determine the position of the active area (1) in <i>probe top</i> mode with electron beam being scanned like depicted by the dashed blue line in pictogram (1): path from glass/ AlO_x on Al/glass (2) in <i>probe bottom</i> mode with electron beam being scanned like depicted by the dashed blue line in pictogram (2): path from silver on glass/active area/silver on glass with 500 eV kinetic impact energy. The grey box indicates the position of the aluminum film, which is also the underlay of the active area. Taken from [13]. | 75 |

| | | |
|-----|---|----|
| 8.1 | <p>(a): (1) Normalized current measured in the bottom aluminum electrode as a function of the x-position with $U_d = +40$ V during a scan of the primary electron beam across the aluminum electrode (see pictogram (1)). (2) Normalized current measured in the silver top electrode as a function of the x-position with $U_d = +40$ V for scanning across the silver electrode (see pictogram (2)). (b): like in (a) but for $U_d = -40$ V. The black line indicates the x-position where the z-scans (see below) were performed. The area for $x > 40.5$ mm is shaded, since the silver film is left there towards a carbon contact. See also in [14].</p> | 81 |
| 8.2 | <p>(a): Current in <i>probe top</i> mode measured in the silver electrode normalized to the primary current as function of the x-position scanning across the active area for $U_d = +40$ V. The black line indicates the x-position at which the z-scans were performed. (b): Like in (a) but with $U_d = -40$ V. See also in [14].</p> | 83 |
| 8.3 | <p>(a): Current in the <i>probe bottom</i> mode measured in the aluminum electrode normalized to the primary current as function of the x-position scanning across the active area for $U_d = +40$ V for different kinetic energies. The black line indicates the x-position at which the z-scans were performed. (b): Like in (a) but with $U_d = -40$ V. See also in [14].</p> | 84 |
| 8.4 | <p>(a): Normalized current measured in <i>probe top</i> mode with positive <u>collector/repeller</u> voltage $U_d = +40$ V as a function of the z-position while scanning the primary electron beam at different kinetic energies across the active area. (b): Same as (a) but for $U_d = -40$ V. The black vertical line at $z \approx 147.2$ mm in panels (a) and (b) indicates the z-position, at which the x-scans were performed. See also in [14].</p> | 87 |
| 8.5 | <p>(a): Normalized current measured in <i>probe bottom</i> mode with positive <u>collector/repeller</u> voltage $U_d = +40$ V as a function of the z-position while scanning the primary electron beam at different kinetic energies across the active area. (b): Enlarged view of panel (a) for $145 \text{ mm} \leq z \leq 148 \text{ mm}$. (c): Same as (a) but for $U_d = -40$ V. The black line at $z \approx 147.2$ mm in panels (a) and (c) indicates the z-position at which the x-scans were performed.</p> | 88 |
| 8.6 | <p><i>Direct</i> and <i>indirect</i> emission yield calculated from the current measured in the irradiated silver electrode (<i>direct</i> experiments) (panels (a)-(b)) and in the underlying, non-irradiated aluminum electrode (<i>indirect</i> experiments) (panels (c)-(d)) measured during irradiation of a MIM's active area for positive and negative collector/repeller voltages, respectively. All current values were normalized to the primary electron current I_{prim}. See also in [14].</p> | 90 |
| 8.7 | <p>(a): Cross-absorption yield, i.e., cross-absorption current calculated using equation 6.21 normalized to the primary electron current, measured under irradiation of the top silver surface at three different spots of the active MIM junction area: (a) the clean silver surface at $x = 35$ mm on one edge of the active area; (b): the clean silver surface at $x = 38.7$ mm on the other edge of the active area; (c): the carbon contaminated spot in the center of the active area ($x = 37.4$ mm). See also in [14].</p> | 92 |

| | | |
|------|--|-----|
| 8.8 | (a): Γ_{dir} as function of the impact angle (relative to surface normal) obtained from <i>x</i> -scans in <i>probe top</i> mode at 500 eV primary impact energy for $U_d = \pm 40$ V. (b): like (a) but Γ_{indir} obtained from <i>probe bottom</i> experiments. | 94 |
| 8.9 | (a): Γ_{MIM} normalized to the signal obtained for normal incidence as function of the impact angle (relative to surface normal) obtained from measurements on similar MIM devices under irradiation with Ar^+ -ions for different kinetic impact energies without external electrode. Reproduced from [46, 57]. | 95 |
| 8.10 | Solid lines: Γ_{dir} obtained from measurements of the current into the irradiated top electrode for irradiation of the active area as function of voltage U_d applied to external electrode for different kinetic impact energies. Dashed lines: Current I_d measured simultaneously to sample current on the external electrode. See also in [14]. | 97 |
| 8.11 | Solid lines: Γ_{dir} obtained from measurements of the current into the irradiated top electrode for irradiation of the silver film outside the active area as function of voltage U_d applied to external electrode for different kinetic impact energies. Dashed lines: Current I_d measured simultaneously to sample current on the external electrode. | 98 |
| 8.12 | Solid lines: Γ_{dir} obtained from measurements of the current into the irradiated bottom electrode for irradiation of the oxide covered aluminum film as function of voltage U_d applied to external electrode for different kinetic impact energies. Dashed lines: Current I_d measured simultaneously to sample current on the external electrode. | 99 |
| 8.13 | Overview of <i>indirect</i> experiments where the active area is irradiated while the current is measured in the <i>probe bottom</i> mode. Γ_{indir} is calculated by the formula 6.6 and shown as a function of the collector/repeller voltage U_d for different kinetic energies from 100 eV (a) to 1000 eV (c). Taken from [14]. | 100 |
| 8.14 | Evaluation of <i>indirect</i> experiments as a function of the kinetic energy for different collector/repeller voltages: +40 V in (a), 0 V in (b) and -40 V in (c). Taken from [14]. | 101 |
| 8.15 | (a): Total emission yield ζ as a function of the kinetic electron impact energy during irradiation of a silver film as reported in the literature obtained by summing η and δ : El-Gomati from [71, 72], Bronshtein Fraiman from [60] and average of results from <i>x</i> - and <i>z</i> -scans (see figure 7.5 and [13]) along with results calculated using Casino Monte Carlo for modified settings (see figure 7.6 in chapter 7.2 and [20, 13]). (b): Results of experiments discussed within this thesis obtained by evaluating I_d^+ (black curve) and by evaluating the sample current using equation 4.1 (red curve), respectively. See also in [14]. | 103 |

| | | |
|------|--|-----|
| 8.16 | Total emission yield ζ as a function of the kinetic electron impact energy during irradiation of aluminum film as reported in the literature obtained by summing η and δ : El- Gomati from [71, 72], results from z-scans measured without external electrode (black curve) see section 7.1.3 (see also [13]) along with results evaluated from figures 8.12 and 8.13 evaluated using equation 4.1 (red curve) and with current measured onto the external electrode for irradiation of the oxide covered aluminum (blue curve). | 104 |
| 8.17 | Yield in the <i>probe bottom</i> mode as a function of the collector/repeller voltage for different static bias voltages taken under irradiation of the active area with 500 eV electrons. (a) : Negative bias voltage. (b) : Zoomed view of (a) of the negative collector/repellervoltage. (c) : Positive bias voltage. (d) : Zoomed view of (c) of the positive collector/repeller voltage. Taken from [14]. | 106 |
| 8.18 | Yield in the <i>probe top</i> mode as a function of the repeller/collector U_d voltage for different static bias voltages taken under irradiation of the active area with 500 eV electrons. (a) : Negative bias voltage. (b) : Zoomed view of (a) of the negative collector/repellervoltage. (c) : Positive bias voltage. (d) : Zoomed view of (c) of the positive collector/repeller voltage. | 107 |
| 11.1 | 3d view of a result of a SIMION simulation: The impact of a 250 eV primary electron beam was simulated in case of a collector/repellervoltage $U_d = -50V$. The so called "dome electrode" represents the collector/repeller electrode | 112 |
| 11.2 | Side view of a result of a SIMION simulation: The impact of a 250 eV primary electron beam was simulated in case of a repeller voltage $U_d = -50V$. | 113 |
| 11.3 | Side view of a result of a SIMION simulation: The impact of a 250 eV primary electron beam was simulated in case of a collector voltage $U_d = +50V$. | 114 |
| 11.4 | Side view of a result of a SIMION simulation: The potential of the external electric field. | 114 |
| 11.5 | Side view of a result of a SIMION simulation: The potential of the external electrical field. | 115 |